

## Effects of observed projections on turbulence statistics in the intracluster medium

1 MARK A. BISHOP<sup>1</sup>

2 <sup>1</sup>*School of Chemical and Physical Sciences*  
3 *Victoria University of Wellington*  
4 *Wellington 6012*  
5 *New Zealand*

### 6 ABSTRACT

7 The total mass of a cluster is one of its most fundamental properties. Measurements  
8 of the galaxy cluster mass often relies upon assuming hydrostatic equilibrium.  
9 However, this is often invalidated as the intracluster medium (ICM) is continuously  
10 disturbed by mergers, feedback processes, and motions of galaxies. These processes  
11 generate gas motions that contribute nonthermal pressure; typically turbulence, that  
12 leads to an underestimation of the mass by as much as 30%. We can measure turbulence  
13 through indirect probes that come in the form of fluctuations in the X-ray  
14 surface brightness and Sunyaev-Zeldovich effect maps. These are projected characteristics,  
15 encoding the 3D structure of the turbulence in the ICM. This project will  
16 be an analysis of the 3D to 2D projections of the intracluster medium and its effect  
17 on the retrieved statistical measures commonly used in turbulence analysis like the  
18 power spectrum by using numerical simulations appropriate to galaxy clusters.

### 19 1. INTRODUCTION

20 As Figure 1 (Courtois et al. 2013) shows, galaxies are not evenly distributed in  
21 space. Gravity pulls galaxies together, resulting in observed regions in the universe  
22 with higher concentrations of galaxies. These regions are the largest stable, gravita-  
23 tionally bound objects and when they contain ma  udes of galaxies on the order  
24 of hundreds to thousands they are called a galaxy cluster. Galaxy clusters are made  
25 out of three main parts: the galaxies and their respective stars, gas and dust account  
26 for approximately 5% of the total mass in a galaxy cluster. About 15% of a galaxy  
27 cluster’s mass is represented as the intracluster medium (ICM); a hot, diffuse, plasma  
28 trapped in the regions between the galaxies. The remainder of the mass present in  
29 the cluster is the dark matter.

30 The ICM continually emits radiation across many wavelengths via various processes.  
31 The X-ray emission is predominantly caused by: free-free (bremsstrahlung) emission  
32 from charged particles, and extended emission from lines like the Fe xxv and He $\alpha$ .

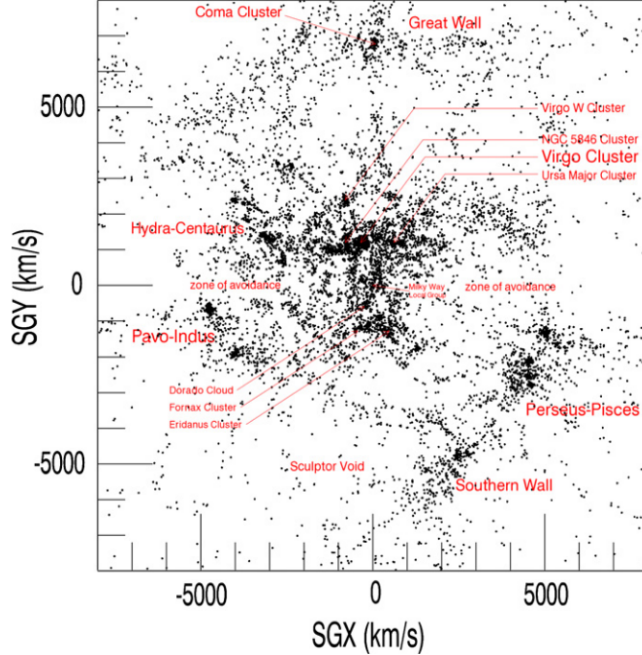


**Figure 1.** Figure from Courtois et al. (2013) showing a projection normal to the supergalactic plane (SG) with SG Z-coordinate between  $-1000 \text{ km s}^{-1}$  to  $1000 \text{ km s}^{-1}$ . Each dot represents a galaxy from the V8k catalog.

33 Emission lines (like H $\alpha$ ) can also be detected in the optical/UV bands for specific  
 34 regions of the ICM (such as the cold gas filaments). The ICM can also be seen by ex-  
 35 amining the changes in the cosmic microwave background (CMB) blackbody radiation  
 36 caused by CMB photon inverse Compton scattering with high energy electrons in the  
 37 ICM; this is called the (thermal) Sunyaev-Zeldovich (SZ) effect. When the photons  
 38 obtain energy from the bulk motion of the ICM, this is called the kinetic SZ (kSZ)  
 39 effect. Lastly, by using multiple frequency radio observations, rotation measures can  
 40 be extracted from regions containing strong synchrotron emission. Examples of some  
 41 of these mentioned ICM observation techniques are shown in Figure 2.

42 It is often assumed that the ICM is in a state of hydrostatic equilibrium, the hot  
 43 ICM plasma is bound to the cluster structure by the strong gravitational well of dark  
 44 matter and held afloat by the internal (predominantly thermal) pressure. However,  
 45 galaxy clusters are typically in a state of dynamical evolution, there are constant  
 46 processes underway such as: mergers between multiple clusters, active galactic nucleus  
 47 (AGN) feedback, cosmic gas accretion, and galaxy dynamics. These processes have  
 48 the effect of injecting energy into the ICM at a large scale, as a result, it is expected  
 49 that the ICM is turbulent, allowing for the transfer of energy from these large scales  
 50 into thermal energy. These perturbations can be observed through the observation  
 51 methods, but there remains many open questions. Figure 3 shows an example of X-  
 52 ray surface-brightness fluctuations of Coma cluster (left) and a line-of-sight velocity  
 53 map of the filamentary structure in the core of the Perseus cluster; these fluctuations  
 54 appear to be turbulent.

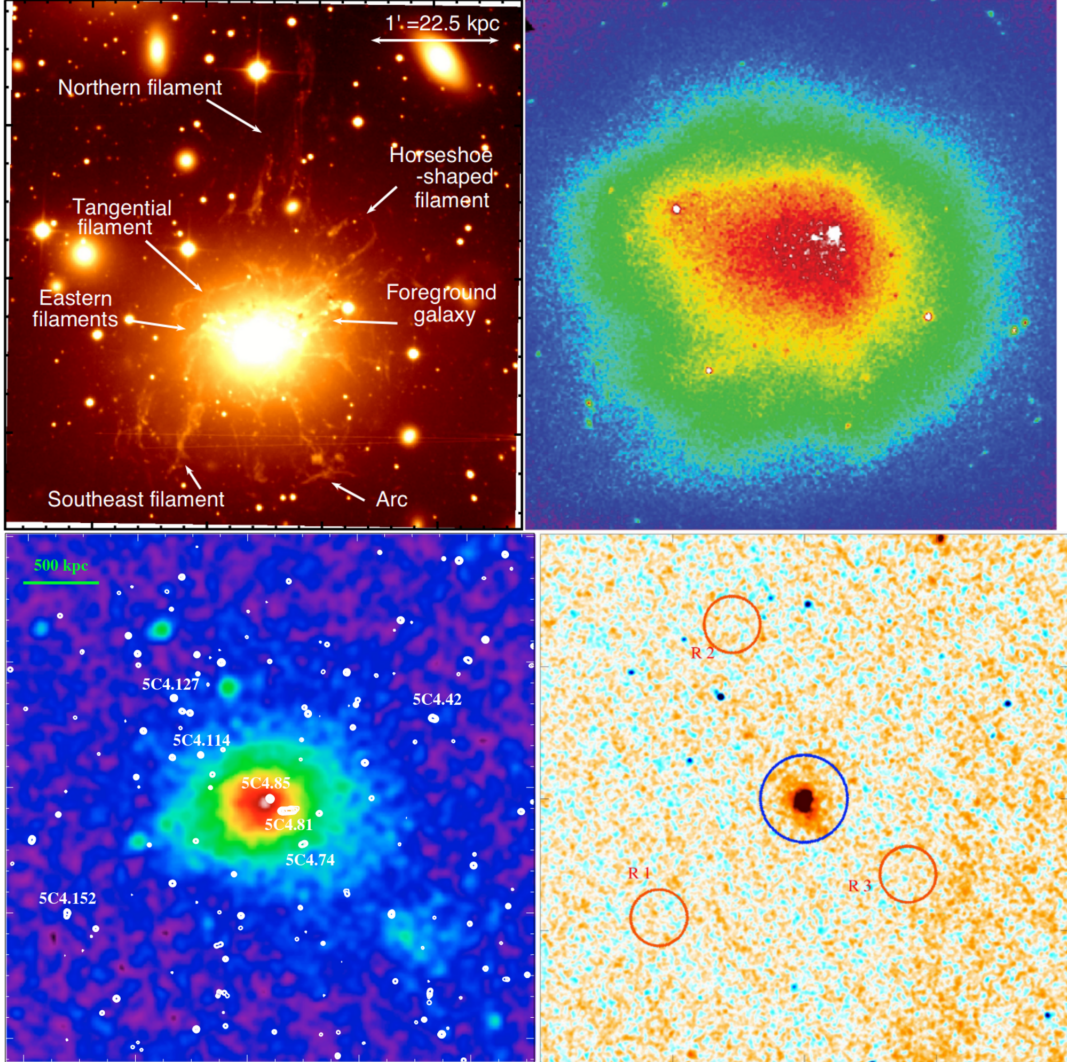


**Figure 2.** Top left, the mean integrated flux from emission line observations centered around NGC1275/Perseus cluster (Gendron-Marsolais et al. 2018). Top right, the X-ray observation from XMM-Newton of the Coma cluster (Churazov et al. 2012). Bottom left, composition of the X-ray image from the ROSAT All Sky Survey (background colors) and with radio emission as the white contours of which, rotation measures can be extracted from the Coma cluster (Bonafede et al. 2010). Bottom right, the SZ effect observation of the Coma cluster (inside the blue circle) (Khatri & Gaspari 2016).

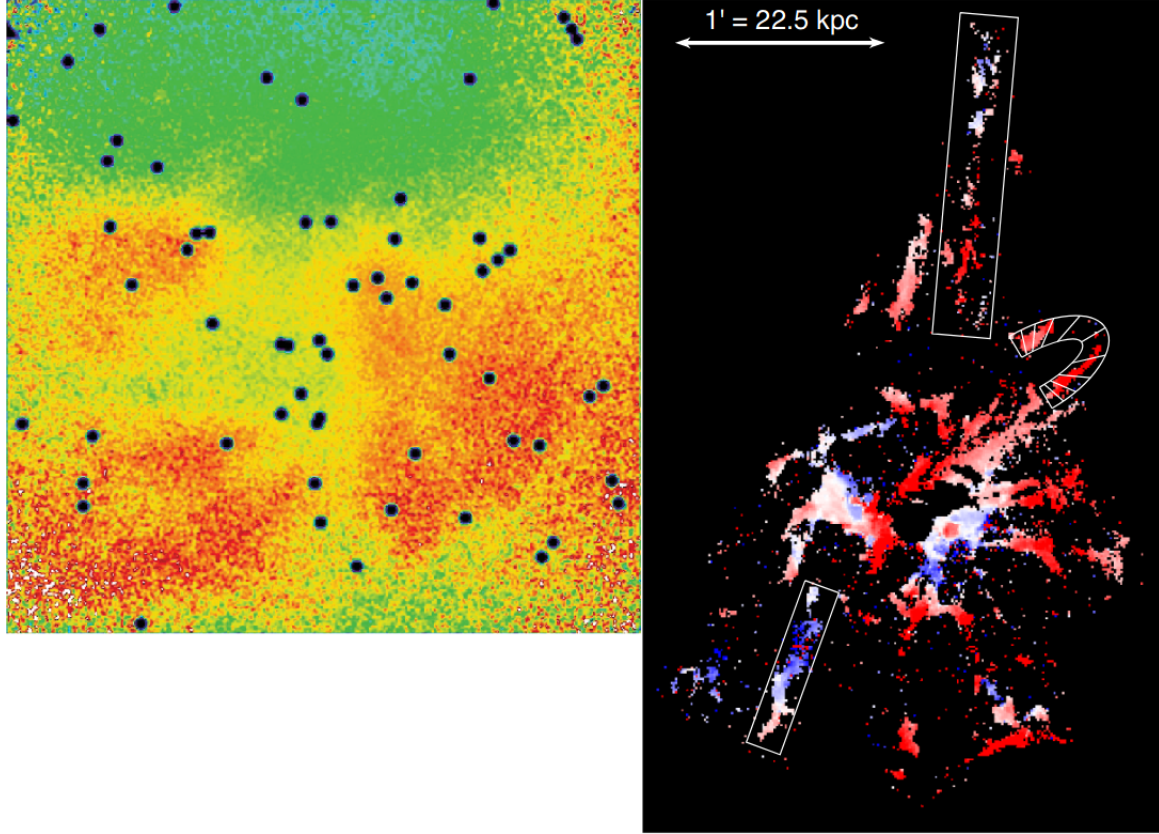


**Figure 3.** Left, X-ray surface brightness fluctuations of the Coma cluster obtained after subtracting a smooth unperturbed model (Churazov et al. 2012). Right, line-of-sight velocity map of NGC1275/Perseus filamentary structure obtained from the emission line Doppler shifts (Gendron-Marsolais et al. 2018).

55                    2. LITERATURE REVIEW

56                    2.1. *Turbulence and scales in the ICM*

57       It is common for astrophysical plasma to be turbulent; from the solar wind, the inter-  
 58       stellar medium, and to scales as large as the intracluster medium (ICM) (Brandenburg  
 59       & Nordlund 2011; Brandenburg & Lazarian 2013). Turbulence is often characterized  
 60       by random/chaotic motions, diffusivity and dissipation. The random motions induced  
 61       by turbulence means it is typical to analyze using statistical methods; Figure 3 shows  
 62       the apparent randomness in ICM observations. Diffusivity acts to mix and transfer  
 63       properties like mass, momentum and energy at enhanced, efficient rates. Turbu-  
 64       lence acts as a mechanism for energy transfer: transferring energy from some large  
 65       (driving) scale down to small scales until dissipation effects become strong, finally  
 66       converting into internal energy. It is common to view this cascade of energy from  
 67       large to small scales as fluctuations of a large size being broken up and diffused into  
 68       smaller fluctuations.

69       The energy in the ICM can come from many sources with varying time, length  
 70       and energy scales. Common forms include: galaxy cluster mergers creating large  
 71       scale sloshing motions in the ICM which induce turbulence on scales of hundreds of  
 72       kiloparsec, and powerful active galactic nuclei (AGN) ejecting matter from the core  
 73       of a galaxy out into the ICM on scales of tens of kiloparsec Simionescu et al. (2019). [\citet{}](#)

74       It is common to analyze the random fluctuations using statistical methods. Using  
 75       power spectral densities (Appendix A, Appendix B), decomposing the variance into  
 76       Fourier space wavenumbers provides the large driving scale, the inertial range, and  
 77       the dissipation scales. Most of the energy in a turbulent flow resides in the large  
 78       scales, which is seen as a peak in the power spectrum. The inertial range is typically  
 79       a power law slope describing the transfer and breakup of energy from the large scale  
 80       to smaller scales. A common power law value is  $\beta_3 = 5/3$  (Appendix A), the Kol-  
 81       mogorov spectrum (Kolmogorov 1941). Analyzing random fluctuations and finding  
 82       the Kolmogorov spectrum is not indicative of a turbulent medium but is a strong  
 83       indicator; it should be noted that turbulence could take any (negative) power law  
 84       value. At the smallest scale, dissipation occurs; transferring the energy from the tur-  
 85       bulent flow, seen as an exponential drop off. This is an idealized picture; the cascade  
 86       of energy can be a broken power law, the rate of energy transfer changing depending  
 87       on the physics at those scales.

88       In the ICM, assuming a driving scale  $L = 100$  kpc, an estimated Spitzer mean free  
 89       path  $\lambda_{\text{mfp}}$  ranging from  $\sim 0.1$  to 10 kpc (Spitzer 1962; Donnert et al. 2018), and  
 90       estimated ion-gyroradius  $\rho_i \sim 1$  npc (Kunz et al. 2022). We have,  $\rho_i \ll \lambda_{\text{mfp}} \ll L$   
 91       which has important physical consequences. The ICM should be collisional (atleast,  
 92       weakly collisional) until the viscous scale determined by  $\lambda_{\text{mfp}}$  which disagrees with  
 93       observations. Similarly, the Spitzer viscosity provides a small Reynolds number; a  
 94       number describing the level of turbulence with higher turbulence providing higher  
 95       Reynolds numbers. To rectify these issues, additional mechanisms have been argued

for allowing collisions to happen at smaller scales at the cost of being out of reach of observations (Donnert et al. 2018). But, there are still many uncertainties in the observations as will be further discussed in this section.

## 2.2. Magnetic fields and rotation measure observations

The frozen-in flux theorem (sometimes called Alfvén’s theorem) states: the magnetic fields are embedded and constrained to move within the plasma. Movement of the plasma results in a movement of the magnetic field and vice versa. Turbulent motions driven within the ICM are therefore expected to produce turbulent motions in the embedded magnetic fields.

Intracluster medium magnetic fields strengths are typically in the ranges of  $\lesssim 10 \mu\text{G}$  (Carilli & Taylor 2002). Such a weak magnetic field would imply a large plasma  $\beta$ : a plasma parameter describing the ratio of thermal to magnetic pressure

$$\beta = \frac{p_{\text{therm}}}{p_{\text{mag}}} = \frac{n k_B T}{B^2 / 2\mu_0} \lesssim 100 \quad (1)$$

where  $T \approx 10^8 \text{ K}$  and  $n \approx 10^{-3} \text{ cm}^{-3}$  (van Weeren et al. 2019). This fact is often made use of in simulations to reduce computational complexity by assuming the allowance of the neglection of magnetic fields. For example, Gaspari & Churazov (2013); Gaspari et al. (2014) (and similarly, Fang et al. (2018)) use FLASH (Fryxell et al. 2000) to simulate the ICM using a 2 fluid (electron-ion) hydrodynamics. The effects of the magnetic field are encapsulated in the thermal conductivity  $\kappa$  (Spitzer 1962)

$$\kappa \simeq 0.76 f n_e k_B \lambda_{e,mfp} v_{e,th} \quad (2)$$

where  $v_{e,th} = \sqrt{3k_B T_e / m_e}$  is the electron thermal speeds and  $\lambda_{e,mfp} \approx 10^4 T_e^2 / n_e$  is the electron mean free path which form the characteristic length scale and speed of conduction. The  $f$  parameter determines the magnetic suppression factor, using the argument of the dynamically unimportant magnetic field compared to thermal pressure (due to the large plasma  $\beta$  and small coherence lengths). Gaspari & Churazov (2013) compare their simulations to observations (Churazov et al. 2012) and find they are consistent with a highly suppressed conduction  $f \approx 10^{-3}$ .

However, Mohapatra et al. (2022a,b) finds in multiphase idealized MHD simulation runs, the magnetic field couples the hot and cold phases at the large scales. The magnetic field becomes dominant in the cold-phase at small scales due to the frozen-in flux theorem; the cold-phase condensates out of the hot phase leading to an increase in the plasma pressure. From multiphase simulations with self-regulated AGN feedback, Wang et al. (2021) also finds the magnetic field is dynamically important in the structure the cold-phase filaments and hints at potential effects on the hot-phase but cannot conclude anything due to limitations in the simulation resolution.

The rotation measure is the measure of the change in direction of polarization of an electromagnetic wave due to Faraday’s effect: the proportional rotation of polarized

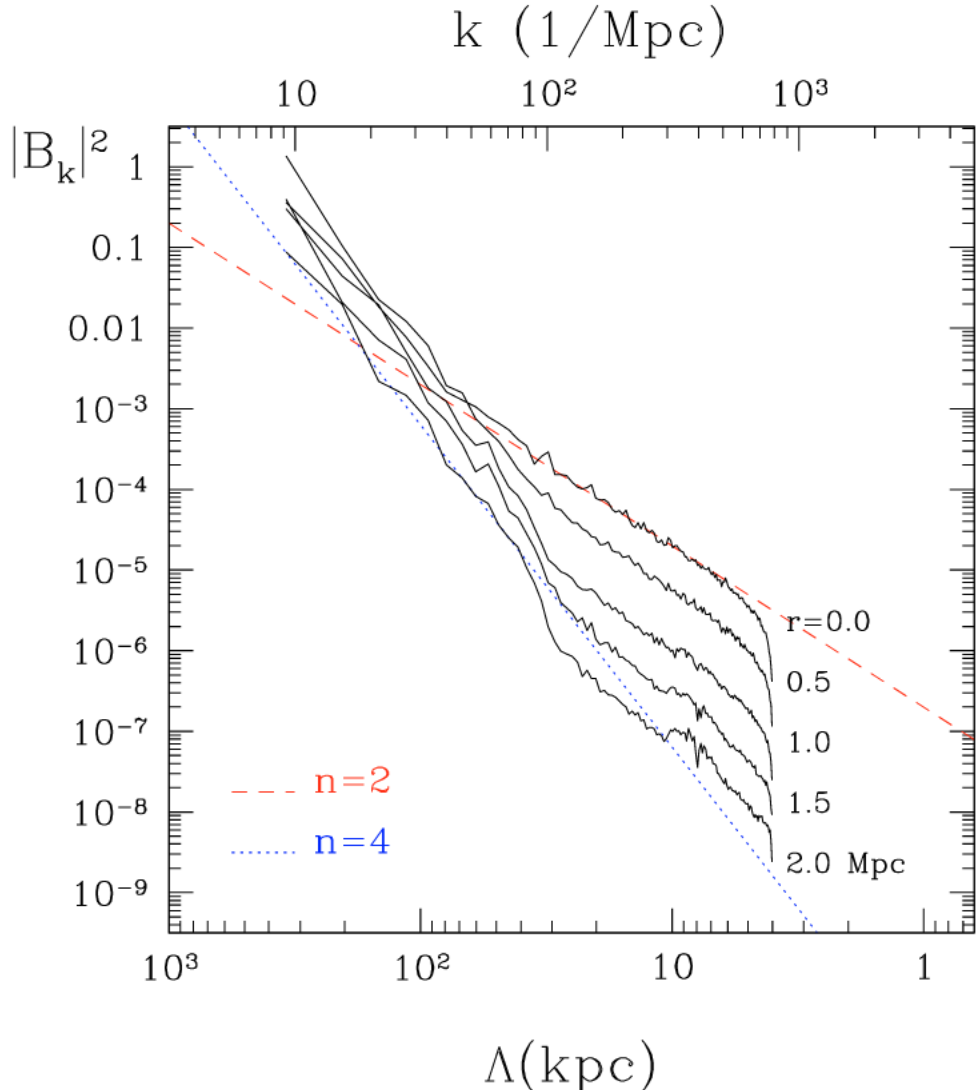


**Figure 4.** Figure showing the magnetic field power spectra as a function of distance from the cluster center (Govoni et al. 2006, Fig. 13). Black lines show the modal spectrum power law slopes with adjacent text indicating distance from the cluster centre with power law slope lines of  $\alpha_3 = 2$  (dashed red) and  $\alpha_3 = 4$  (dotted blue). The magnetic field power spectrum clearly has a break scale, changing from  $\alpha_3 \approx 4$  at large scales to  $\alpha_3 \approx 2$  at small scales. This break scale increases with increasing distance from the cluster center.

light to the projection of the magnetic field along the light propagation direction. In the ICM, the polarized light required for the rotation measure is generated from synchrotron emission of relativistic particles from cosmic radio sources like astrophysical jets, see Carilli & Taylor (2002) for a relevant review. From radio observations spanning different wavelengths, rotation measures can be derived in regions where polarized light from a background synchrotron emitting source passes through the magnetic field of the ICM Vogt & Enßlin (2003, 2005); Brentjens & de Bruyn (2005); Govoni et al. (2006); Guidetti et al. (2008); Vacca et al. (2010); Bonafede et al. (2010); Vacca et al. (2012) estimate the magnetic field power spectrum in galaxy clusters de-

rived from the rotation measure observations. Guidetti et al. (2008); Bonafede et al. (2010); Vacca et al. (2010) find modal spectrum power law slopes consistent with Kolmogorov  $\alpha_3 \approx 11/3$ , whereas Vacca et al. (2012) finds  $\alpha_3 = 2.8 \pm 1.3$  and Murgia et al. (2004) finds  $\alpha_3 \approx 2$ . Govoni et al. (2006); Laing et al. (2008) find broken power law spectra with steep and Kolmogorov slopes at the large scales, and shallow slopes at the small scales. Figure 4 shows the broken magnetic power spectrum for different radial distances from the core of the cluster (Govoni et al. 2006). For all radial distances, there is a broken magnetic power law spectrum with the large scale  $\alpha_3 \approx 4$  slope, transitioning to a  $\alpha \approx 2$  power law at small scales with the break location increasing with increasing radial distance from the core. Go [redacted] et al. (2006); Laing et al. (2008) state the magnetic field could be dominated by small scale structures in the cluster core, and large scale structures at the outskirts, giving rise to their observations. Figure 4 could be explained via a faster decay of turbulence in the central region, and slower decay in the outskirts due to the stratification effects. In the more stratified central regions of the ICM, the energy gets converted to potential energy faster, resulting in a larger turbulence amplitude. This is corroborated by the kinetic energy measurements in cosmological and idealized HD simulations Shi et al. (2018); Shi & Zhang (2019). The broken power law may also be consistent with the picture of small scale dynamo in the ICM Schekochihin & Cowley (2006); Rincon (2019); the mechanism for increasing the strength of the magnetic field from a small, origin magnetic field Garaldi et al. (2021). Lastly, Domínguez-Fernández et al. (2019) finds from cosmological simulations, the dynamical state of the magnetic field is not universal and can be significantly affected by a complex sequence of amplification events previously occurred during the lifetime of the cluster. Therefore, the wide range of power laws obtained from the rotation measure observations could be due to different physics occurring at the scales and locations probed by the separate rotation measure maps, simplifications in modelling or differences in the galaxy clusters themselves (see also, Donnert et al. 2018).

### 2.3. Density fields and X-ray observations

The ICM is compressible, which can be inferred via the existence of sound waves (Zhuravleva et al. 2014a) and shocks. The density in *compressible* turbulence exhibits fluctuations that can trace the velocity fluctuations (Sreenivasan 1995). The ICM is also stratified; the density is large in the core and decreases (exponentially) with increasing radial distance from the core. The compressibility and stratification of the ICM leads to significant changes in the turbulence behaviour: creating anisotropy. Buoyancy forces can cause gas to rise or sink on its density which can contribute to the generation of turbulence. Inversely, the stratification can restrict the mixing of gases of different densities. The existence of density perturbations (suggested to be dominated by turbulence), can affect the mass estimates of the ICM with bias in the range of 10 – 30% (Mroczkowski et al. 2019; Pratt et al. 2019).

X-ray observations trace the emission weighted line-of-sight integral of the electron density squared (primarily through free-free emission)

$$I_X(\boldsymbol{\theta}) \propto \int \rho_e(\boldsymbol{\theta}, \ell)^2 \epsilon_X(\boldsymbol{\theta}, \ell) d\ell \quad (3)$$

The X-ray image obtained from telescopes like Chandra and XMM-Newton return the above equation; to obtain the fluctuations, typically a model is assumed (such as the beta model, Arnaud 2009) giving the function  $\bar{I}_{X,0}(\boldsymbol{\theta})$  describing the mean distribution. The total image is then described similar to a Reynolds decomposition

$$I_X(\boldsymbol{\theta}) = \bar{I}_{X,0}(\boldsymbol{\theta}) + \delta I_X(\boldsymbol{\theta}) \quad (4)$$

where  $I_X(\boldsymbol{\theta})$  is the plane-of-sky observed surface brightness image,  $\bar{I}_{X,0}(\boldsymbol{\theta}) = \langle I_X(\boldsymbol{\theta}) \rangle$  is the assumed average/large scale model, and  $\delta I_X(\boldsymbol{\theta})$  is the surface brightness fluctuations (where  $\langle \delta I_X(\boldsymbol{\theta}) \rangle = 0$ ).

Churazov et al. (2012) have extracted X-ray surface brightness fluctuations in the core region of the Coma cluster with XMM-Newton and Chandra space telescopes. These observations include exposure factors, bright sources, noise, and point spread function factors. [ ] exposure factors arise due to observation limits of the telescope design and/or observing time/locations. So there are regions in the retrieved images that have not been sampled as much as others. The raw observed images need to be corrected for via the known exposure map. The noise in the image can be described as Poisson noise which acts as a constant across all wavenumbers. Retrieved power spectra will converge to the noise floor. Churazov et al. (2012) discuss a method for subtracting resampled noise to obtain a noise subtracted spectrum. The contaminating sources (like foreground and background bright compact sources) need to be removed via simple masking due to their impacts on power spectrum at small scales (large wavenumbers). Telescope observations obtain the true image (with the noise and exposure etc) convolved with a point spread function (PSF). In Fourier space, the PSF convolution becomes multiplication. Therefore, a simply way to correct for the PSF is to divide the energy spectrum by the energy spectrum of the PSF correction. Churazov et al. (2012) use the Arévalo et al. (2012) method (Appendix A) for estimating the power spectrum of the X-ray surface brightness fluctuations during each stage of the removal and correction of the previously discussed noise, point sources, and PSF factors. Finally, converting the image into the fluctuations using a modelled beta distribution, 2D power spectra are obtained via the Arévalo et al. (2012) method (Appendix A) and then converted to 3D spectra using the projection-slice theorem relation (again, Appendix A)

$$E_{\rho,2D}^{\text{modal}}(|\mathbf{k}_\theta|) = E_\rho^{\text{modal}}(|\mathbf{k}_\theta|) \int E_{EM}^{\text{modal}}(k_\ell) dk_\ell \quad (5)$$

where  $k_\theta = |\mathbf{k}_\theta|$  is the magnitude of the 2D plane-of-sky wavenumber vector,  $k_\ell$  is the line-of-sight wavenumber, and  $E_{EM}^{\text{modal}}(k_\ell)$  is the modal spectrum of the projection emissivity factor  $\epsilon_X$ .

10

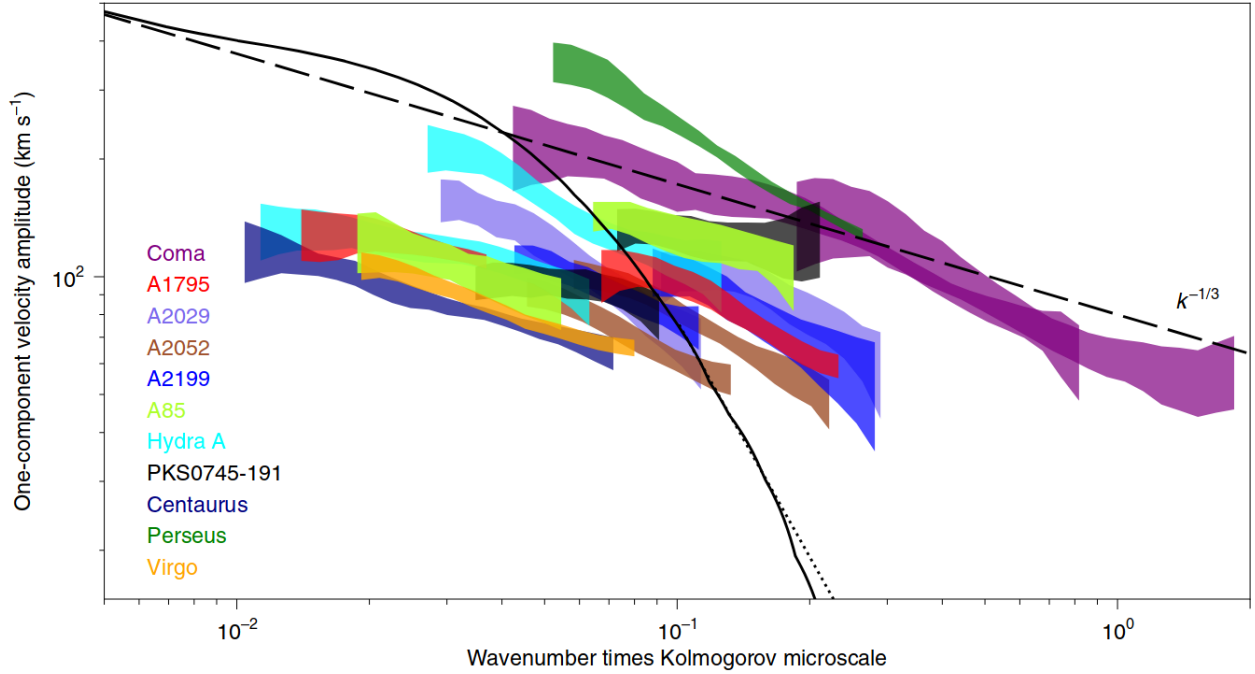


**Figure 5.** Figure from Zhuravleva et al. (2019), showing the one-component velocity amplitude spectrum of a sample of galaxy clusters with the width showing the  $1\sigma$  uncertainty. Additionally, the Kolmogorov  $k^{-1/3}, \delta_3 = 1/3$  is added in dashed black. The solid black line shows the one-component velocity amplitude of a direct numerical simulation (DNS)

Zhuravleva et al. (2014b) argues for the possibility of using the density power spectrum as a proxy for the velocity power spectrum via the relation

$$E_{\rho}^{\text{modal}}(|\mathbf{k}|) \approx \left(\frac{\eta}{c_s}\right)^2 E_V^{\text{modal}}(|\mathbf{k}|) \quad (6)$$

where  $c_s$  is the speed of sound,  $E_{\rho}^{\text{modal}}(|\mathbf{k}|)$  is the modal spectrum of the density fluctuation amplitudes  $\rho_{\delta}/\rho$  given via,

$$E_{\rho}^{\text{modal}}(|\mathbf{k}|) = \left| \frac{\hat{\rho}_{\delta}}{\hat{\rho}} \right|^2 \quad (7)$$

and  $E_V^{\text{modal}}(|\mathbf{k}|)$  is the modal spectrum of the velocity fluctuations

$$E_V^{\text{modal}}(|\mathbf{k}|) = |\hat{u}_x|^2 + |\hat{u}_y|^2 + |\hat{u}_z|^2 \quad (8)$$

where the hat ( $\hat{\cdot}$ ) denotes the Fourier transform (Appendix A). This relation is derived for relaxed clusters dominated by buoyancy physics at large scales; at small scales, the density is a passive scalar advected by the velocity field. Another key assumption made, is the turbulence is *isotropic* at these small scales.

The simulations by Gaspari & Churazov (2013); Gaspari et al. (2014); Fang et al. (2018) use simulations to constrain the slope of the density fluctuations in a non-conductive medium, varying the magnetic suppression factor  $f$ , and Mach number  $\mathcal{M}$ .

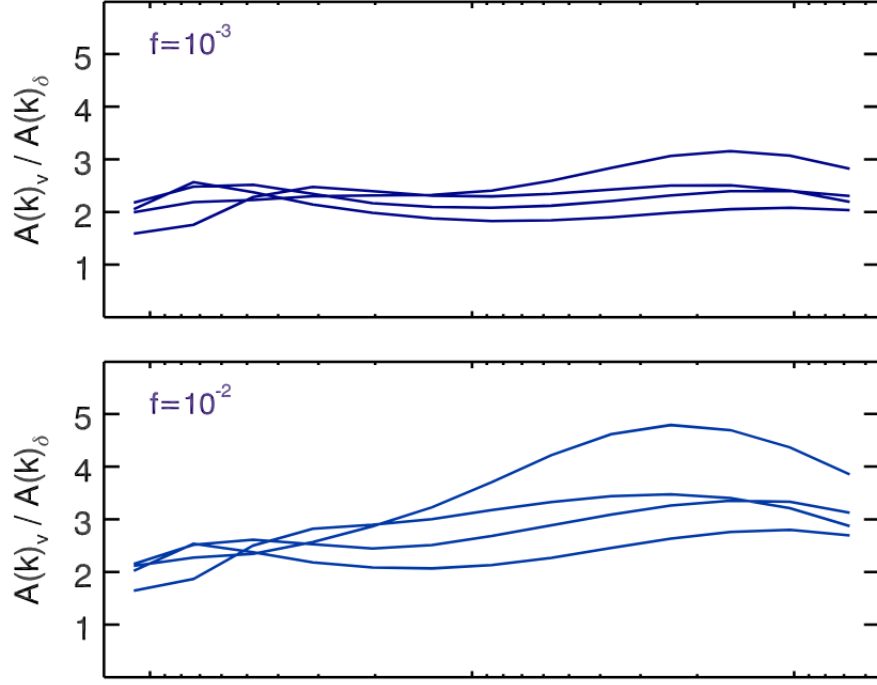


**Figure 6.** Figure from Gaspari et al. (2014), showing the ratio between the velocity amplitude spectrum to the density amplitude as a function of wavenumber  $k$  for different Mach numbers (shown as the same lines on the same plot) and thermal conduction parameters  $f = 10^{-3}$  (top) and  $f = 10^{-2}$  (bottom).

Figure 6 shows the ratio of the velocity amplitude spectrum to the density amplitude spectrum as a function of wavenumber  $k$ , with Mach numbers of  $\mathcal{M} = 0, 0.25, 0.5, 0.75$  plotted on the same plots, and thermal conduction values of  $f = 10^{-3}, 10^{-2}$  (top and bottom respectively). With thermal conduction values less than  $f = 10^{-3}$ , the ratio of velocity to density amplitude spectra does not change significantly, the velocity spectrum staying approximately 2-3 times greater than the density spectrum. With increasing thermal conductivity,  $f = 10^{-2}$  (and Mach numbers), the velocity spectrum is roughly 2 times greater than at low wavenumbers and 3 times greater at high wavenumbers, and almost 5 times greater at high Mach number. The simulations by Gaspari & Churazov (2013); Gaspari et al. (2014); Fang et al. (2018) find that the slope of the density fluctuations in a non-conductive medium is approximately Kolmogorov despite the stratification (also seen in, Vazza et al. 2011; Valdarnini 2019), with the power law steepening with increasing conductivity towards a Burgers power law ( $\beta_3 = 2$ ). It was also found that this relationship only weakly depends on the Mach number.

Zhuravleva et al. (2014a); Walker et al. (2015); Zhuravleva et al. (2018, 2019); de Vries et al. (2023) use the density to velocity relation from Zhuravleva et al. (2014b) to obtain the spectrum of the velocity fields from X-ray surface brightness fluctuations. Reproduced from Zhuravleva et al. (2019), Figure 5 shows the one-component velocity amplitude spectra of a sample of galaxy clusters at  $1\sigma$  statistical

uncertainty. Superimposed on this image is the Kolmogorov power law ( $\delta_3 = 1/3$ ) in dashed black and solid black shows scaled spectra results from a HD direct numerical simulation (DNS). The DNS spectra shows the scales dissipation occurs at, associated with the Spitzer viscosity/resistivity based upon electron-ion collisions (Spitzer 1962). If the velocity field were subject to this Spitzer viscosity level, one would expect to observe an exponential drop off in velocity (as indicated by the black line). The observations appear to pass the traditional Spitzer viscosity without exponentially decaying, suggesting the true, effective viscosity in the ICM is not the Spitzer value.

Zhuravleva et al. (2022) examines the  $E_\rho^{\text{modal}} \rightarrow E_V^{\text{modal}}$  relation in more detail using the Omega500 non-radiative HD cosmological simulations (Nagai et al. 2007; Nelson et al. 2014). They find the relation has the lowest scatter for 3D density amplitude to velocity spectrum conversion, but the projected density squared (the X-ray surface brightness) has the largest scatter. They show there is a strong linear relation between the velocity spectrum and the 3D density amplitudes, giving merit to their previously stated relation. This relation gets weaker for perturbed clusters and is significantly weaker for the projected amplitudes.

Mohapatra & Sharma (2019); Mohapatra et al. (2020, 2021, 2022a) use FLASH (Fryxell et al. 2000) to simulate idealized stratified HD turbulence where initial density and pressure slopes are given as an initial exponential function in the form

$$P(t=0) = P_0 e^{-z/H_P} \quad (9)$$

$$\rho(t=0) = \rho_0 e^{-z/H_\rho} \quad (10)$$

where  $H_P, H_\rho$  are the pressure and density scale heights respectively. Figure 7 shows a couple figures of the stratified turbulence from Mohapatra et al. (2020). Where the Ri (Richardson) number (at a scale  $\ell$ )

$$Ri_\ell = \frac{N^2}{v_\ell^2/\ell^2} \quad (11)$$

is the ratio of stratification buoyancy ( $N$ , the Brunt-Vaisala frequency) to turbulent shearing forces ( $v_\ell^2/\ell^2$ ,  $v_\ell$  is the velocity at length scale  $\ell$ ). For moderate Richardson number  $Ri = 1$  (top row), the projected density (left), projected density fluctuations (middle) and slice of density fluctuations (right) are shown with the black arrows representing the projected velocity field (right and middle) and slice of the velocity field (right). The bottom row shows projected density (left), projected density fluctuations (middle) and slice of the density fluctuations (right) for strong stratification  $Ri = 13$  along with the projected (left and middle) and slice (right) velocity field as black arrows. The key takeaway is: for low to moderate stratification, the turbulence is able to form circular eddies (seen as the circular patterns in the velocity fields). For strong stratification, the buoyancy forces dominate, restricting the turbulence in the direction of stratification. This shown in the velocity fields, they are elongated perpendicular to the direction of stratification (z-direction), sometimes referred to *slab* or *pancake* turbulence.

The level of stratification can be better described by the perpendicular/transverse (to the direction of gravity) Froude number  $Fr_{\perp}$  where  $Fr_{\perp} \ll 1$  is strong stratification and  $Fr_{\perp} \gg 1$  is weakly stratified. The perpendicular Froude number is the ratio of the buoyancy timescale to turbulent timescale

$$Fr_{\perp} = \frac{v_{\perp}}{N\ell_{\perp}} \approx \frac{1}{\sqrt{Ri_L}} \quad (12)$$

This works better as at parameterizing the stratification over the Richardson number at the driving scale  $L$  because, the eddies are anisotropic in strong turbulence, becoming larger perpendicular to the direction of stratification, and smaller parallel parallel to stratification.

[Mohapatra et al. \(2020, 2021\)](#) iterates over different levels of stratification to derive a new relation for the variance of the logarithmic density fluctuations  $\sigma_s^2$  based on  $Fr_{\perp}$ , turbulence driving parameter  $b$ , pressure and entropy scale heights  $R_{PS} = H_P/H_S$ , and Mach number  $\mathcal{M}$

$$\sigma_s^2 = \ln \left( 1 + b^2 \mathcal{M}^4 + \frac{0.10}{(Fr_{\perp} + 0.25/\sqrt{Fr_{\perp}})^2} \mathcal{M}^2 R_{PS} \right) \quad (13)$$

This definition arises from the net density perturbations in stratified turbulence consisting of the buoyancy and turbulent fluctuations

$$\delta\rho^2 = \delta\rho_{turb}^2 + \delta\rho_{buoyancy}^2 \quad (14)$$

A related works by [Molina et al. \(2012\)](#) found the relation,

$$\sigma_s^2 = \ln \left( 1 + b^2 \mathcal{M}^2 \frac{\beta}{\beta + 1} \right) \quad (15)$$

where  $\beta$  is the ratio of thermal to magnetic pressure (the plasma beta parameter). The formula  $\sigma_s^2 = \ln(1 + b^2 \mathcal{M}^4)$  is consistent for no stratification (essentially,  $Ri \rightarrow 0$  meaning no buoyancy fluctuations), this is the form essentially assumed in the earlier expression

$$E_{\rho}^{\text{modal}}(|\mathbf{k}|) \approx \left( \frac{\eta}{c_s} \right)^2 E_V^{\text{modal}}(|\mathbf{k}|) \quad (16)$$

by [Zhuravleva et al. \(2014b\)](#).

[Simone et al. \(2022\)](#) used the *Itasca* cluster sample which is a set of galaxy clusters simulated using the cosmological *ENZO* code and neglected the magnetic fields. They examine the density to velocity relation and note it is consistently smaller (but still linear) with large scatter than previous literature suggests ([Gaspari et al. 2014; Zhuravleva et al. 2014b](#)) and could not detect a relation between the Richardson number and the logarithmic density fluctuations reported in [Mohapatra et al. \(2020\)](#). Separating the cluster samples to relaxed and unrelaxed. Relaxed clusters appear to agree

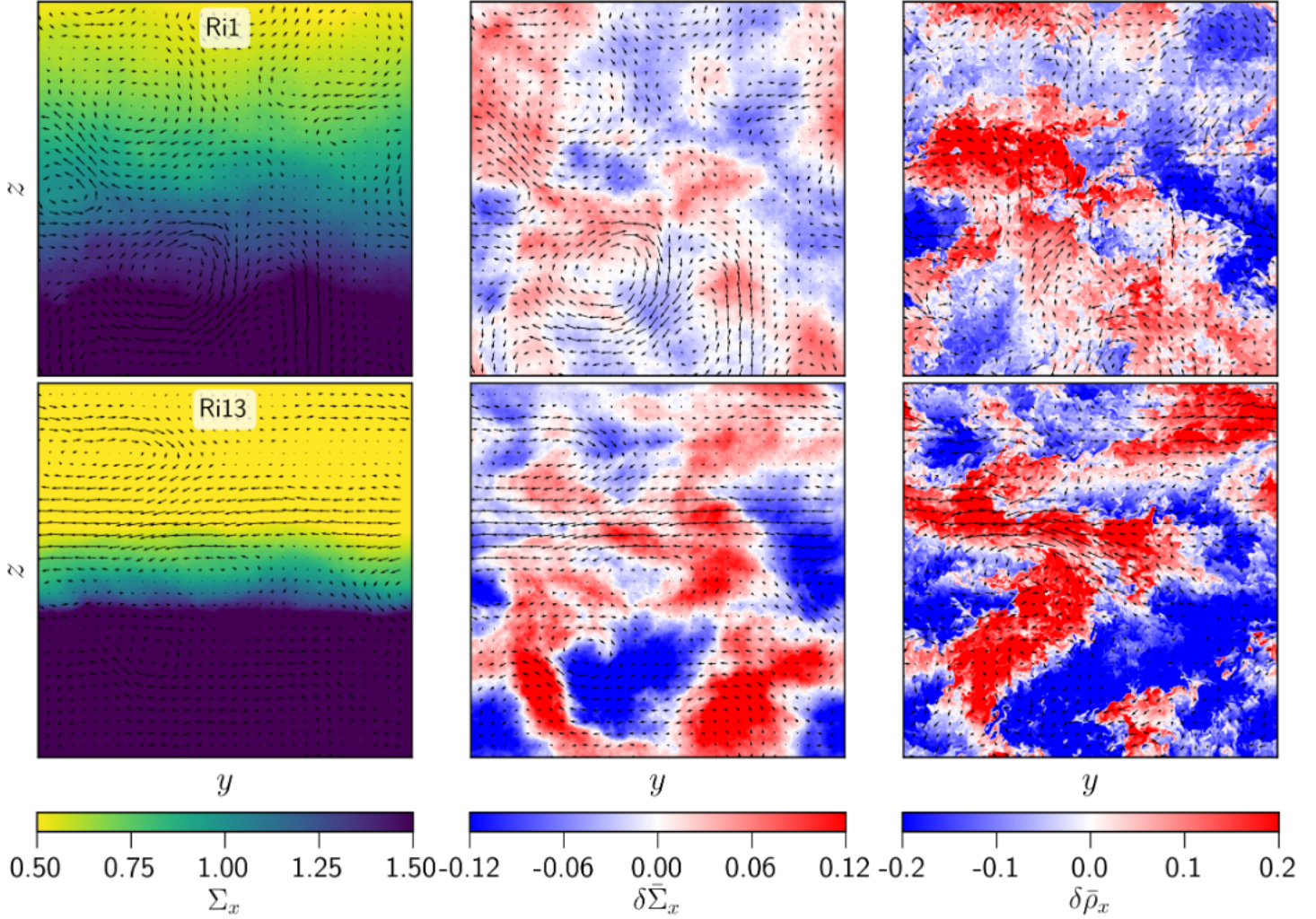


**Figure 7.** Figure from Mohapatra et al. (2020) showing: the projected density along the  $x$ -direction  $\Sigma_x$ , the corresponding (projected) density fluctuations  $\delta\bar{\sigma}_x$ , and the normalized density perturbation slices  $\delta\bar{\rho}_x$  taken in the  $x = 0$  plane; for moderate and strong stratification strengths, characterized by the Richardson numbers  $Ri = 1, 13$  respectively. The black superimposed arrows indicate the projected velocity field in the 2D plane for the projected density and projected density fluctuations, and the slice at  $x = 0$  velocity field for the density slice image.

with the unity relation ( $\eta \approx 1$ ) whereas unrelaxed clusters have a weaker relation. They investigate the clumps (which may or may not be physical, Angelinelli et al. 2021; Zhuravleva et al. 2022) and find they strongly influence the density-velocity relation.

In summary, ... (try to wrap up this section with a brief statement about what we can learn from X-ray surface brightness fluctuations and what the remaining issues/uncertainties are)

The Sunyaev-Zeldovich (SZ) effect is the inverse Compton scattering of cosmic microwave background (CMB) radiation with the hot electrons in the ICM. This effect produces a change in the expected black-body spectrum of the CMB and hence it can be used to examine the ICM of a galaxy cluster (Mroczkowski et al. 2019). The observation is described by the emissivity weighted line-of-sight integral of the electron

352 pressure

353

$$Y_{SZ}(\boldsymbol{\theta}) \propto \int P_e(\boldsymbol{\theta}, \ell) \epsilon_{SZ}(\boldsymbol{\theta}, \ell) d\ell \quad (17)$$

354

355 and is a similar method to the X-ray images except we get the electron pressure  
 356 instead of the electron density squared. Really, this is called the thermal SZ effect;  
 357 there is a second order effect where the photons obtain energy based on the bulk  
 358 motion of the ICM called the kinetic SZ effect. Fluctuations in the SZ effect surface  
 359 brightness image trace the projected pressure fluctuations in the ICM. The  $Y_{SZ}$  surface  
 360 brightness fluctuations  $\delta Y_{SZ}$  can be found via Reynolds decomposition, much like the  
 361 X-ray surface brightness fluctuations

362

$$Y_{SZ}(\boldsymbol{\theta}) = \bar{Y}_{SZ,0}(\boldsymbol{\theta}) + \delta Y_{SZ}(\boldsymbol{\theta}) \quad (18)$$

363

364 where the large-scale model  $\bar{Y}_{SZ,0}(\boldsymbol{\theta})$  is typically modelled using a beta distribution  
 365 (Arnaud 2009). **Beta model is not really typical but not really important here**

366 Khatri & Gaspari (2016) use CMB observations from the *Planck* satellite to obtain  
 367 2D SZ effect maps of the Coma cluster. Fluctuations in the SZ effect trace the  
 368 pressure turbulence as the SZ effect is proportional to the line-of-sight integral of the  
 369 electron pressure. The fluctuations are then used to obtain a 2D pressure power spec-  
 370 trum via the flat-sky, spherical harmonics approximation (Appendix A). Then, they  
 371 deproject the 2D SZ perturbations into 3D pressure fluctuations using the projection  
 372 slice theorem (Peacock 1999; Churazov et al. 2012; Zhuravleva et al. 2012, and also  
 373 Appendix A). Figure 8 is a figure obtained from Khatri & Gaspari (2016), showing  
 374 the combination of their pressure amplitude spectrum of the Coma cluster and the  
 375 X-ray Chandra density amplitude spectrum results from Churazov et al. (2012); Gas-  
 376 parsi & Churazov (2013). There is clearly a disconnect between the SZ effect data  
 377 (blue, dark red, yellow, black, green and red markers with error bars) probing the  
 378 large scales of the cluster and the Chandra X-ray data (purple markers with error  
 379 bars). There is an extrapolated band (cyan) attempting to exhibit the inertial range  
 380 with a power law of  $k^{-1/3}$  (Kolmogorov) and connect the two datasets.

381 Using the same arguments as Zhuravleva et al. (2014b), the pressure can also be  
 382 a passive scalar. Zhuravleva et al. (2022) examines the relation of pressure to ve-  
 383 locity spectra ( $E_P^{\text{modal}} = \frac{\eta_P^2}{c_s^2} E_V^{\text{modal}}$ ). Similar to their density results, they find the  
 384 3D pressure amplitudes can be suitable proxies for the velocity with  $\eta_P \approx 1$  for re-  
 385 laxled and unrelaxed clusters. Correlations between the 2D projected pressure (SZ  
 386 effect) and velocity are much weaker but performs better than the projected density  
 387 (X-ray). Similarly, in stratified turbulence, the logarithmic pressure fluctuations to  
 388 Mach number relation is found by Mohapatra & Sharma (2019); Mohapatra et al.  
 389 (2020) to take the form:

390

$$\sigma_{\ln(P)}^2 = \ln(1 + b^2 \gamma^2 \mathcal{M}^4) \quad (19)$$

391

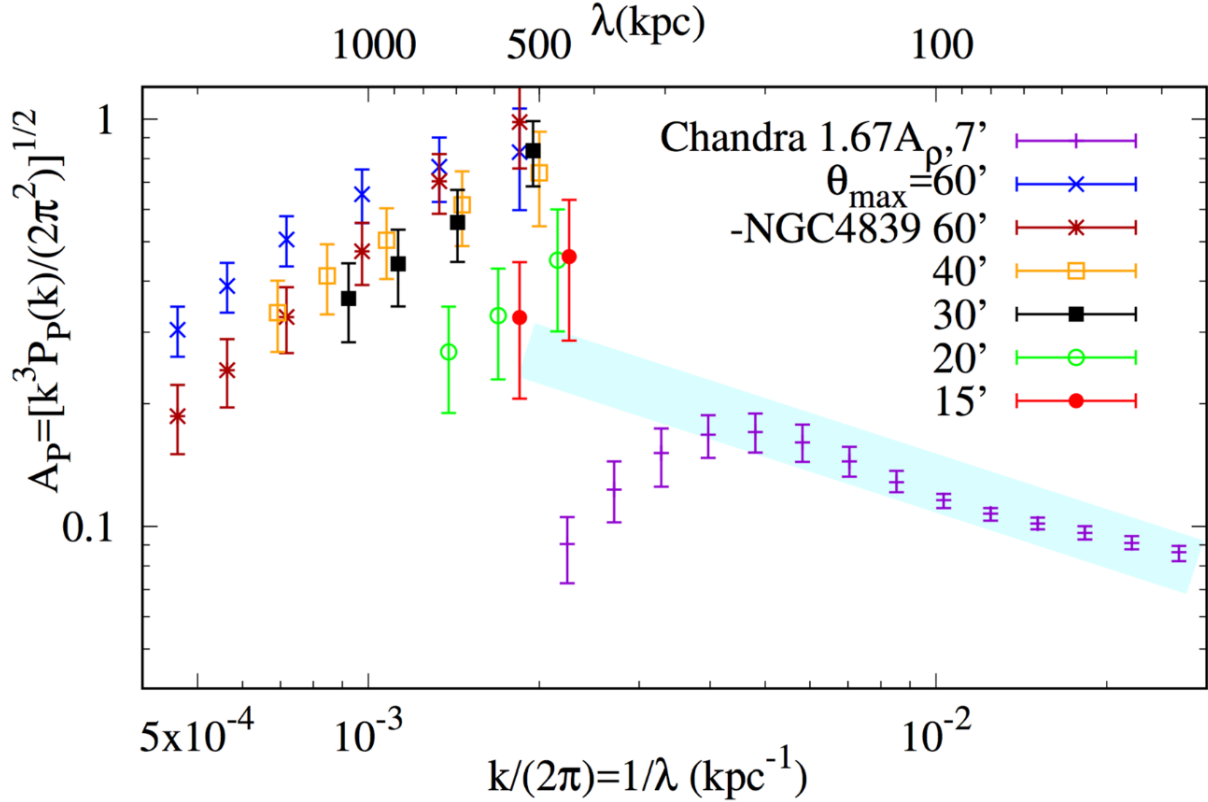


**Figure 8.** Figure from Khatri & Gaspari (2016), combining their own *pressure* amplitude spectrum of the Coma cluster from the SZ effect (blue, dark red, yellow, black, green, red) with the *density* amplitude spectrum from Gaspari & Churazov (2013) also of the Coma cluster but in X-ray from Chandra (purple). The cyan band attempts to connect the two datasets with a Kolmogorov, inertial range, power law band  $k^{-1/3}$ .

for turbulence driving parameter  $b$  and adiabatic index  $\gamma$ . This relation is simpler (*i.e.* doesn't contain the stratification dependence) than the density one ~~(*i.e.* corresponding density relationship)~~ as the buoyant density fluctuations are *isobaric*. This shows the power spectrum of the pressure fluctuations should only depend on the Mach number (and driving parameter and adiabatic index). This indicates the tSZ effect (projected pressure) is the better estimation method for the turbulent velocity (also, Mohapatra et al. 2022c).

Again, brief summary here. Maybe something about how despite this promise, SZ has so far not been studied much because of instrumental limitations

### 398 2.5. Velocity and emission line observations

Using spectroscopic telescopes, emission line spectra can be observed. These spectral lines will come with large Doppler shifts due to the expansion of the universe (and other systematics). The Doppler shifting can be translated to a velocity for each emission line. Hence, these spectroscopic telescopes observe a 3D datacube, a position position and velocity (PPV) (Lazarian & Pogosyan 2000, 2004) with the positions indicating the sky-plane and velocity distribution measurements along the line of sight. Typically, the emission lines are described by a  $\text{sinc}(x) = \sin(x)/x$  function convolved with a Gaussian. By naively taking the peak of the emission line,

407 sometimes called a velocity line centroid we obtain the following:

$$408 \quad 409 \quad \mathcal{V}_{LC}(\boldsymbol{\theta}) \propto \int u_\ell(\boldsymbol{\theta}, \ell) \epsilon_{LC}(\boldsymbol{\theta}, \ell) d\ell \quad (20)$$

410 projected what?

411 an emission weighted projected of the line-of-sight component of the velocity. Otherwise,  
412 the width of the Gaussian can be used.

413 In the centers of some cool-core clusters, filamentary structures can be seen in  
414 H $\alpha$  (an electron orbital transition of Hydrogen from  $n = 3$  to  $n = 2$ ); this is a cold-  
415 phase of the ICM, tracing the recombination of atomic Hydrogen from recently ionized  
416 hydrogen. Because of these energetics, the H $\alpha$  Emission is expected to trace the energy  
417 from the supermassive black hole feedback (see, Zhang et al. 2018, 2022; Mohapatra  
418 et al. 2023, for cold-phase development and blackhole feedback mechanisms). These  
419 filament structures can be observed through spectroscopy, meaning Doppler shift  
420 measurements can be obtained for each pixel in an image, and therefore line-of-sight  
421 velocities (Gendron-Marsolais et al. 2018).

422 The same applies to X-ray spectrometry. The Hitomi telescope (also known as  
423 Astro-H) (Hitomi Collaboration et al. 2016, 2018), was an X-ray telescope with a  
424 spectrometer built to detect bulk and turbulent motions of the intracluster medium by  
425 measuring Doppler shifts and broadening of emission lines (such as Fe xxv and He $\alpha$ )  
426 that unfortunately met a hasty end. Obtaining a single, partial science observation  
427 of the Perseus cluster (Figure 11), Figure 11 shows the observation from Hitomi of  
428 part of the Perseus cluster. The line-of-sight bulk motion on the left, and the line-of-  
429 sight velocity dispersion (broadening) on the right. Previous telescopes like Suzaku  
430 and XMM-Newton were able to perform spectroscopic measurements of the ICM but  
431 had too large errors to be able to make any conclusion remarks other than broad  
432 constraints (Gatuzz et al. 2023).

433 Hitomi Collaboration et al. (2018) finds: the large-scale bulk velocity gradient with  
434 an amplitude of 100km s $^{-1}$  which is consistent with sloshing induced motions. The  
435 lack of evidence for a non-Gaussian distribution implies that the observed velocity  
436 dispersion is dominated by small-scale motions, and a driving scale of turbulence as  
437 mostly smaller than 100kpc. Hitomi's successor, XRISM (XRISM Science Team 2020)  
438 is expected to launch this year intending to recover information that was expected  
439 from Hitomi.

440 Zhuravleva et al. (2012) uses generated fractional Brownian motion (Gaussian) fields  
441 to mainly confirm their assumptions of allowing the conversion of 2D to 3D power  
442 spectra using a constant related to the projection emissivity factor. They examine  
443 artifical observations through the emissivity-weighted projected velocity field (line  
444 centroid) and the velocity dispersion (line broadening). This has several problems, as  
445 literature reviewed earlier suggests; it is unknown whether the ICM is homogeneous  
446 and isotropic with a Kolmogorov (essentially assumed with their generated fBM fields)  
447 or whether the stratification and magnetic fields add enough anisotropy to disrupt  
448 this assumption at the resolution capabilities of current/near-future telescopes. Sec-

ondly, their density field is assumed to be the large scale density distribution (Arnaud 2009), so it ignores the small scale density fluctuations present in the ICM. Z<sub>one</sub> et al. (2016) examines the capabilities of the soon to be launched XRISM (XRISM Science Team 2020) X-ray spectroscopic telescope under idealized assumption through generated fractional Brownian motion (Gaussian) fields. They expect the telescope will be able to measure the Mach number and injection scales of the turbulent spectra but will not be sensitive enough to determine the dissipation scale or the slope of the power spectra in the inertial range unless it is extremely deviated from the expected range defined in turbulence literature.

Li et al. (2020) examine the H $\alpha$  Filaments in Persus, A2597, and Virgo galaxy clusters and produce their first order line-of-sight velocity structure functions computed in the core region, outer region and all. These structure functions tend to show peak bumps at scales proportional to the AGN jets, with more increasing further on corresponding to scales approaching large scale mixing (say, from galaxy cluster/group mergers). The produced structure functions have steeper slopes than the Kolmogorov  $\ell^{1/3}$ , shown as  $\ell^{1/2}$  for Perseus and Abell 2597 and even steeper for Virgo. Figure 9 shows these first order line-of-sight velocity structure functions of Persus, Abell 2597 and Virgo galaxy clusters (blue, orange and red respectively). The shaded regions indicate results obtained from X-ray Chandra data of Coma and Perseus clusters (purple and green respectively) which show remarkable agreement with the filament data. The grey dashed lines shows the dissipation scales of the same DNS simulation shown in the Zhuravleva et al. (2019) plot (Figure 5). These structure functions have steeper slopes than the Kolmogorov  $\ell^{1/3}$  at scales less than the expected Spitzer scales. They suggest the steep slopes could arise from the magnetic field tension, turbulence instabilities, unique features of intermittent AGN feedback, or projection effects: close sky-plane pixels may be separated by large distances in the line-of-sight direction which would affect smaller scales more. Figure 10 shows a similar image to Figure 9, but haven't scaled by the Kolmogorov scale. It shows the Perseus structure functions (inner, outer and all regions as red, green and blue respectively) along with constraints from the Hitomi telescope Hitomi Collaboration et al. (2016, 2018) which directly measured the velocity dispersion in the Perseus cluster, where the green and red regions are for the outer and inner regions respectively. The purple Chandra region shows the surface brightness fluctuations of the outer region (as there are large X-ray cavities in the inner Perseus cluster region), so this probes a similar outer region as the filaments. Remarkably, the Chandra surface brightness fluctuations, Hitomi observations, and first order structure functions appear to agree with one another.

Hu et al. (2022) examine the same Perseus (NGC1275) filament structure as Li et al. (2020) but separates the filaments into regions and compares results to high resolution simulations of galaxy filaments. They suggest the presence of supersonic turbulence structures through examining projected velocity structure function slopes of  $\gamma_2 = 1/2$  at scales  $\leq 2\text{kpc}$  in their simulations and Perseus filaments. Beyond

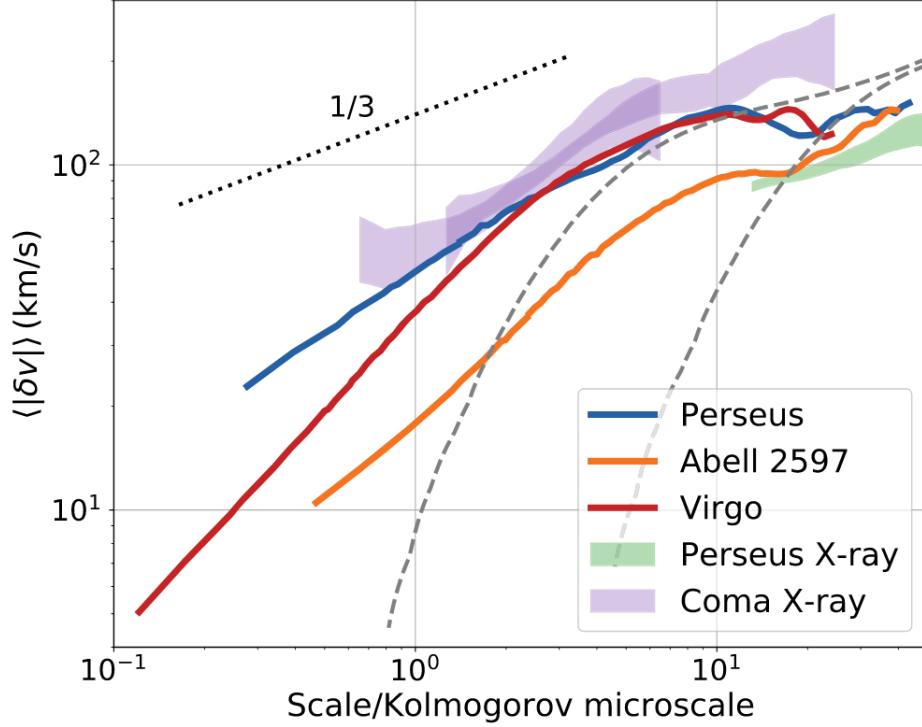


**Figure 9.** Figure from Li et al. (2020), showing the first order line-of-sight velocity structure function of the H $\alpha$  Emission of Perseus, Abell 2597 and Virgo galaxy clusters (blue, orange and red lines respectively). The shaded regions indicate results obtained from X-ray Chandra data of Coma and Persus (purple and green respectively). The dashed grey line shows the dissipation scales of a DNS simulation. The dotted black line is Kolmogorov  $k^{1/3}$  power law slope.

those scales, the velocity structure function depends on the radial gradient which has a slope of  $\gamma_2 = 1$ . They argue, for hot outflows with short cooling timescales, the turbulent velocity structure can be frozen in the cold gas and the velocity structure function power law is  $\gamma_2 \geq 1/2$  for gas originating from supersonic flows and  $\gamma_2 \approx 1/3$  for subsonic flows. At large scales, the slope is determined by the velocity gradient along the filament which depends on the viewing angle.

Figure 12 (obtained from Mohapatra et al. (2022b)) shows the second order velocity structure functions computed with MHD and HD (purple and blue, respectively) projected data (diamonds and squares) and full 3D data (stars and circles). The power law fits are shown with the 3D HD power law  $m = \gamma_{3,HD} = 0.67 \approx 2/3$  and its projected power law  $m_{proj} = \gamma_{2,HD} = 1.35 < \gamma_{3,HD} + 1 = 5/3$ . The MHD simulation has a similar case, the 3D power law is  $m = \gamma_{3,MHD} = 0.57 \lesssim 2/3$  with its projected power law  $\gamma_{2,MHD} = 1.3 < \gamma_{3,MHD} + 1$ . For both of the simulation structure function projections, they have a steeper power law (by approximately  $\gamma_2 \approx \gamma_2 + 0.7$ ), which is less than the expected factor of 1 (Appendix C). Using the equivalent energy spectrum formula (Appendix A), the omni-directional spectrum would have power laws  $\beta_{2,MHD} = \gamma_{2,MHD} + 1 \approx 2.3 \neq 8/3$  and  $\beta_{2,HD} = \gamma_{2,HD} + 1 \approx 2.35 \approx \gamma_{2,MHD} \neq 8/3$  and the modal spectrum power laws will be  $\alpha_{2,HD} \approx \alpha_{2,MHD} \approx \beta_2 + 1 \approx 3.35 \neq 11/3$ .

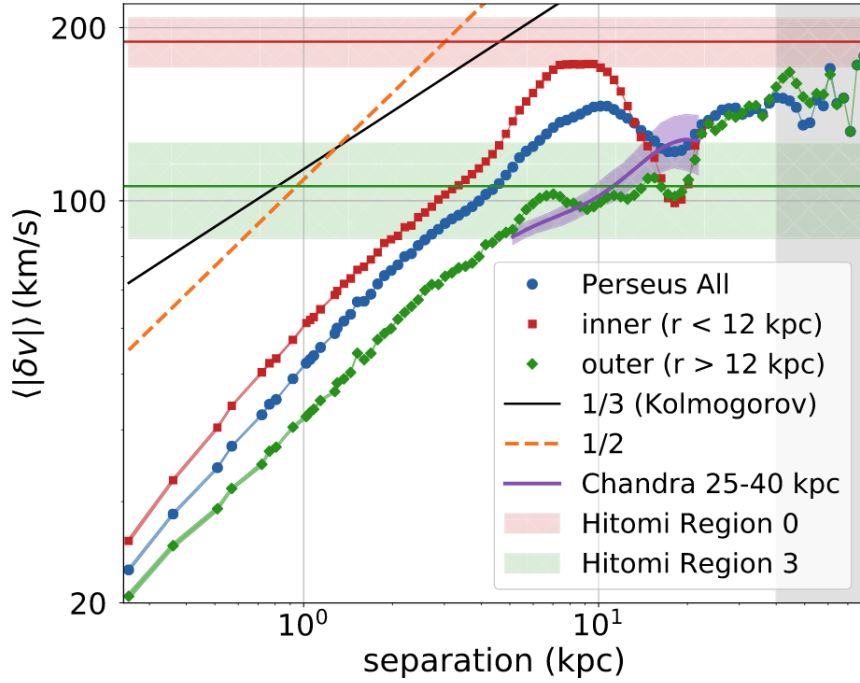


**Figure 10.** Figure from Li et al. (2020), showing the first order velocity structure functions from H $\alpha$  velocity centroid observations in the inner, outer and all (red, green and blue), the constraints from the Hitomi telescope in the inner and outer regions (red and green horizontal bars), and the velocity structure function of the outer region X-ray surface brightness fluctuations from Chandra in purple.

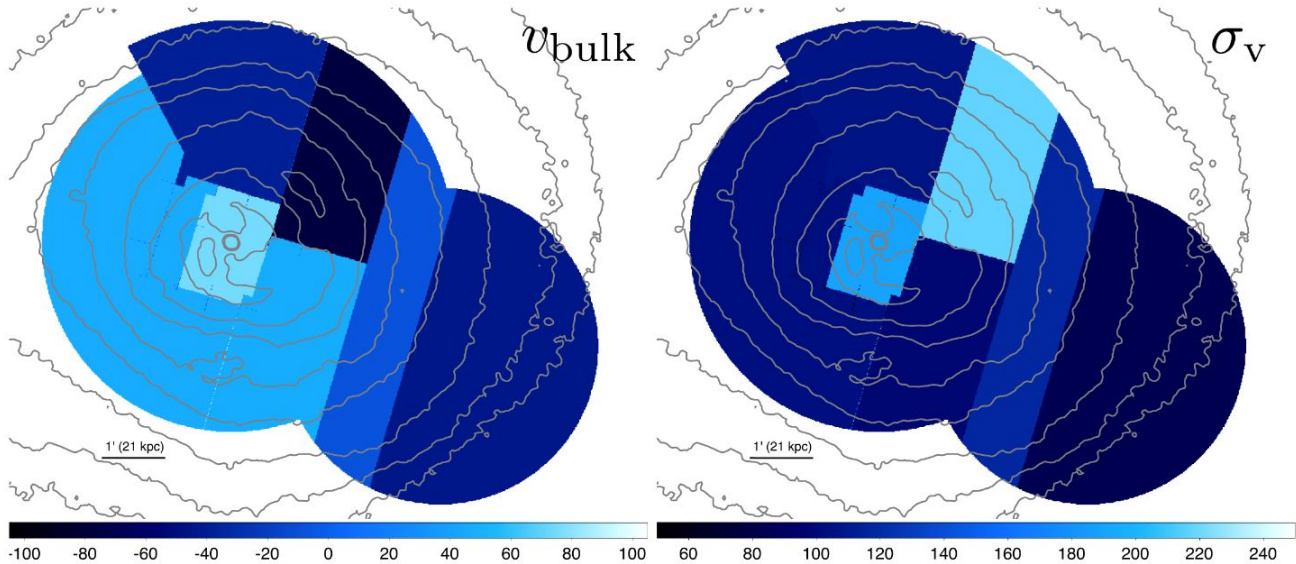


**Figure 11.** Figure from Hitomi Collaboration et al. (2018), showing the partial observation from Hitomi of Perseus cluster. The left image shows the bulk line-of-sight velocity and the right image shows the line-of-sight velocity dispersion. Both images are overlaid with X-ray contours from Chandra.

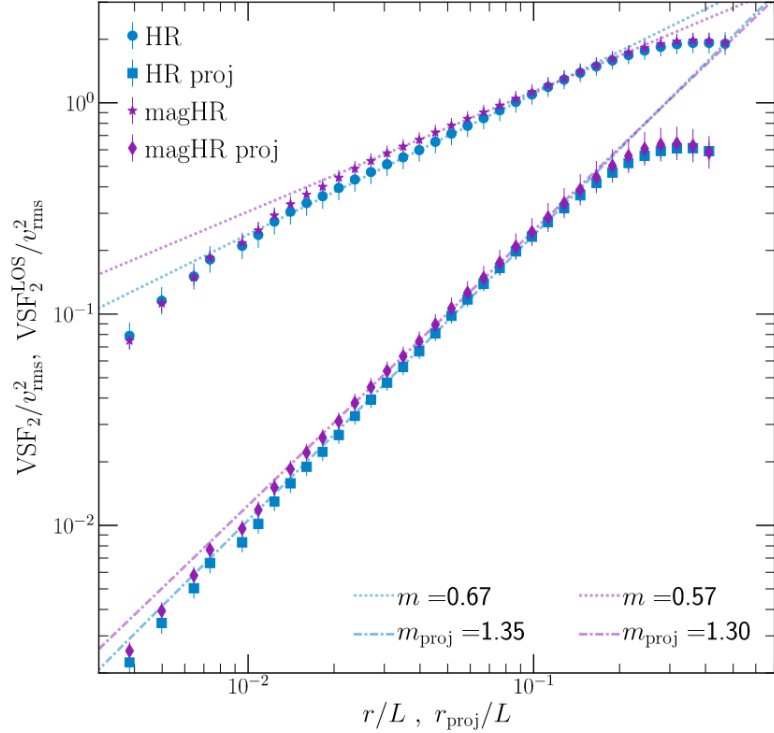


**Figure 12.** Figure from Mohapatra et al. (2022b), showing the projected second order velocity structure function as a function of lag  $r$ , of an HD and MHD simulation (blue squares, purple diamonds respectively) and the full 3D second order velocity structure functions for the HD and MHD simulations (blue circles, purple stars respectively). The power law fits are also shown, with the 3D HD power law  $\gamma_{3,HD} \approx 2/3$ , projected HD power law  $\gamma_{2,HD} \approx 1.35 < 5/3$ . Similarly, the MHD power laws are  $\gamma_{3,MHD} = 0.57 \sim 2/3$  and  $\gamma_{2,MHD} = 1.3$  for the 3D and projected data respectively.

Figure 13 (obtained from Mohapatra et al. (2022b)) shows the projected first-order velocity structure functions of the cold-phase as the filled in shapes for different projection weightings (mimicking  $H_\alpha$  emission line filaments) and the  $H_\alpha$  first-order velocity structure functions from filament observations of 3 different galaxy clusters (Li et al. 2020). The observations roughly agree with the slopes of the simulations at large lags, but are much steeper at smaller lags.

The is a wealth of techniques developed for interstellar turbulence, some of these techniques have already been converted to ICM techniques such as the Arevalo method Arévalo et al. (2012) for computing the power spectrum from scale-space, is derived from structural analysis of interstellar clouds Ossenkopf et al. (2006a, 2008). Koch et al. (2019) provides a nice breakdown of a whole host of different methods for extracting interstellar turbulence statistics based of Doppler shift measurements such as: the velocity channel analysis (VCA) and velocity coordinate spectrum (VCS), which analyse spectral-line cubes integrating over spectral coordinate and spatial coordinate respectively. Brunt et al. (2003); Brunt & Mac Low (2004) generate synthetic observations (projections) of interstellar turbulence based on simulations; examining the relationship between projected velocity statistics and the true 3D power spectrum

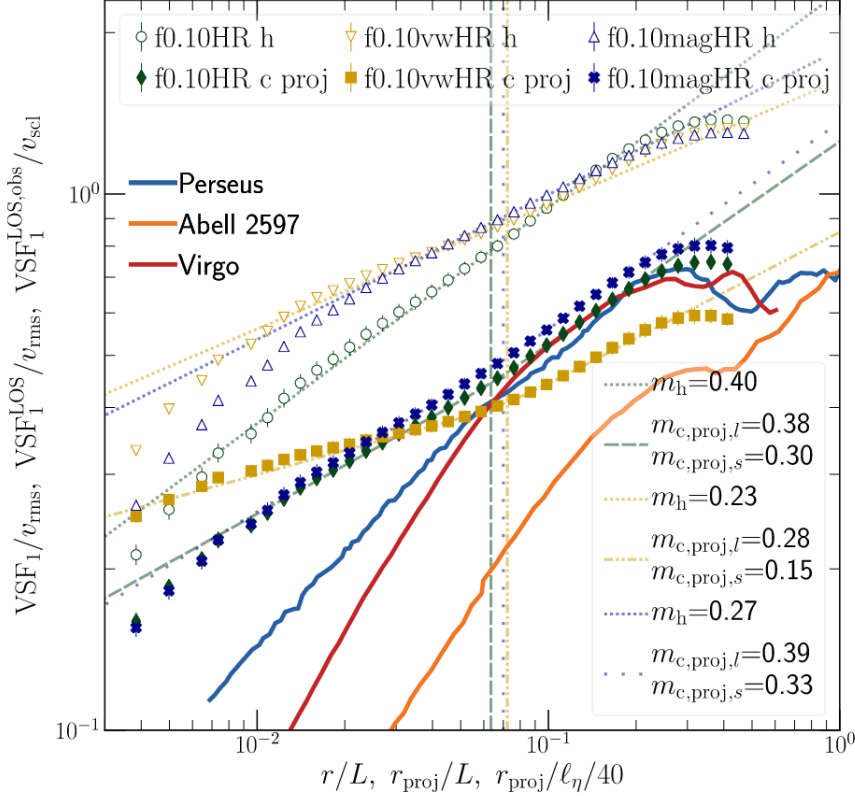


**Figure 13.** Figure from Mohapatra et al. (2022b), combining the observations from Li et al. (2020) (orange, red, and blue lines) and simulation data from Mohapatra et al. (2022b). Even with the projection, the simulations (filled in diamonds, squares and crosses) do not exhibit the same slopes as the observed data.

using the techniques of principle component analysis (PCA) and line centroid (LC) variation. They find differences in the projected versus 3D statistics, providing a relation between the 2D and 3D power law slopes with empirically derived modifications that are dependent on the turbulence properties.

## 2.6. Summary

In summary, the ICM observables are the following

$$RM(\boldsymbol{\theta}) \propto \int B_\ell(\boldsymbol{\theta}, \ell) \epsilon_{RM}(\boldsymbol{\theta}, \ell) d\ell \quad (21)$$

$$\mathcal{V}_{LC}(\boldsymbol{\theta}) \propto \int V_\ell(\boldsymbol{\theta}, \ell) \epsilon_{LC}(\boldsymbol{\theta}, \ell) d\ell \quad (22)$$

$$I_X(\boldsymbol{\theta}) \propto \int \rho_e(\boldsymbol{\theta}, \ell)^2 \epsilon_X(\boldsymbol{\theta}, \ell) d\ell \quad (23)$$

$$Y_{SZ}(\boldsymbol{\theta}) \propto \int P_e(\boldsymbol{\theta}, \ell) \epsilon_{SZ}(\boldsymbol{\theta}, \ell) d\ell \quad (24)$$

where we have the projected magnetic field from rotation measure (RM), velocity field from emission line centroids (LC) (and other techniques briefly mentioned in the

section above), electron density squared from X-ray and electron pressure from SZ effect. These are all projected along with their respective emissivity, where typically:

$$\epsilon_{RM} = \rho_e(\boldsymbol{\theta}, \ell) w_{RM}(\boldsymbol{\theta}, \ell) \quad (25)$$

$$\epsilon_{LC} = \rho(\boldsymbol{\theta}, \ell) \quad (26)$$

$$\epsilon_X = n_e n_i \Lambda(T) \quad (27)$$

$$\epsilon_{SZ} = n_e n_i \Lambda(T) \quad \text{Not the same as X-ray?} \quad (28)$$

where the function  $w_{RM}(\boldsymbol{\theta})$  is a window function describing the Faraday screen (in our case, the ICM) for a polarization source which could exist far in the background.  $\Lambda(T)$  is the temperature dependant cooling function (Sutherland & Dopita 1993), describing the rate of cooling based off emission (this also will depend on the metallicity of the ICM). Of particular interest is the X-ray and SZ effect surface brightness observations ( $I_X, Y_{SZ}$ ) because they haven't been looked at in as much rigorous detail as the rotation measure observations and velocity (obtained from Doppler shift measurement) observations (at least, for interstellar turbulence, although it is likely a lot of the same principles can be applied to the ICM). These quantities are interesting because:

- The  $I_X$  term is the projection of the density *squared* which can bias it towards to the denser central regions of the cluster.
- The X-ray and SZ images don't natively return the fluctuations, they have to be modelled by subtracting the observation from an assumed mean distribution.
- X-ray and SZ signals are not necessarily aligned (van Weeren et al. 2019).
- The availability of observation; the H $\alpha$  Filaments and RM are not present or covering every cluster, and  $Y_{SZ}$  might not be available for clusters with a strong AGN.
- X-ray and SZ effect observations have different angular resolutions; the SZ effect observations have a very large angular resolution meaning it sees primarily the large scale structure.
- The X-ray and SZ images have the ability to trace the 3D velocity distribution (without making isotropic assumptions) compared to the velocity and magnetic field measurements providing just the line-of-sight components.
- The literature suggests the SZ effect is the better method for constraining turbulent velocities.

These quantities have the following issues in the literature:

- There is a steepening in some of the observations and in some simulations but not necessarily matching the rates and the scales.

- 573     • Similarly, there is debate whether the ICM should follow a Kolmogorov slope or  
574        not, some idealized simulations reproduce Kolmogorov slope spectra (although  
575        not matching the Kolmogorov turbulent physics) and others find spectral slopes  
576        matching different turbulent physics like stratified buoyancy driven or super-  
577        sonic.
- 578     • Where are the dissipation scales? Estimates of the collisional viscosity and  
579        mean-free path ([Spitzer 1962](#)) would indicate a *small* Reynolds number and  
580        large dissipation scale which is not observed. Simulating all of the physics across  
581        all possible scales in the ICM is impossible, so phenomenological arguments  
582        are often made (say, ignoring the magnetic fields and/or stratification), which  
583        could bias results. The density and pressure could be passively scaled quantities  
584        ([Corrsin 1959](#); [Brandenburg & Nordlund 2011](#); [Brandenburg & Lazarian 2013](#)),  
585        taking a spectral slope determined by large scale buoyancy driving; modelling  
586        the stratification is important. Projection effects could create cancellations on  
587        the small scales where the magnetic field is dominant.
- 588     • Where and what are the driving scales? Cluster mergers and mass accretion  
589        and AGN feedback are the typical sources assumed for large scale turbulence  
590        driving ([Simionescu et al. 2019](#)), but their exact mechanisms of energy transfer  
591        to the surrounding fluids are relatively unknown.
- 592     • More work needs to be done on understanding the contributions to the retrieved  
593        turbulence spectra from noise, exposure and projections.

594

### 3. RESEARCH QUESTIONS

595

The aim of my thesis is to understand the mechanisms behind the projection of turbulence variables (velocity field, magnetic field, density and pressure) with the main focus on the density (squared) and pressure projections corresponding to the X-ray and SZ effect (surface brightness) observations respectively. The following questions will lead in achieving this aim:

596

- How do the full 3D statistics compare to projected statistics? What information is lost and what can be retrieved?
- What effect does the usage of different statistical measures and methods have on the retrieved turbulence information?
- How does different turbulence behaviour show up in the observed statistics? Is the stratification important? and what about the magnetic fields?

600

601

602

603

604

605

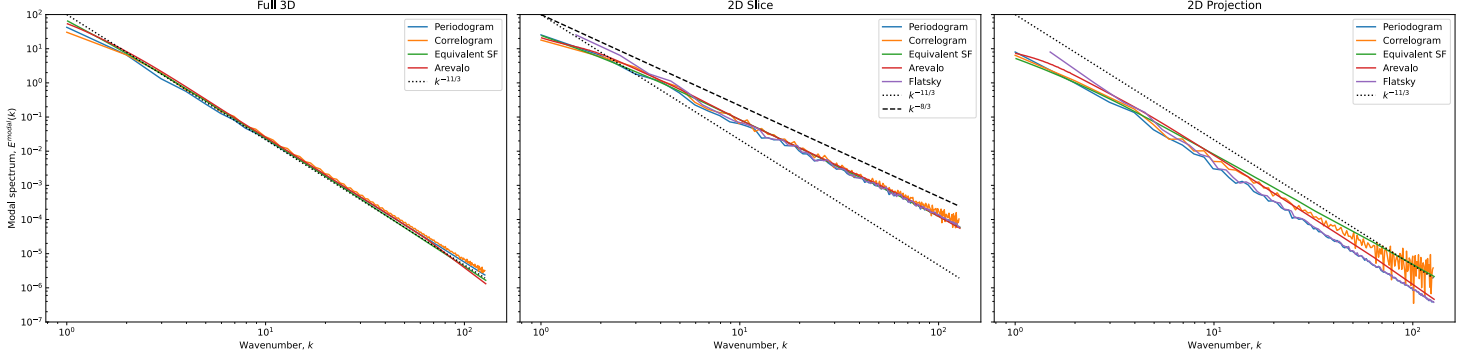


**Figure 14.** Comparing the modal spectra on a 3D generated fBM field with a modal power law of  $\beta_3 = 11/3$  (left), a 2D slice of the same fBM field (middle), and the 2D projection (right) for the different methods: Periodogram (blue), correlogram (orange), equivalent structure function (green), Arevalo (red), and flatsky (purple).

#### 4. SIMULATIONS & PRELIMINARY RESULTS

This section will describe the progress I have made thus far and future steps I will take to achieve my research goals. A lot of the work accomplished so far has been to implement the methods currently present in the code-base ([Implementation details](#)); understanding the different normalizations of the power spectrum methods to make them comparable.

##### 4.1. Gaussian fields

We make use of fractional Brownian motion (Gaussian) fields generated such that its power spectrum has a determined power law value. This is useful for testing (see [Appendix C](#)) and could potentially be useful for the projected methods as the line-of-sight integration potentially destroys the turbulent intermittency information (which is described in the complex phase). So fBM fields are often used in examining properties of projected turbulence ([Enßlin & Vogt 2003](#); [Vogt & Enßlin 2003, 2005](#); [Koch et al. 2019](#)).

[Figure 14](#) shows the modal spectra of a three-dimensional fBM field with a power law of  $k^{11/3}$ . The left panel shows the spectra calculated for the full three-dimensional cube and then binned for plotting; the different power spectrum estimation methods are consistent and following the expected power law slope. The middle panel shows the spectra calculated from a 2D slice of the 3D fBM cube; the different methods are also consistent in this case, but following a slope of  $8/3$  which is expected for the 2D slice. The right panel shows the methods for the 2D projection of the 3D cube; now there is deviation in the methods. The flat-sky and periodogram (blue and purple) are similar (with discrepancy resulting from different wavenumber vector binning methods). The methods mostly follow the expected powerlaw of  $11/3$  with deviation in the equivalent structure function and correlogram methods (green and orange) at large wavenumbers. Overall, there is an expected decrease in the energy from the full 3D spectra to the 2D slice and 2D projection: the slice and projection do

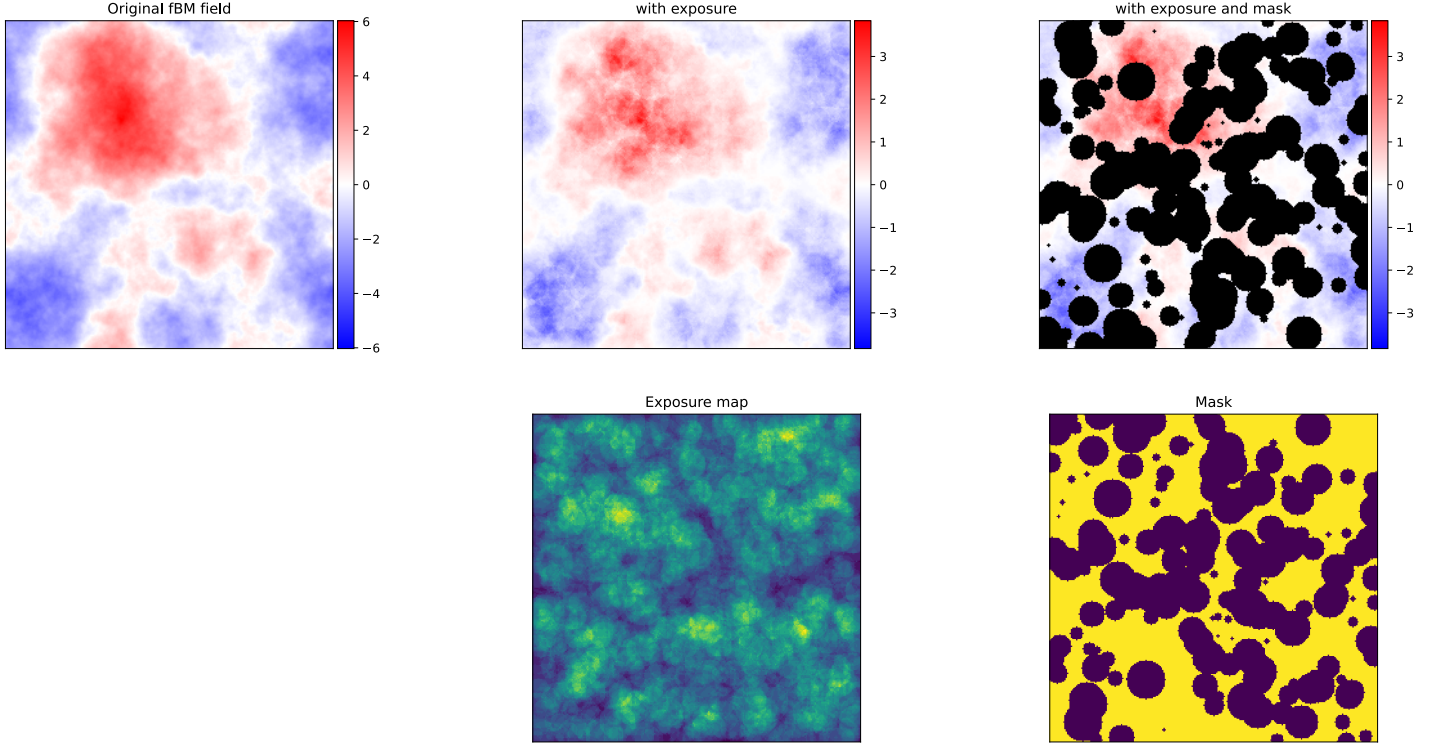


**Figure 15.** A figure demonstrating an fBM fluctuation field (projected or otherwise) in the top left. The middle column shows the fBM fluctuations multiplied by the corresponding randomly generated exposure map, mimicing a telescope observation where certain regions have been observed for longer periods than others. The last column shows the fBM fluctuations with the exposure map with a randomly generated mask added; the mask acts to remove regions where there would ordinarily be contaminations from bright sources in real observations.

not contain all of the energy information of the 3D data cube. More work is required to understand what is causing the differences in the slopes for the 2D projection.

As discussed in section 2 (Churazov et al. 2012), X-ray observations typically require an exposure normalization, masking and noise reduction. A true observed image has changing exposure depending on the observation times and telescope design, so the underlying turbulence field may be observed inconsistently which could disrupt spectrum calculations. Sharp jumps from pixel values to zeros in masked regions can also cause artefacts during the Fourier transform. Figure 15 shows the process of adding an exposure map and a mask to an fBM fluctuation image. This will be needed to more accurately test the observation process; the underlying turbulent field is observed with variation in each pixel observing time (due to telescope limitations), which will change the apparent power spectrum. The Arevalo method and flat-sky methods provide mechanisms for dealing with masking (and therefore exposure maps). Secondly, the mask is required in observations to remove contaminating sources like bright galaxies and stars in the foreground/background or regions of discontinuity. Whilst our fluctuation images won't have regions of contamination, the mask could be required for testing to break the Fourier periodicity which could add bias to the

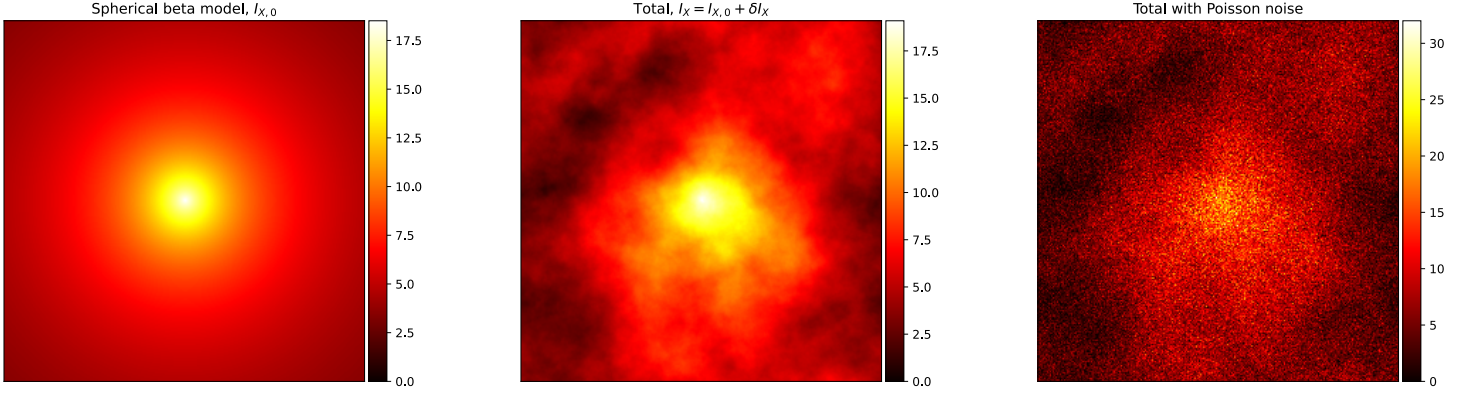


**Figure 16.** A figure demonstrating the procedure for adding Poisson noise to an image. For a generated 2D fBM field (projected or otherwise), first generate a spherical beta model (left). Next, add that beta model to the fBM fluctuations to get the total observed image (middle). The right figure shows the total image (fluctuations with the mean) with generated Poisson noise, where each pixel value in the original total image specifies the mean (and also standard deviation) of the Poisson noise distribution to sample from.

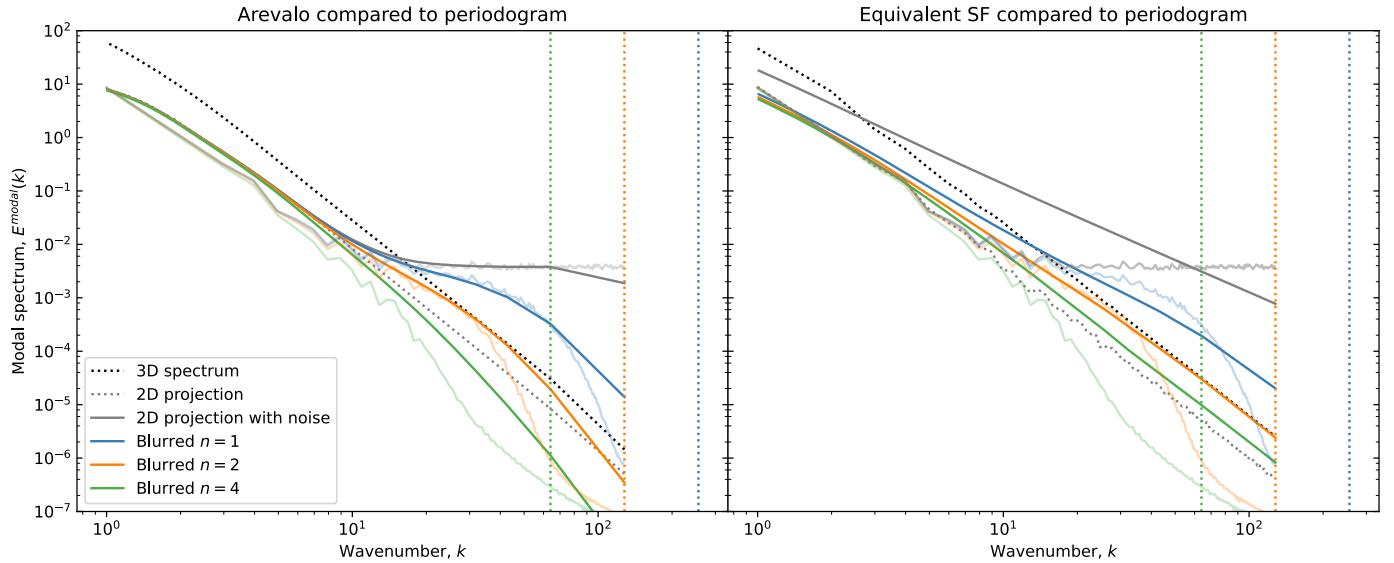


**Figure 17.** The full 3D modal spectrum (dotted black), 2D projection (dotted gray), and 2D projection with noise (solid gray). The blue, orange and green solid lines indicate the Gaussian blurred forms of the 2D projection with noise, with the scales indicated by the vertical dotted lines of each respective colour. The faint solid lines show the periodogram; the solid lines are the Arevalo method on the left plot and the equivalent structure function method on the right.

obtained spectra. For future, the full test will be to add a beta model, then add the exposure map, then add noise to the image, and lastly apply the mask.

Figure 16 shows a fluctuation image with a spherical beta model added, and then Poisson noise is added where each pixel in the total image is the mean of the Poisson noise distribution for that pixel. To obtain a noisy fluctuation image, the same beta model can be subtracted from the total noisy image.

656    [Figure 17](#) shows the modal power spectra derived from a 3D fBM field. The dotted  
 657 black line shows the 3D modal spectrum, with its 2D projection in dotted gray and  
 658 with noise added via the process shown in [Figure 16](#) in solid gray. The noise is  
 659 modelled with Poisson noise which is constant in Fourier space. Therefore, at small  
 660 wavenumbers, the normal spectrum can be seen. At large wavenumbers, the spectrum  
 661 will converge to the constant Poisson noise floor. The noisy fluctuation image is then  
 662 smoothed via a Gaussian blur at three different levels (sigma values) indicated by  
 663 the vertical dotted lines, their spectra are in blue, orange and green for  $\sigma = 1, 2, 4$   
 664 respectively. The faint solid lines are for comparison to the periodogram methods  
 665 whereas the solid lines is calculated from the Arevalo method (left) and equivalent  
 666 structure function method (right). The Arevalo method performs better with the  
 667 larger smoothing ( $\sigma = 2, 4$ ) but does not retrieve the original 2D projected spectrum  
 668 at large wavenumbers. The equivalent structure function method manages to retrieve  
 669 the original spectrum well for  $\sigma = 4$ , with a bias in the energy at large wavenumbers  
 670 but an apparent similar power law.

#### 671    4.2. Provided simulation data

672    The next step has been to use provided simulation data. The first; an *incompressible*,  
 673 isotropic, MHD simulation and the second; an *compressible*, isotropic, MHD  
 674 simulation. Using real simulation data is important because the fBM/Gaussian fields  
 675 are not *turbulent*, they simply share expected turbulent properties of an inertial range  
 676 power law. In other words, the fBM fields do not contain information about couplings  
 677 and intermittent structures between the magnetic, velocity and density fields, there-  
 678 fore simulations are required.

##### 679    4.2.1. Incompressible MHD

680    The incompressible, isotropic, MHD simulation does not have information about the  
 681 density so we make use of a single component of the velocity field for the following  
 682 plots.

683    [Figure 18](#) shows the omni-directional (left) and modal periodogram spectra (right)  
 684 of the full 3D (solid black), 2D slice (solid gray) and 2D projection (dashed gray)  
 685 spectra of the incompressible MHD simulation data. Superimposed in dotted black is  
 686 the expected power law for each spectra. As expected, the omni-directional spectrum  
 687 of the 3D and 2D slice data have the same Kolmogorov  $k^{-5/3}$  powerlaw whereas  
 688 the 2D projection has a powerlaw of  $k^{-8/3}$ , a factor of  $k^{-1}$  due to the difference in  
 689 the shell/annulus integrations. Similarly, the modal spectra of the 3D data and 2D  
 690 projection share a  $k^{-11/3}$  power law and the 2D slice has a  $k^{-8/3}$ , shallower by a factor  
 691 of  $k$ .

692    [Figure 19](#) compares the different spectrum calculation methods for the incompressible  
 693 MHD simulation for the full 3D spectrum (of the line-of-sight component of the  
 694 velocity field), a 2D slice perpendicular to the line-of-sight, and the 2D projection.  
 695 The differences now are more pronounced than [Figure 14](#). The different methods show

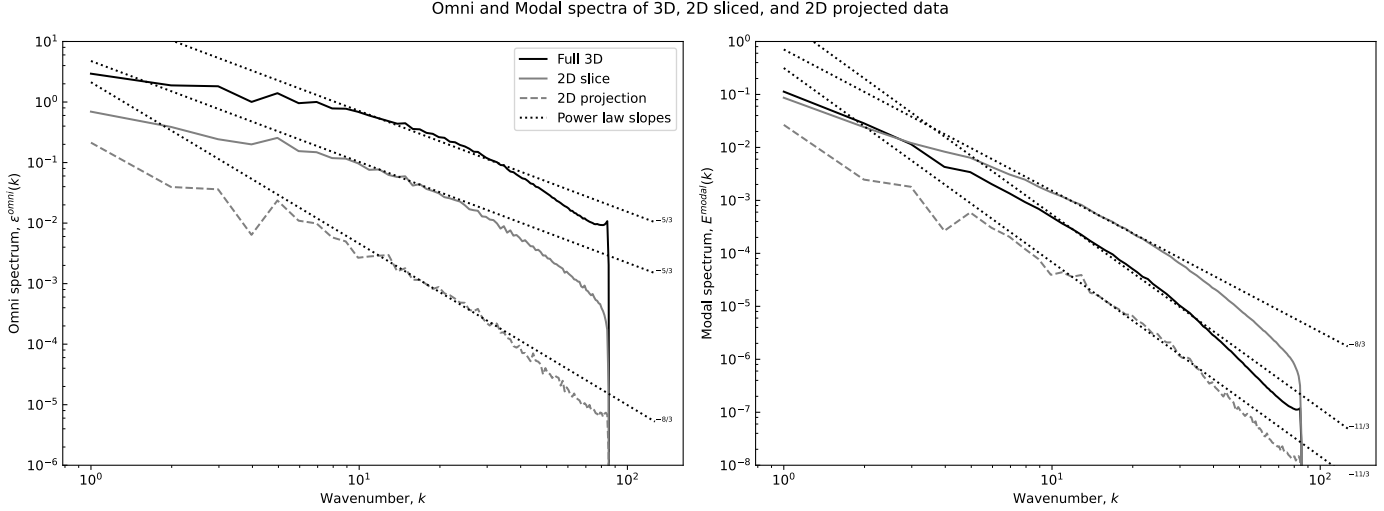


**Figure 18.** Omni-directional (left) and modal (right) periodogram spectra made showing the same relations to Figure 36 (Projections) for the full 3D spectra (solid black), 2D slice (solid gray) and 2D projections (dashed gray). As expected, the full 3D and 2D slice omni-directional spectra have the same  $5/3$  powerlaw whereas the 2D projection has a steeper slope by a factor of  $k$ . Likewise, the full 3D and 2D projection have the same modal spectrum power law and the 2D slice has a shallower slope by a factor of  $k$ .

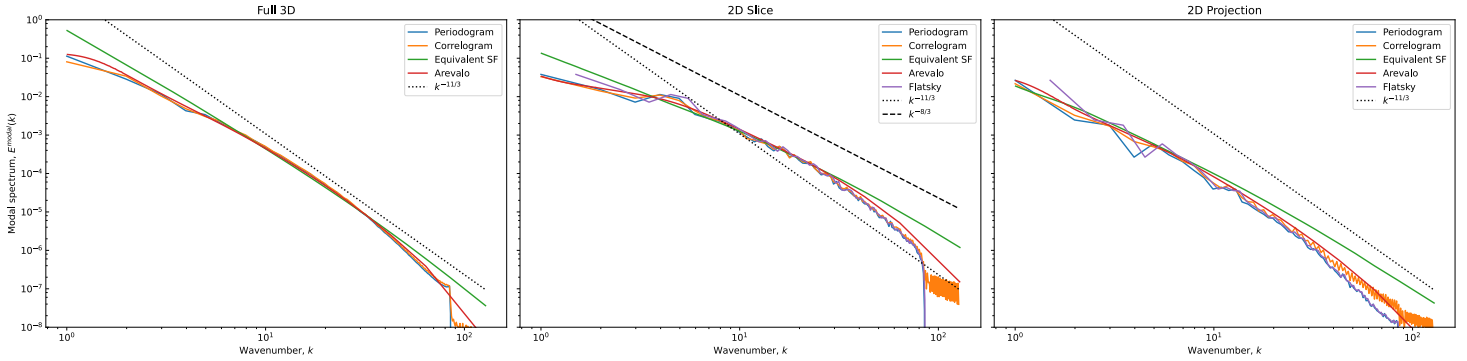


**Figure 19.** Comparing the modal spectra on the line-of-sight component of the velocity vector for an incompressible MHD simulation (left), a 2D slice (middle), and the 2D projection (right) for the different methods: Periodogram (blue), correlogram (orange), equivalent structure function (green), Arevalo (red), and flatsky (purple).

similar inertial range power law behaviour for both the full 3D and 2D slice spectra, although the Arevalo method (red) and equivalent structure function method (green) show deviations at large wavenumbers for the 2D slice spectra. This deviation is made stronger for the 2D projections, the equivalent structure function method shows a large deviation from the inertial range power law (and from the other methods). Once again, more work is required to understand and quantify these differences.

Figure 20 compares, for increasing projection distances  $d$  the 2D projected spectra  $E_{d,2D}$  to the full 3D spectrum  $E_{3D}$  of a velocity component along the respective line-of-sight (blue, orange and green for  $x, y, z$  respectively). The projection distance is the number of line-of-sight slices included in the projection measurement, *i.e.* a 2D

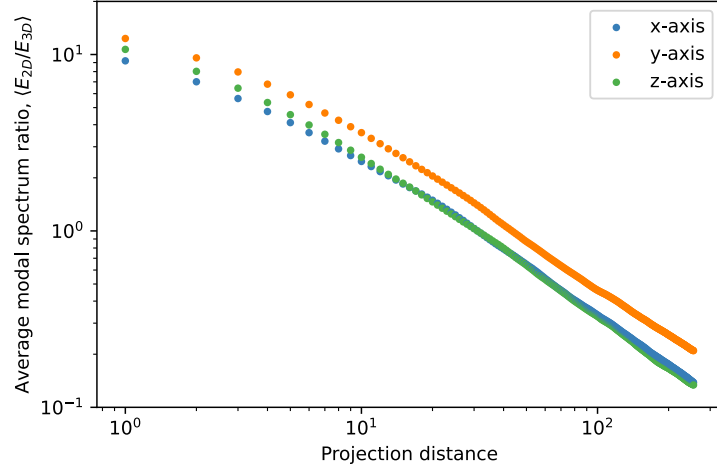


**Figure 20.** Comparing the 2D projection modal spectrum to the full 3D spectrum. The ratio of each wavenumber of  $E_{2D}$  and  $E_{3D}$  is taken and the average is plotted for each projection distance of a 3D data cube. The blue, orange and green indicate the  $x, y, z$ -axis projection and component of the velocity field taken respectively.

projection of a projection distance of 2 is the average of 2 line-of-sight pixels for each pixel in the sky-plane. This is interesting to look at as different projection distances will be in different states of line-of-sight cancellations. For the compressible MHD simulation, this relation is approximately  $d^{-1}$  for projection distances  $d > 10$ . This would mean, in order to scale the 2D projection spectra back into the 3D spectra via

$$CdE_{d,2D}(k) \approx E_{3D}(k) \quad (29)$$

for some constant  $C$ , which is expected (see the discussion for Figure 23).

#### 4.2.2. Compressible MHD

This simulation is a compressible MHD simulation, so contains a density field. Now, we can compare the density (and density squared) projection spectra to the 3D density spectrum and the 3D velocity spectrum. Figure 21 shows the full 3D, 2D slice and 2D projected (left, middle and right respectively) modal spectra for the line-of-sight component of the velocity for the compressible MHD simulation. Due to limitations in the resolution, the inertial range is small (Wan et al. (2010)), but we can still examine the inertial range behaviour of the different methods. Once again, the 3D spectrum shows minimal differences for the different methods in the inertial range (approximately wavenumbers 4 – 20), however, there are large differences between all methods at large wavenumbers and between the equivalent structure function and the others at the small wavenumbers. It is a similar story for the 2D slice spectra, now with the flat-sky method following the periodogram and the structure function exhibiting a shallower power law than expected in the inertial range. For the 2D projections, the expected power law ( $k^{-11/3}$ ) inertial range appears to have decreased (to approximately wavenumbers 5 – 10); now, there is a steepening after wavenumber  $\approx 10$  for the periodogram, correlogram and flat-sky methods. The Arevalo method

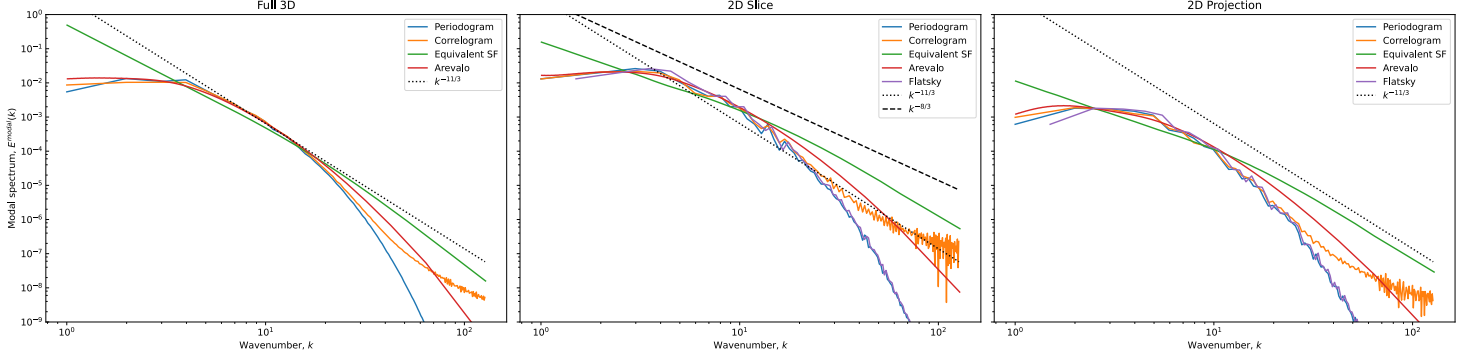


**Figure 21.** Comparing the modal spectra on the line-of-sight component of the velocity vector for a compressible MHD simulation (left), a 2D slice (middle), and the 2D projection (right) for the different methods: Periodogram (blue), correlogram (orange), equivalent structure function (green), Arevalo (red), and flatsky (purple).

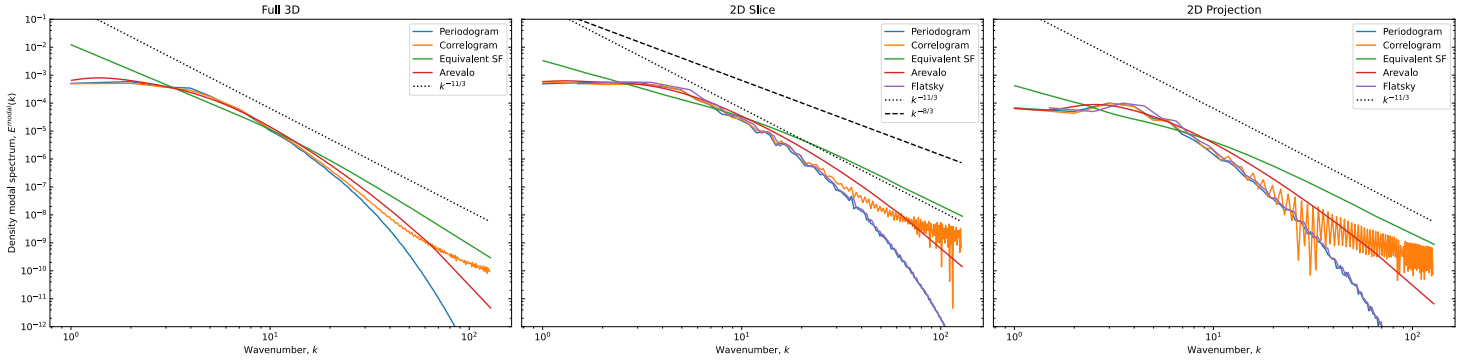


**Figure 22.** Comparing the modal spectra on the density for a compressible MHD simulation (left), a 2D slice (middle), and the 2D projection (right) for the different methods: Periodogram (blue), correlogram (orange), equivalent structure function (green), Arevalo (red), and flatsky (purple).

731 appears to display the power law from wavenumbers  $k \approx 6 - 20$ . The equivalent  
 732 structure function does not agree with the other methods. Similarly, Figure 22 shows  
 733 the full 3D, 2D slice and 2D projection density spectra. They appear similar to the  
 734 velocity component spectra albeit with a smaller amplitude. The differences lie in  
 735 the 2D slice where the inertial range periodogram, correlogram, flat-sky and Arevalo  
 736 methods appear to follow the  $k^{-11/3}$  power law instead of the expected  $k^{-8/3}$ . The  
 737 density spectra for the 2D projection appears to have a power law steeper than  $k^{-11/3}$   
 738 for the periodogram, correlogram and flat-sky spectra. The Arevalo method appears  
 739 to show the expected power law and the equivalent structure function has a shallower  
 740 slope.

741 Figure 23 compares the 2D projected spectra to the full 3D spectra for the velocity  
 742 components (left) and density field (right). Compared to Figure 20, the relation is  
 743 not smooth, especially note the jump at around projection distance  $d \approx 100$  for the  
 744  $y$ -axis projections. Also note, the sharp change in slope in the  $z$ -axis density ratio at  
 745  $d \approx 40$ . Once again, these relations require more investigation but will be important

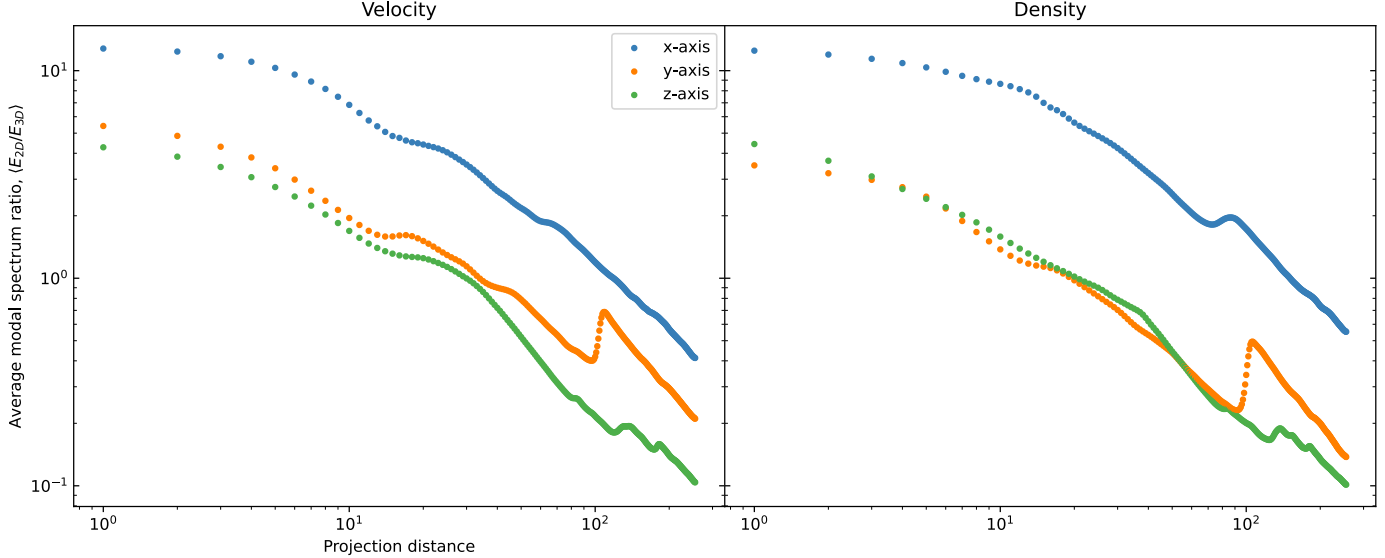


**Figure 23.** Comparing the 2D projection modal spectrum to the full 3D spectrum. The ratio of each wavenumber of  $E_{2D}$  to  $E_{3D}$  is taken and the average is plotted for each projection distance of a 3D data cube. The blue, orange and green represent projections of the  $x, y, z$ -axis respectively and the relevant component of the velocity. The right plot shows the projected velocity components compared to the respective full 3D velocity component. The right plot shows the projected density spectrum compared to the 3D density spectrum.

to investigate due to the following relation commonly stated in the literature

$$\frac{E_{2D}}{E_{3D}}(|\mathbf{k}|) \approx \int E_{\text{EM}}^{\text{modal}}(k_\ell) dk_\ell \quad (30)$$

where  $E_{\text{modal}2D}$ ,  $E_{\text{modal}3D}$  are the 2D and 3D modal spectra we are comparing and  $E_{\text{EM}}^{\text{modal}}(k_\ell) = |W(k_\ell)|^2$  is the projection weighting in Fourier space. In the current plot, the emissivity function  $\epsilon_d(\ell) = d^{-1}$  is constant for each projection distance  $d$ , meaning that its Fourier transform is a delta function

$$W(k_\ell) = \int \epsilon(\ell) e^{-ik_\ell \ell} d\ell = d^{-1} \delta(k_\ell) \quad (31)$$

which would imply that

$$E_{2D}(\mathbf{k}_\theta) = d^{-1} E_{3D}(\mathbf{k}_\theta, 0) \quad (32)$$

which is the *projection-slice theorem*.

#### 4.3. Observational Data

We have also begun to apply our methods to observational data to compare them and to help understand the current techniques in the literature (Churazov et al. (2012); Zhuravleva et al. (2019)). I have been given processed X-ray Chandra observations of the Coma cluster (Figure 24) and subtracted a spherical beta model to get the X-ray surface brightness fluctuation map which appears similar to the one

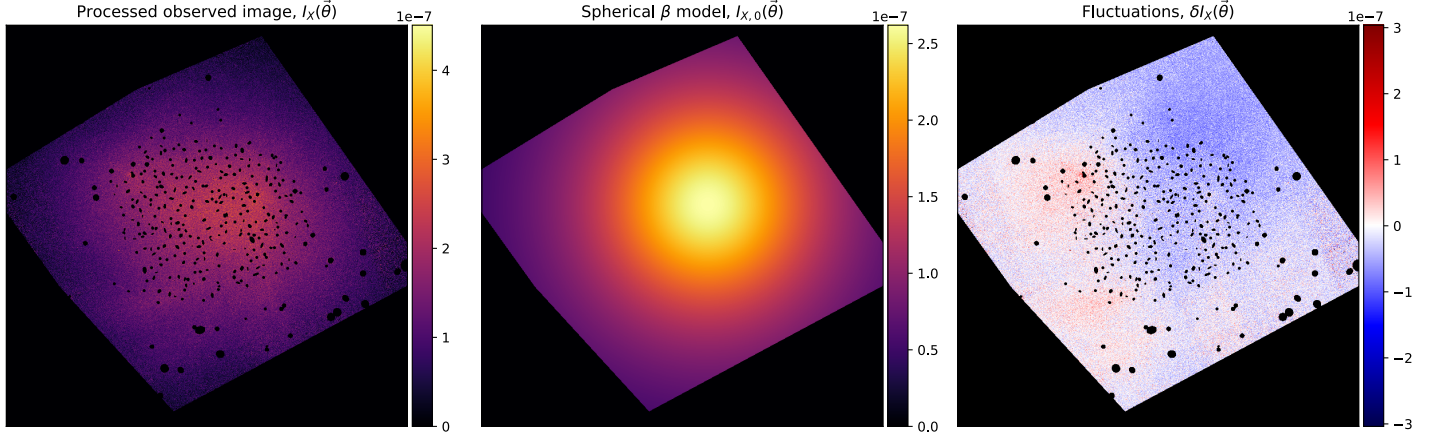


**Figure 24.** Left: filtered, normalized, subtracted flux of the Coma cluster from Chandra  $I_X$ ; this is a processed image to normalize with respect to the observational restrictions *i.e.* exposure. Only the core region of  $651 \times 651$ kpc has been selected. Middle: the generated spherical beta model  $I_{X,0}$ , chosen to represent the large-scale/mean distribution of the image. Right: the X-ray surface brightness fluctuations  $\delta I_X$  obtained by subtracting the processed observed image by the spherical beta model  $\delta I_X = I_X - I_{X,0}$ .

presented in Zhuravleva et al. (2019). Now, we can compute the spectra using the different methods, as shown in Figure 25. The black dots show the modal spectrum data of a Poisson noise-subtracted, Chandra, Coma cluster observation, extracted from Churazov et al. (2012) to compare our results with. The red, blue and green lines show the Flat-sky, periodogram and correlogram methods which agree with each other almost exactly; the difference with the flat-sky method is attributed to the differences in how the wavenumbers are binned, it is possible to modify my periodogram binning method to obtain the exact same shape (not shown). The Arevalo method (purple) show very similar behaviour to the periodogram (and others) albeit smoother, with some discrepancy at the large wavenumbers. The equivalent structure function method shows abnormalities, projecting a line straight from the small wavenumbers to the large wavenumber noise floor seen of the other methods. Figure 26 shows the same as Figure 25 but we have applied a Gaussian blur at the scale represented by the dashed vertical line to the fluctuation map and computed the spectra based off that. Now, the Flat-sky and periodogram (blue and red) still agree, but the correlogram and Arevalo methods (green and purple) do not. The equivalent structure function method now closely traces the  $11/3$  power law slope.

More work is required to fully understand what is happening here; the effects of Poisson noise on the retrieved turbulence statistics for the different methods and the difference between the smoothing and the techniques for Poisson noise removal discussed in Churazov et al. (2012).

Figure 27 shows a processed SITELLE observation (Drissen et al. 2010) of the galaxy NGC1275 in the core of the Perseus cluster. The observation file was downloaded and processed using ORCS (Martin et al. 2015, 2018, 2021b,a). My results are similar to the result obtained by Gendron-Marsolais et al. (2018) (seen in Figure 3) but contains

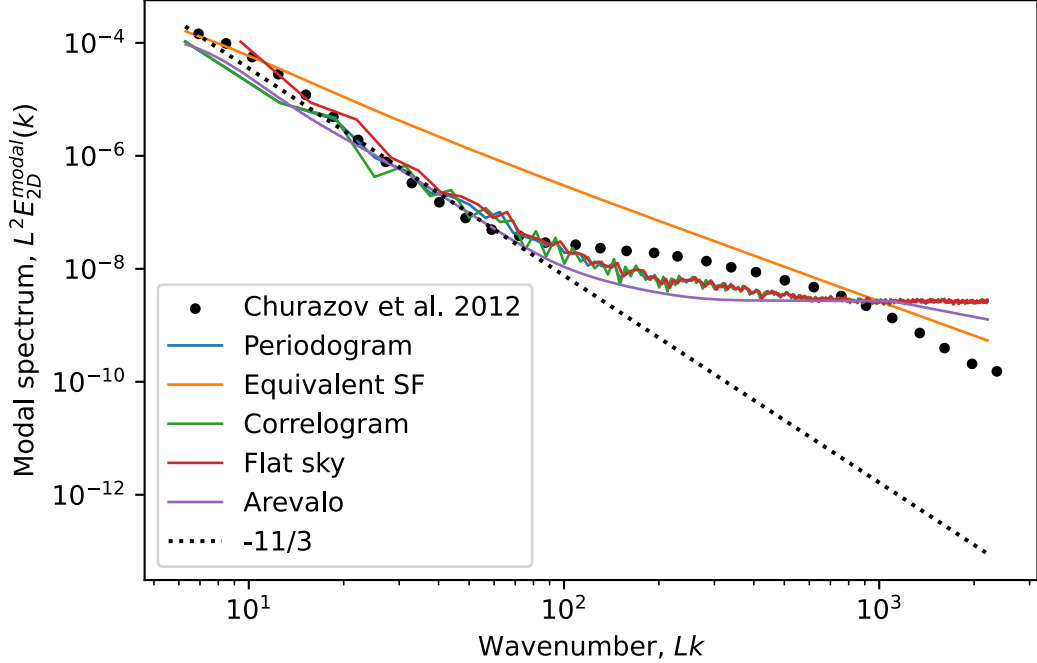


**Figure 25.** Normalized modal spectrum versus the normalized wavenumber for the different methods for computing the spectrum of the X-ray surface brightness fluctuations Figure 24. The periodogram (blue), correlogram (green), flat-sky (red), and Arevalo (purple) methods are consistent. The equivalent structure function method (orange) does not agree with the other methods however, could be due to the noise and projection bias seen in Figure 14. Black dots is the Poisson noise subtracted spectrum, extracted from Churazov et al. (2012), this spectrum was also generated in a smaller region. The dotted black line is a  $11/3$  power law for comparison.

more noise and does not seem to show as much structure in the outer filaments, meaning power spectra calculations of this image obtains incorrect results. This is still being investigated.

## 5. SUMMARY

In summary: information is lost during the 2D projection process. This results in a difference between spectra estimated using different methods, with the worst performing being the equivalent structure function method; this result applies to the simulations and generated fBM data. When noise is introduced (for now, just to the fBM data), the structure function obtains the correct slope of the projected 2D image when a Gaussian blur is applied. However, this is most likely artificial due to there realistically being no information beyond the noise scale but it is still interesting possibility to consider.

## 6. FUTURE WORK

This final section details the future work for this project. The first step is to properly quantify the differences observed in the above sections; fitting slopes to the obtained estimations to be able to properly compare them. Next, an investigation

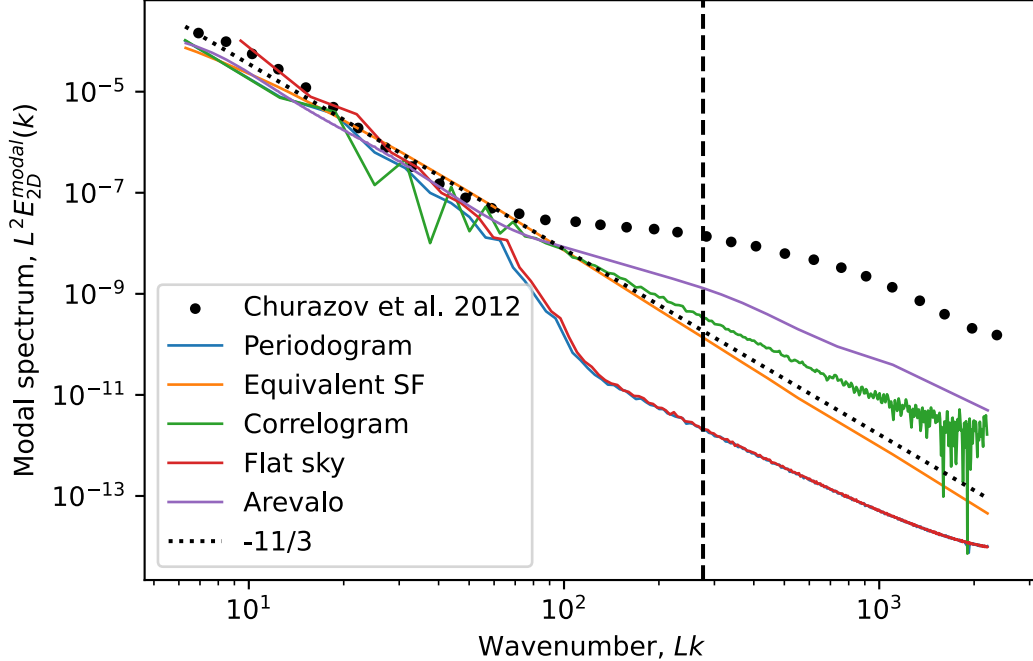


**Figure 26.** Normalized modal spectrum versus the normalized wavenumber for the different methods for computing the spectrum of the *smoothed* X-ray surface brightness fluctuations Figure 24. The periodogram (blue) and flat-sky (red) spectra are mostly equivalent. The equivalent structure function (orange) almost exactly follows the power law. The Arevalo (purple) and correlogram (green) method mostly follow the other spectra at large scales but behave differently past the smoothing scale. Black dots is the Poisson noise subtracted spectrum, extracted from Churazov et al. (2012), this spectra was also generated with a region. The dotted black line is a 11/3 power law for comparison. The dashed black vertical line shows the Gaussian smoothing scale of  $n = 16$ .

into the exposure maps and masks applied to underlying observations is required. Currently I can generate random exposure and mask maps Figure 15), so these will need to be applied to the generated fBM fields and simulation data and I will need to investigate the effects on the returned power spectra. Realistically, we will also end up generating an exposure map that more closely resembles the exposure map for the X-ray, Chandra Coma cluster observation. True observed images contain noise which can be added via sampling from a Poisson distribution where each pixel in the image is the mean of the Poisson distribution for that pixel. The final process to obtain an simulated observed image will be the following:

- A 3D simulation (or, in general, a datacube) will have a 3D mean beta distribution applied
- This datacube (with the added mean field) will be projected (with some relevant emissivity factor) along the line-of-sight to obtain a projected image which constitutes a projected mean and projected fluctuation component.
- An exposure map will be applied obtaining an exposure map corrected observed image.

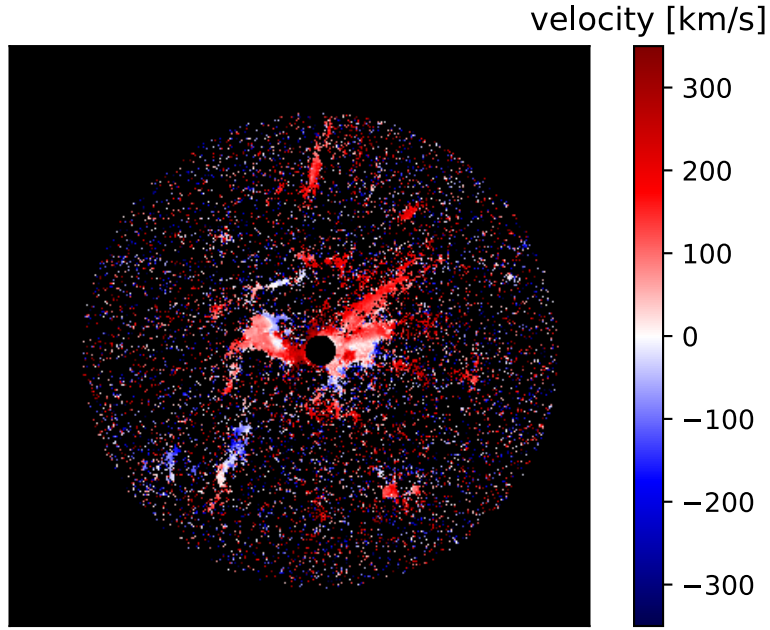


**Figure 27.** A processed SITELLE observation of the galaxy NGC1275 in the core of the Perseus cluster in the SN3 band. The velocities are obtained by fitting the SITELLE emission lines to the H $\alpha$  line to obtain the doppler shift, subtracting the mean velocity of the cluster obtains the bulk (line-of-sight) velocity fluctuations for the H $\alpha$  filaments (as shown).

- We will then be able to correctly add in Poisson noise where the exposure map corrected image is chosen as the mean of the Poisson distribution for each pixel.
- We will then be able to subtract a beta model to obtain the observed projected fluctuations (with noise).
- From here we will perform the analysis, comparing methods of retrieving the true spectra (of the 3D data cube) to the retrieved observed, projected fluctuations.

The next step will be to use the PLUTO Code for Astrophysical Gas Dynamics ([Mignone et al. \(2007, 2012\)](#)) to run my own simulations. PLUTO is a freely-distributed software for the numerical solution of astrophysical fluid dynamics, and can be used to simulate turbulence in the ICM under appropriate parameters. Currently I have been able to run the test cases provided with the code and analyze the resultant data. So, next I will implement my own initial conditions to simulate isotropic, homogeneous, compressible MHD turbulence. Lastly, this will be extended further to incorporate the stratified dynamics, this is necessary to simulate turbulence in the ICM conditions. This will enable me to calculate projections for the pressure, temperature, density, velocity and magnetic fields using the processes de-

839 scribed above. Future work will focus on the pressure and density projections with  
840 simulated mean distributions, emissivity values, noise, exposure maps and masks in  
841 order to investigate the retrieval of the 3D spectra from 2D observed ICM surface  
842 brightness fluctuation maps.

## APPENDIX

844                   A. POWER SPECTRA DERIVATIONS

845                   A.1. *Spectrum types*

846     For variables consisting of multiple dimensions *i.e.* vector fields like the velocity and  
 847     magnetic fields, the *spectral tensor* defines the tensor consisting of each combination  
 848     of directions from the vector field in Fourier space. For example, for the velocity field  
 849      $\mathbf{u}(\mathbf{x})$ , its spectral tensor is

850                   
$$S_{ij}(\mathbf{k}) = \hat{u}_i(\mathbf{k})\hat{u}_j(\mathbf{k}) \quad (\text{A1})$$

852     where the  $i, j$  subscripts are the index notation, where repeated indices implies a  
 853     summation. The *modal spectrum* is then constructed as the *trace* of the *spectral*  
 854     *tensor*. Assuming the same velocity field is a 3-dimensional vector field, the *modal*  
 855     *spectrum* is then

856                   
$$E^{\text{modal}}(\mathbf{k}) = S_{ii}(\mathbf{k}) = |\hat{u}_x(\mathbf{k})|^2 + |\hat{u}_y(\mathbf{k})|^2 + |\hat{u}_z(\mathbf{k})|^2 \quad (\text{A2})$$

858     Scalar quantities such as the density  $\rho(\mathbf{x})$  have modal spectrum defined as

859                   
$$E^{\text{modal}}(\mathbf{k}) = |\hat{\rho}(\mathbf{k})|^2 \quad (\text{A3})$$

861     For the 2D projections; say and image in the 2D sky-plane  $I(\boldsymbol{\theta})$  (integration of  
 862     a quantity along the line-of-sight  $\ell$ ) where  $\boldsymbol{\theta}$  is the 2D sky-plane vector; its *modal*  
 863     *spectrum* is a 2D spectrum of a single variable dependent on the sky-plane position  $\boldsymbol{\theta}$

864                   
$$E^{\text{modal}}(\mathbf{k}_\theta) = \left| \hat{I}(\mathbf{k}_\theta) \right|^2 \quad (\text{A4})$$

866     where  $\mathbf{k}_\theta$  is the wavenumber vector in the sky-plane  $\boldsymbol{\theta}$ .

867                   A.1.1. *Omni-directional and modal spectra*

868     The *omni-directional* and *modal spectra* are best explored through Parseval's Theorem;  
 869     (twice) the RMS configuration-space energy (variance) per unit mass (or twice  
 870     the total Fourier space energy per unit mass) is the integral of the *modal* energy  
 871     spectrum with respect to the wavenumber vector  $\mathbf{k}$

872                   
$$\langle u(\mathbf{x})^2 \rangle = 2E^{\text{total}} = \frac{1}{(2\pi)^D} \int_{-\infty}^{\infty} E^{\text{modal}}(\mathbf{k}) d^D \mathbf{k} \quad (\text{A5})$$

874     For a three-dimensional spectrum, if we convert the integral to spherical polar coordinates

876                   
$$E_{3D}^{\text{total}} = \frac{1}{(2\pi)^D} \int E_{3D}^{\text{modal}}(\mathbf{k}) d^3 \mathbf{k} \quad (\text{A6})$$

877                   
$$= \frac{1}{(2\pi)^D} \int \int \int k^2 \sin \theta E_{3D}^{\text{modal}}(k, \theta, \phi) d\theta d\phi dk \quad (\text{A7})$$

878                   
$$= \frac{1}{(2\pi)^D} \int_{k=-\infty}^{\infty} k^2 \int_{\theta=0}^{2\pi} \int_{\phi=0}^{\pi} \sin \theta E_{3D}^{\text{modal}}(k, \theta, \phi) d\theta d\phi dk \quad (\text{A8})$$

879                   
$$= \frac{1}{(2\pi)^D} \int_{k=-\infty}^{\infty} \mathcal{E}_{3D}^{\text{omni}}(k) dk \quad (\text{A9})$$

we arrive at the definition of the *omni-directional spectrum*  $\mathcal{E}_{3D}^{\text{omni}}(k)$ , this is the spectrum that integrates over wavevector directions. If the turbulence is actually isotropic, then we must have  $\mathcal{E}^{\text{omni}}(k, \theta, \phi) = \mathcal{E}^{\text{omni}}(k)$ , and the omni-directional spectrum is a simple multiple of the modal spectrum (by the surface 'area' of the constant  $k = |\mathbf{k}|$  magnitude surface). So, for two and three dimensional energy spectra, the *omni-directional spectra* are the following:

$$\mathcal{E}_{2D}^{\text{omni}}(k_2) = 2\pi k E_{2D}^{\text{modal}}(|\mathbf{k}_2|) \quad (\text{A10})$$

$$\mathcal{E}_{3D}^{\text{omni}}(k_3) = 4\pi k^2 E_{3D}^{\text{modal}}(|\mathbf{k}_3|) \quad (\text{A11})$$

where  $k_2 = |\mathbf{k}_2| = \sqrt{k_x^2 + k_y^2}$ , and  $k_3 = |\mathbf{k}_3| = \sqrt{k_x^2 + k_y^2 + k_z^2}$  are the magnitudes of their respective  $D$ -dimensional wavenumber vectors. For ease, we have written the different ways of integrating over spectra to obtain the energy:

$$E_{3D}^{\text{total}} = \frac{1}{8\pi^3} \int_{-\infty}^{\infty} E_{3D}^{\text{modal}}(\mathbf{k}_3) d^3 \mathbf{k}_3 \stackrel{\text{isotropy}}{=} \frac{1}{8\pi^3} \int_{-\infty}^{\infty} 4\pi k_3^2 E_{3D}^{\text{modal}}(|\mathbf{k}_3|) dk_3 = \frac{1}{8\pi^3} \int_{-\infty}^{\infty} \mathcal{E}_{3D}^{\text{omni}}(k_3) dk_3 \quad (\text{A12})$$

$$E_{2D}^{\text{total}} = \frac{1}{4\pi^2} \int_{-\infty}^{\infty} E_{2D}^{\text{modal}}(\mathbf{k}_2) d^2 \mathbf{k}_2 \stackrel{\text{isotropy}}{=} \frac{1}{4\pi^2} \int_{-\infty}^{\infty} 2\pi k_2 E_{2D}^{\text{modal}}(|\mathbf{k}_2|) dk_2 = \frac{1}{4\pi^2} \int_{-\infty}^{\infty} \mathcal{E}_{2D}^{\text{omni}}(k_2) dk_2 \quad (\text{A13})$$

Practically, we can calculate the *omni-directional spectra* and then divide by the shell integral (normalization) factor to get the *angle-averaged modal spectrum*; or the average value in spherical annuli/shells at magnitude  $k_2/k_3$  and size  $dk_2/dk_3$ , is the modal spectrum:

$$E_{2D}^{\text{modal}}(|\mathbf{k}_2|) = \frac{\mathcal{E}_{2D}^{\text{omni}}(k_2)}{2\pi k} \quad (\text{A14})$$

$$E_{3D}^{\text{modal}}(|\mathbf{k}_3|) = \frac{\mathcal{E}_{3D}^{\text{omni}}(k_3)}{4\pi k^2} \quad (\text{A15})$$

### A.1.2. Projected spectra

The *projection-slice theorem* states that the Fourier transform of a projection is the same as taking a slice of the original data in Fourier space. So for a projection of the 3D data along the  $z$ -axis

$$f^{\text{proj}}(x, y) = \int f(x, y, z) dz \quad (\text{A16})$$

its 2D modal spectrum is the same as the slice (of wavenumber in the projection axis)  $k_z = 0$  of the original 3D modal spectrum

$$E_{2D}^{\text{modal}}(k_x, k_y) = E_{3D}^{\text{modal}}(k_x, k_y, 0) \quad (\text{A17})$$

For a generalized projection with an emissivity factor dependent on the line-of-sight variable only

$$f^{\text{proj}}(x, y) = \int f(x, y, z) \epsilon(z) dz \quad (\text{A18})$$

then, accounting for this additional term (Peacock 1999; Zhuravleva et al. 2012; Churazov et al. 2012; Khatri & Gaspari 2016; ZuHone et al. 2016)

$$E^{\text{modal}}(k_x, k_y) = \int E^{\text{modal}}(k_x, k_y, k_z) |\hat{\epsilon}(k_z)|^2 dk_z \quad (\text{A19})$$

where

$$\hat{\epsilon}(k_z) = \int \epsilon(z) e^{ik_z z} dz \quad (\text{A20})$$

is the Fourier transform of the emissivity function, so  $E_{\text{EM}}^{\text{modal}}(k_z) = |\hat{\epsilon}(k_z)|^2$  is the one-dimensional modal spectrum of the emissivity. Churazov et al. (2012) assumes there is a wavenumber  $k_{z,\text{cutoff}}$  for which  $E_{\text{EM}}^{\text{modal}}(k_z)$  falls off for  $k_z \gg k_{z,\text{cutoff}}$ . Therefore, for  $k_z \gg k_{z,\text{cutoff}}$

$$E_{2D}^{\text{modal}}(k_x, k_y) \approx E_{3D}^{\text{modal}}(k_x, k_y, 0) \int E^{\text{modal}}(k_z) dk_z \quad (\text{A21})$$

So now, our 2D modal spectrum is the 3D modal spectrum (with the line-of-sight wavenumber  $k_z = 0$ ) with some (assumed constant in  $k$ ) scaling factor.

### A.1.3. Reduced spectrum

In some situations, we do not have enough information to calculate the total *omnidirectional* or *modal* spectrum. For example, typical *in-situ* observations of the solar wind with a single spacecraft occur along a single direction (radially  $\hat{\mathbf{R}}$  from the sun) (e.g., Oughton et al. 2015); this is a one-dimensional slice. This leads to the definition of the *reduced spectrum* (Batchelor 1953), which is the projection of the three-dimensional *modal spectrum* onto the observation direction  $\mathbf{R}$ , yielding a function of the reduced wavenumber  $k_R = \mathbf{k} \cdot \hat{\mathbf{R}}$

$$E^{\text{red}}(k_R) = \int_{-\infty}^{\infty} \int_{-\infty}^{\infty} E_{3D}^{\text{modal}}(k_1, k_2, k_R) dk_1 dk_2 \quad (\text{A22})$$

So the reduced spectrum is the integral of the modal spectrum over all but one of the  $\mathbf{k}$ -space coordinates. Because many measurements are essentially 1D slices, this quantity is heavily used in analysis of fluid mechanics experiments (e.g., wind tunnels) and solar wind measurements. It is also useful to consider *partially* reduced spectra, where, for example, only one  $\mathbf{k}$ -space coordinate is integrated over. Consider an  $R$ -dimensional slice from a  $D > R$ -dimensional *modal spectrum*,  $E^{\text{modal}}(\mathbf{k})$ , with  $\mathbf{k}$  a  $D$ -dimensional vector. We can separate the components of  $\mathbf{k}$  into the coordinates spanning the  $R$ -dimensional slice,  $\mathbf{k}'$ , and the rest,  $\mathbf{k}_{\text{red}}$ . Projecting from (i.e., integrating over) the  $R$   $\mathbf{k}'$  Cartesian coordinates yields a *partially reduced spectrum*

$$E^{\text{red}}(\mathbf{k}_{\text{red}}) = \int E^{\text{modal}}(\mathbf{k}) d^R \mathbf{k}' \quad (\text{A23})$$

In relevance to astronomical observations, the partially reduced spectrum would be the integral over one wavenumber direction (the line-of-sight wavenumber)  $k_\ell$ . This produces a *line-of-sight reduced spectrum* that is a function of the two Cartesian wavenumbers in the 2D sky-plane,  $\mathbf{k}_\theta$ :

$$E^{\text{red}}(\mathbf{k}_\theta) = \int E^{\text{modal}}(\mathbf{k}_\theta, k_\ell) dk_\ell \quad (\text{A24})$$

This is the spectrum of a 2D slice of 3D data. In essence, this is equivalent to the *projection slice theorem*; the original 3D data is the Fourier space form and the transformation is the inverse Fourier transform. Taking the projection in Fourier space and transforming via the inverse Fourier transform is the same as taking the slice of the inverse Fourier transform of the 3D Fourier space data (i.e., the configuration space 3D data).

## A.2. Spectrum methods

The energy spectrum describes how the energy is distributed across wavenumbers, which can be thought of as the reciprocal scales of the turbulent system. There are several ways to extract an energy spectrum through different definitions of scales. The first two methods: *periodogram* and *correlogram*, use Fourier transforms to decompose the random turbulent signal into constituent wavenumbers. The third method, calculates a *lag-space* and transforms it into an equivalent energy spectrum. Lastly, a scale-space method is used where Gaussian convolutions select structures on a specific scale, which is then used to construct another equivalent spectrum.

## A.3. Fourier spectra

The modal spectrum calculated using the Fourier transformation can be accomplished with the following

$$E^{\text{modal}}(\mathbf{k}) = \langle |\hat{u}(\mathbf{x})|^2 \rangle = \left\langle \left| \int u(\mathbf{x}) e^{-i\mathbf{k}\cdot\mathbf{x}} d^D \mathbf{x} \right|^2 \right\rangle \quad (\text{A25})$$

The DFT implementation of this formulation is called the *periodogram*. An equivalent method for calculating the modal spectrum is via the Fourier transform of the autocorrelation function (*Wienver-Khinchin theorem*)

$$E^{\text{modal}}(\mathbf{k}) = \int R(\mathbf{r}) e^{-i\mathbf{k}\cdot\mathbf{r}} d^D \mathbf{r} \quad (\text{A26})$$

where  $R(\mathbf{r}) = \langle u(\mathbf{x})u(\mathbf{x} + \mathbf{r}) \rangle$  is the autocorrelation function. The discrete form of this method is called the *correlogram*. Using the inverse Fourier transform

$$R(\mathbf{r}) = \frac{1}{(2\pi)^D} \int E^{\text{modal}}(\mathbf{k}) e^{i\mathbf{k}\cdot\mathbf{r}} d^D \mathbf{k} \quad (\text{A27})$$

If we take the integrals over spherical polar coordinates with  $J_0(kr) = \sin(kr)/kr$  being the spherical Bessel function of the first kind of order zero (Frisch 1995; Pope 2000; Davidson & Nelkin 2005)

$$\Rightarrow R(r) = \frac{1}{(2\pi)^D} \int_{-\infty}^{\infty} \mathcal{E}^{\text{omni}}(k) J_0(kr) dk \quad (\text{A28})$$

### A.3.1. Equivalent structure function

Energies of eddies of size  $\lambda$  or less this association doesn't capture all of the contribution (there is an additional term of  $\lambda^2$  times the enstrophy of the eddies)

Using the binned second order structure function  $S_2(\lambda)$ , where  $\lambda = |\boldsymbol{\lambda}|$ , we can approximate the *equivalent omni-directional spectrum* in the inertial (power-law) range by first expanding the definition for the structure function

$$S_2(\boldsymbol{\lambda}) = \langle |u(\mathbf{x}) - u(\mathbf{x} + \boldsymbol{\lambda})|^2 \rangle \quad (\text{A29})$$

$$= \langle |u(\mathbf{x})|^2 \rangle - 2 \langle u(\mathbf{x}) u(\mathbf{x} + \boldsymbol{\lambda}) \rangle + \langle |u(\mathbf{x} + \boldsymbol{\lambda})|^2 \rangle \quad (\text{A30})$$

$$= 2 \langle |u(\mathbf{x})|^2 \rangle - 2 \langle u(\mathbf{x}) u(\mathbf{x} + \boldsymbol{\lambda}) \rangle \quad (\text{A31})$$

$$= 2R(0) - 2R(\boldsymbol{\lambda}) \quad (\text{A32})$$

where we have used the fact that  $u(x)$  is homogeneous (*i.e.*  $\langle u(x) \rangle = \langle u(x + \lambda) \rangle$ ).

$$S_2(\boldsymbol{\lambda}) = \frac{2}{(2\pi)^D} \int_{-\infty}^{\infty} E^{\text{modal}}(\mathbf{k}) d\mathbf{k} - \frac{2}{(2\pi)^D} \int_{-\infty}^{\infty} e^{i\mathbf{k}\cdot\boldsymbol{\lambda}} E^{\text{modal}}(\mathbf{k}) d^D \mathbf{k} \quad (\text{A33})$$

$$= \frac{2}{(2\pi)^D} \int_{-\infty}^{\infty} [1 - e^{i\mathbf{k}\cdot\boldsymbol{\lambda}}] E^{\text{modal}}(\mathbf{k}) d^D \mathbf{k} \quad (\text{A34})$$

$$\Rightarrow S_2(\lambda) = \frac{2}{(2\pi)^D} \int_{-\infty}^{\infty} (1 - J_0(k\lambda)) \mathcal{E}^{\text{omni}}(k) dk \quad (\text{A35})$$

where we have taken the integration in (spherical) polar coordinates and where  $J_0$  is a spherical Bessel function of the first kind of order zero; this relation holds for 2 and 3 dimensional data.  $1 - J_0(k\lambda)$  acts as a filter on the omni-directional spectrum to extract the structure function. Assuming large separations, the filter is

$$\lim_{k\lambda \gg 1} [1 - J_0(k\lambda)] = 1 \quad (\text{A36})$$

and assuming  $k$  is in the inertial range (*i.e.*  $\mathcal{E}^{\text{omni}}(k) \propto k^{-\beta}$ ; for Kolmogorov scaling  $\beta = 5/3$ )

$$S_2(\lambda) \approx \frac{2}{(2\pi)^D} \int \mathcal{E}^{\text{omni}}(k) dk \quad (\text{A37})$$

$$\propto \frac{2}{(2\pi)^D} \int k^{-\beta} dk \quad (\text{A38})$$

$$\approx \frac{2}{(2\pi)^D} k^{-\beta+1} \quad (\text{A39})$$

$$= \frac{2}{(2\pi)^D} k \mathcal{E}^{\text{omni}}(k) \quad (\text{A40})$$

1022 Rearranging the above, we can obtain the *omni-directional spectrum* via the second  
 1023 order structure function assuming  $k \propto 1/\lambda$

$$\stackrel{1024}{\Rightarrow} \mathcal{E}^{\text{SF}}(k) \propto \lambda S_2(\lambda) \quad (\text{A41})$$

1026 This obtains the expected result for Kolmogorov scaling ( $\alpha = -5/3$ ), then  $S_2(\lambda) \propto$   
 1027  $\lambda^{2/3}$ . This method is also expressed in the following literature: [Tennekes & Lumley \(1972\)](#);  
 1028 [Frisch \(1995\)](#); [Stutzki et al. \(1998\)](#); [Pope \(2000\)](#); [Davidson & Nelkin \(2005\)](#);  
 1029 [Chhiber et al. \(2018\)](#). This method isn't exactly true, the general shape for the (three-  
 1030 dimensional) *longitudinal second order structure function*  $S_2(\lambda_{\parallel})$  for *homogeneous,*  
 1031 *isotropic turbulence*

$$\stackrel{1032}{S}_2(\lambda_{\parallel}) = \frac{4}{3} \int_0^{\infty} \mathcal{E}^{\text{omni}}(k) H(k\lambda) dk \quad (\text{A42})$$

1033 where, the filter is now

$$\stackrel{1035}{H}(k\lambda) = 1 + \frac{3 \cos(k\lambda)}{(k\lambda)^2} - \frac{3 \sin(k\lambda)}{(k\lambda)^3} \quad (\text{A43})$$

1037 Approximating this function as

$$\stackrel{1038}{H}(k\lambda) \approx \hat{H}(k\lambda) = \begin{cases} \left(\frac{k\lambda}{\pi}\right)^2 & k\lambda < \pi \\ 1 & k\lambda > \pi \end{cases} \quad (\text{A44})$$

1040 which obtains the following approximation

$$\stackrel{1041}{\frac{3}{4} S_2(\lambda_{\parallel})} \approx \int_{\pi/\lambda}^{\infty} \mathcal{E}^{\text{omni}}(k) dk + \frac{\lambda^2}{\pi^2} \int_0^{\pi/\lambda} k^2 \mathcal{E}^{\text{omni}}(k) dk \quad (\text{A45})$$

1043 So the *longitudinal second order structure function* is the sum of all eddies of size  $\lambda$   
 1044 or less and the enstrophy in eddies of size  $\lambda$  or greater ([Batchelor 1953](#); [Pope 2000](#)).  
 1045 If we ignore the contribution from the enstrophy, then we can easily obtain a similar  
 1046 expression to the one derived above. This definition requires the incompressibility  $\nabla \cdot \mathbf{u} = 0$ , so this relation might now perform well for the compressible MHD turbulence.

### 1048 A.3.2. Arevalo method

1049 This section describes the Arevalo method ([Arévalo et al. 2012](#)) which has been  
 1050 developed from a technique used for examining the power spectrum in the interstellar  
 1051 medium ([Arévalo et al. 2012](#); [Stutzki et al. 1998](#); [Bensch et al. 2001](#); [Mac Low & Ossenkopf 2000](#)). A Gaussian convolution selects scales at (approximately) the standard  
 1052 deviation  $\sigma$  and larger. The aim of this method is to compute an equivalent power  
 1053 spectrum by selecting scales from the image using Gaussian convolutions where  $*$   
 1054 represents the convolution product between two functions  $f(x)$  and  $g(x)$

$$\stackrel{1056}{(f * g)(x)} = \int f(y)g(x-y) dy \quad (\text{A46})$$

1058 A Gaussian function  $g(x)$  with standard deviation  $\sigma$ , and its Fourier transform  $\hat{g}(k)$   
 1059 (that is also a Gaussian of deviation  $\sigma_k = 1/\sigma$ )

$$1060 \quad g(x) = \frac{1}{(2\pi\sigma^2)^{D/2}} e^{-x^2/2\sigma^2} \quad (\text{A47})$$

$$1061 \quad \hat{g}(k) = e^{-k^2\sigma^2/2} \quad (\text{A48})$$

1063 By defining standard deviations of slight difference, determined by  $\xi$  where  $\xi \ll 1$

$$1064 \quad \sigma_1 = \sigma / \sqrt{1 + \xi} \quad (\text{A49})$$

$$1065 \quad \sigma_2 = \sigma \sqrt{1 + \xi} \quad (\text{A50})$$

1067 and taking their difference, we form our filter  $\hat{f}(k) = \hat{g}_1(k) - \hat{g}_2(k)$  in Fourier space

$$1068 \quad \hat{f}(k) = \hat{g}_1(k) - \hat{g}_2(k) \approx k^2\sigma^2\xi e^{-k^2\sigma^2/2} \quad (\text{A51})$$

1070 where we have taken Taylor expansion approximations about  $\xi$

$$1071 \quad \hat{g}_1(k) = e^{-k^2\sigma_1^2/2} = e^{-k^2\sigma^2/2(1+\xi)} \approx e^{-k^2\sigma^2/2} \left(1 + \frac{1}{2}k^2\sigma^2\xi\right) \quad (\text{A52})$$

$$1072 \quad \hat{g}_2(k) = e^{-k^2\sigma_2^2/2} = e^{-k^2\sigma^2(1+\xi)/2} \approx e^{-k^2\sigma^2/2} \left(1 - \frac{1}{2}k^2\sigma^2\xi\right) \quad (\text{A53})$$

1074 This filter selects scales  $\sigma_1$  and  $\sigma_2$  and takes their differences, which results in  
 1075 subtracting scales of size  $\sigma_2$  and larger from scales of size  $\sigma_1$  resulting in scales of  
 1076 exactly  $\sigma$ , assuming  $\xi$  is small.

1077 The filter  $\hat{f}(k)$  has a maximum value at

$$1078 \quad \frac{d\hat{f}}{dk} = 0 \implies \frac{k^2\sigma^2}{2} = 1 \implies k_{max} = \frac{\sqrt{2}}{\sigma} \quad (\text{A54})$$

1080 If we let  $k = 2\pi k'$ , we obtain the result from Arévalo et al. (2012):  $k' = \frac{1}{\sqrt{2\pi^2}} \frac{1}{\sigma}$ .

1081 Rewriting the filter in terms of  $k_{max}$

$$1082 \quad \hat{f}_{max}(k) = 2 \left( \frac{k}{k_{max}} \right)^2 \xi e^{-(k/k_{max})^2} \quad (\text{A55})$$

1084 Finally, convolving the filter with our  $D$ -dimensional image  $u(x)$ , we find the vari-  
 1085 ance as

$$1086 \quad V = \int |(u * f)(x)|^2 dx \quad (\text{A56})$$

$$1087 \quad = \frac{1}{2\pi} \int |\hat{u}(k)\hat{f}(k)|^2 dk \quad (\text{A57})$$

$$1088 \quad = \frac{1}{2\pi} \int |\hat{u}(k)|^2 |\hat{f}(k)|^2 dk \quad (\text{A58})$$

$$1089 \quad = \frac{1}{2\pi} |\hat{u}(k_{max})|^2 \int |\hat{f}(k)|^2 dk \quad (\text{A59})$$

In the second step, we have converted the real-space convolution to Fourier space using Parseval's theorem and the convolution identity that results in the product in Fourier space. In the last step, we have assumed that  $|\hat{u}(k)|^2$  is dependent on  $k_{max}$  and not  $k$ , allowing us to remove it from the integral. In other words,  $\hat{f}(k)$  selects scales dominantly at  $k = k_{max}$  from  $\hat{u}(k)$ . By rearranging the above equation, we obtain the *modal spectrum* value at an equivalent wavenumber  $k_{max}$

$$\implies E^{\text{Arevalo}}(k_{max}) = \frac{1}{2\pi} |\hat{u}(k_{max})|^2 = \frac{\int |(u * f)(x)|^2 dx}{\int |\hat{f}(k)|^2 dk} \quad (\text{A60})$$

To calculate the complete *modal spectrum*, this step is repeated across a range of  $\sigma$  values, corresponding to equivalent wavenumber ( $k_{max}$ ) values, to give the entire spectrum.

The purpose of the Arevalo method is to cope with the removal of data in astronomical observations. The above method is modified to include a mask/exposure map  $\Xi$ , that defines pixels in the image as masked out or weights points based on their exposure (Arévalo et al. 2012). Now, the variance is

$$V = \Xi(x) \left( f * \frac{u}{\Xi} \right)(x) = \Xi(x) \left( \frac{(g_1 * u)(x) - (g_2 * u)(x)}{(g_1 * \Xi)(x) - (g_2 * \Xi)(x)} \right) \quad (\text{A61})$$

The rest of the method is the same.

### A.3.3. Spherical harmonics: flat-sky approximation

A projected galaxy cluster described as an observation on the total sky-sphere. If we describe our cluster turbulent projection in the region on the sky-sphere, and decomposing as a spherical harmonic (with associated Legendre polynomials), and assuming the angular distance is small, the *flat-sky approximation* can be achieved Peacock (1999); Jaffe & Kamionkowski (1998); Khatri & Gaspari (2016); Alonso et al. (2019). In essence, this assumes if our angular distances are small, the observation can be assumed to be a (projected sky-) plane in the projected sky-sphere. Therefore, the *flat-sky approximation* provides a method for estimating power spectra from a spherical harmonic decomposition.

## B. POWER SPECTRA IN LITERATURE

There is a lot of ambiguity in the literature definitions of the power spectrum. Different papers use different definitions of the power spectrum (or don't specify it at all) and use different normalizations (namely, regarding where the  $2\pi$  factors belong; both in the wavenumber and the Fourier transform). Since we are looking at comparing different methods, it is important to keep track of the  $2\pi$  factors and any others that appear in equivalent forms of the power spectrum. This section is intended to highlight, for clarity, some differences in definitions and terms used across different fields.

### B.1. Signal Processing

It is common in signal processing to define the *energy spectrum*

$$E(f) = |\hat{x}(f)|^2 \quad (\text{B62})$$

from the one-dimensional Fourier transform

$$\hat{x}(f) = \int_{-\infty}^{-\infty} x(t)e^{-2\pi ift} dt \quad (\text{B63})$$

of a one-dimensional time-series signal  $x(t)$  with *finite energy*

$$E = \int_{-\infty}^{\infty} |x(t)|^2 dt < \infty \quad (\text{B64})$$

It is acknowledged that future variation of a signal cannot be known exactly, so probabilistic statements have to be made. The signal  $x(t)$  becomes a random signal (a stationary stochastic process) extending throughout all time, which, would give infinite energy or another stochastic process with a single observation (one realization of the signal) depending on if we treat the observation as a discrete or continuous signal. If we observe the random signal  $x(t)$  over a finite time interval  $[-T/2, T/2]$  giving  $x_T(t)$ , its Fourier transform is

$$\hat{x}_T(f) = \int_{-\infty}^{\infty} x_T(t)e^{-2\pi ift} dt = \int_{-T/2}^{T/2} x(t)e^{-2\pi ift} dt \quad (\text{B65})$$

and the *energy spectrum* is now

$$E(f) = \langle |\hat{x}_T(f)|^2 \rangle \quad (\text{B66})$$

where  $\langle \cdot \rangle$  is the expectation over realizations. For convergence as  $T \rightarrow \infty$  the *power spectrum* is

$$S(f) = \lim_{T \rightarrow \infty} T^{-1} E(f) \quad (\text{B67})$$

$$= \lim_{T \rightarrow \infty} \left\langle \frac{1}{T} \left| \int_{-T/2}^{T/2} x(t)e^{-2\pi ift} dt \right|^2 \right\rangle \quad (\text{B68})$$

which has the advantage of being real, non-negative and existing for all stationary processes with zero mean and finite variance (Schuster 1898; Blackman et al. 1960; Oppenheim et al. 1999; Stoica & Moses 2005; Barbour & Parker 2022).

1158      **B.2. Energy and power spectrum in astronomy literature**

1159      It is common in astronomical literature (Brandenburg & Lazarian 2013; Brunt et al.  
 1160      2003; ZuHone et al. 2016) to define the  $D$ -dimensional *power spectrum*  $P_D(k)$  as  
 1161      the equivalent of the (more commonly represented in turbulence literature) *modal*  
 1162      *spectrum*  $E_D^{\text{modal}}(|\mathbf{k}|)$

$$1163 \quad P_D(k) \equiv E_D^{\text{modal}}(|\mathbf{k}|) \quad (B69)$$

1165      and the  $D$ -dimensional *energy spectrum*  $E_D(k)$  as the integration of shells/annuli in  
 1166      Fourier space *i.e.* what we have called the *omni-directional spectrum*  $\mathcal{E}_D^{\text{omni}}(k)$

$$1167 \quad E_D(k) = \int d\Omega P_D(k) \quad (B70)$$

$$1168 \quad \equiv \mathcal{E}^{\text{omni}}(k) \quad (B71)$$

1170      where  $d\Omega \propto k^2$  in 3D and  $\propto k$  in 2D.

1171      **B.3. Amplitudes**

1172      Expressing the *modal/power* spectrum in dimensionless form, as the *variance* per  
 1173       $\ln k$  (Peacock 1999)

$$1174 \quad \Delta_{3D}^2(k) = \frac{d \langle v^2 \rangle}{d \ln k} \quad (B72)$$

$$1175 \quad = \frac{d}{d \ln k} \int E_{3D}^{\text{modal}}(\mathbf{k}) d^3 \mathbf{k} \quad (B73)$$

$$1176 \quad = \frac{d}{d \ln k} 4\pi \int k^2 E_{3D}^{\text{modal}}(|\mathbf{k}|) dk \quad (B74)$$

$$1177 \quad = k (4\pi k^2 E_{3D}^{\text{modal}}(|\mathbf{k}|)) \quad (B75)$$

$$1178 \quad = k \mathcal{E}_{3D}^{\text{omni}}(k) \quad (B76)$$

1180      has the meaning that when  $\Delta^2(k) = 1$ , there are order-unity fluctuations from modes  
 1181      within the logarithmic bin around wavenumber  $k$ . By taking the square root of  $\Delta^2(k)$   
 1182      the standard deviation *i.e.* the amplitudes are obtained:

$$1183 \quad A_{2D}(k) = \sqrt{2\pi k^2 E_{2D}^{\text{modal}}(|\mathbf{k}|)} = \sqrt{\mathcal{E}_{2D}^{\text{omni}}(k) k} = \sqrt{\Delta_{2D}^2(k)} \quad (B77)$$

$$1184 \quad A_{3D}(k) = \sqrt{4\pi k^3 E_{3D}^{\text{modal}}(|\mathbf{k}|)} = \sqrt{\mathcal{E}_{3D}^{\text{omni}}(k) k} = \sqrt{\Delta_{3D}^2(k)} \quad (B78)$$

1186      which is the form commonly expressed in Churazov et al. (2012); Gaspari & Churazov  
 1187      (2013); Gaspari et al. (2014); Zhuravleva et al. (2012, 2019, 2014a); Khatri & Gaspari  
 1188      (2016). It is worth acknowledging that  $\Delta^2(k) = k \mathcal{E}^{\text{omni}}(k)$  has the same form as our  
 1189      second order structure function approximation  $\Delta^2(k) \approx S_2(\lambda)$ .

1190                          *B.4. Fourier convention*

1191     As described in Khatri & Gaspari (2016), X-ray studies (Churazov et al. 2012;  
 1192     Gaspari & Churazov 2013; Gaspari et al. 2014; Zhuravleva et al. 2012, 2019, 2014a)  
 1193     have typically used the Fourier convention of

$$1194 \quad f(\mathbf{x}) = \int \hat{f}(\mathbf{q}) e^{2\pi i \mathbf{q} \cdot \mathbf{x}} d^D \mathbf{q} \quad (B79)$$

1196     where  $\mathbf{k} = 2\pi \mathbf{q}$  *i.e.* the wavenumber  $\mathbf{q}$  is without the  $2\pi$  factor instead of

$$1197 \quad f(\mathbf{x}) = \frac{1}{(2\pi)^D} \int f(\mathbf{k}) e^{i \mathbf{k} \cdot \mathbf{x}} d\mathbf{k} \quad (B80)$$

1199     Following this, the amplitude spectra definitions are

$$1200 \quad A(k) = A(q) = \sqrt{2\pi q^2 P_q(q)} = \sqrt{\frac{k^2}{2\pi} P_k(k)} = \sqrt{2\pi k^2 E_{2D}^{\text{modal}}(|\mathbf{k}|)} \quad (B81)$$

1202     where  $A(k)$ ,  $A(q)$  are the amplitude are the amplitude spectra for the angular  
 1203     wavenumber (with the  $2\pi$ ) and wavenumber (without  $2\pi$ ) respectively. From this  
 1204     definition, the power/modal spectra described in the literature are the same  $P_q(q) =$   
 1205      $P_k(k)$  with different normalizations based on the  $\frac{1}{(2\pi)^D}$  factor. An additional piece of  
 1206     normalization lies in our discrete definition for the power (modal) spectra,

$$1207 \quad E^{\text{modal}}[\mathbf{m}] = \left( \frac{\Delta k}{2\pi} \right)^D \left| \hat{f}[\mathbf{m}] \right|^2 = \frac{1}{L^D} \left| \hat{f}[\mathbf{m}] \right|^2 \quad (B82)$$

1209     which has been defined this way to satisfy Parseval's theorem. So now,

$$1210 \quad P_q(\mathbf{q}) = P_k(\mathbf{k}) = \left( \frac{2\pi}{\Delta k} \right)^D E_D^{\text{modal}}[\mathbf{m}] \quad (B83)$$

1212     These definitions extend to 3D aswell and they are all consistent.

1213                          *B.5. Other packages*

1214     There are, of course, other packages exist that calculate a power spec-  
 1215     trum. For example, `scipy` has an implementation of the *periodogram*  
 1216     (`scipy.signal.periodogram()`) (Virtanen et al. 2020) however, it natively only  
 1217     works for one dimensional signals (although it is possible to calculate the *periodogram*  
 1218     of  $D$ -dimensional signals by using the orthogonality of the Fourier transform with  
 1219     some additional tinkering). The method includes an argument named `scaling` that  
 1220     is either *density* or *spectrum* which provides the distinction between the *power spec-*  
 1221     *trum* ( $PS$ ) and the *power spectral density* ( $PSD$ ) as the following

$$1222 \quad PS = \frac{E}{T} = \frac{1}{N^2} |\hat{u}(k)|^2 \quad (B84)$$

$$1223 \quad PSD = \frac{1}{\Delta k} PS = \frac{1}{N \Delta t} |\hat{u}(k)|^2 \quad (B85)$$

1225 There, the *power spectrum* has units of *units*<sup>2</sup> and corresponds to the energy of the  
 1226 signal divided by the duration. The *power spectral density* corresponds to dividing  
 1227 the power spectrum by the frequency of the bin ( $\Delta k$ ) and has units of *units*<sup>2</sup>/*Hz*.

1228 An additional normalization factor to take into account is the *single* or *double sided*  
 1229 spectral densities. This is the difference between taking the integral from  $-\infty \rightarrow \infty$   
 1230 (for *energy*) or  $-T/2 \rightarrow T/2$  (for *power*) versus  $0 \rightarrow \infty$  (or  $0 \rightarrow T/2$ ). For real-valued  
 1231 functions  $x(t)$ , the spectral densities are even and so the difference in the integral  
 1232 limits is only a factor of 2. Barbour & Parker (2022) finds a total of six different  
 1233 R packages that provide spectrum estimates, with single, double or optional/various  
 1234 normalization options available. In our case, it would be natural to use the single-  
 1235 sided spectral density with factor of two (integrating the symmetric power spectrum  
 1236 from  $0 \rightarrow \infty$ ). Moving the factor of 2 to the other side leads to the definition of an  
 1237 energy per unit mass (*e.g.*  $1/2 \langle v^2 \rangle$  for the kinetic energy).

1238 Another python package available is **turbustat** (Koch et al. 2017), it provides many  
 1239 different methods to examine the turbulent statistics, that was primarily developed  
 1240 for interstellar turbulence (Boyden et al. 2016, 2018; Koch et al. 2017; Sato et al. 2019;  
 1241 Feddersen et al. 2019). The disadvantage of **turbustat** is that their calculations of  
 1242 the statistics are strictly defined and build primarily for the observations of interstellar  
 1243 medium *i.e.* two-dimensional observations, which is not suited for my purposes. A  
 1244 lot of the inspiration for my own code (Appendix C) was derived from **turbustat**  
 1245 methods.

## 1246 B.6. Arevalo methods

1247 The following papers use different normalizations for the Arevalo method. Arevalo  
 1248 expresses their method as

$$1249 E(k_{max}) = \frac{V_{k_{max},obs}}{\xi^2 \gamma(n) k_{max}^D} \quad (B86)$$

1251 where

$$1252 V_{k_{max},obs} = \frac{N}{N_{M=1}} \int S_{k_{max}}^2(x) dx \quad (B87)$$

1254 and

$$1255 S_{k_{max}}(x) = M \left( \frac{g_1 * I}{g_1 * M} - \frac{g_2 * I}{g_2 * M} \right) \quad (B88)$$

1257 Where the normalizations  $N = \int dx$  and  $N_{M=1} = \int N(x)dx$ . The term  $\xi^2 \gamma(D) k_{max}^D$   
 1258 is the analytical solution to  $\int |\hat{f}(k)|^2 dk$ , which depends on the number of dimen-  
 1259 sions (covered by the function  $\gamma(D) = \frac{3}{4}\sqrt{\pi/2}, \pi, \frac{15\pi^{3/2}}{8\sqrt{2}}$  for  $D = 1, 2, 3$  respectively).  
 1260 Additionally, they adopt the wavenumber relation such that there is no  $2\pi$  factor  
 1261 ( $k_{max} = \frac{1}{\sigma}$ ).

1262 Churazov et al. (2012) uses the Arevalo method as

$$1263 \quad E(k_{max}) = \frac{1}{\xi^2 \gamma(n) k_{max}^D} \frac{\sum I_\sigma^2}{\sum \Xi^2} \quad (B89)$$

1264

1265 where  $E(x)$  is the exposure map for their X-ray obervations and

$$1266 \quad I_\sigma = \Xi \left( \frac{g_1 * I_{raw}}{g_1 * \Xi} - \frac{g_2 * I_{raw}}{g_2 * \Xi} \right) \quad (B90)$$

1267

1268 Similarly, albeit slightly different, Zhou et al. (2022) define their renormalized sur-  
1269 face brightness power spectral density as

$$1270 \quad E_2(k_{max}) = \frac{1}{ST} E(k_{max}) \quad (B91)$$

1271

1272 where  $S$  is the solid angle of the sky selected by the mask  $M$ , and  $T$  is the exposure  
1273 time.  $E(k_{max})$  is calculated the same as the Arévalo et al. method

$$1274 \quad E(k_{max}) = \frac{V_{k_{max}, obs}}{\xi^2 \gamma(n) k_{max}^D} \quad (B92)$$

1275

1276 The key differences here, is Churazov et al. (2012) misses the  $\frac{N}{N_{M=1}}$  normalization  
1277 factor in favour of normalizing with respect to the variance of the exposure map  
1278 (which essentially includes the  $\frac{1}{N_{M=1}}$  normalization, but misses  $N$ ). And Zhou et al.  
1279 (2022) includes everything, and applies an additional normalization for the telescope  
1280 (Suzaku) surface brightness.

### C. IMPLEMENTATION DETAILS

This section describes the implementation of the mentioned turbulence statistics and relevant methods for the project, it is intended to be released to a public repository sometime this year. This package is henceforth called the **AnalysisEngine**.

### C.1. Fractional Brownian Motion field

We generate  $D$ -dimensional Fractional Brownian motion (fBM) fields that have a specific modal spectrum power law of  $\alpha$ . This can be done from Fourier space, and translated into  $\mathbf{x}$ -space using the FFT like the following

$$\hat{f}(\mathbf{k}) = \left\{ A \left( \frac{k}{k_b} \right)^{-\alpha_1} \left[ \frac{1}{2} \left( 1 + \left( \frac{k}{k_b} \right) \right)^{1/\Delta} \right]^{\Delta(\alpha_1 - \alpha_2)} \right\}^{1/2} (\cos \theta + i \sin \theta) \quad (\text{C93})$$

$$f(\mathbf{x}) = \mathcal{F}^{-1} \left\{ \hat{f}(\mathbf{k}) \right\} \quad (\text{C94})$$

where  $\theta$  is a randomly generated number between 0 and  $2\pi$  and  $\mathcal{F}^{-1}$  is the inverse Fourier transform. This generates a broken power law function where  $\alpha_1, \alpha_2$  are the power laws (*i.e.*  $k^\alpha$ ) for  $k < k_b$  and  $k > k_b$  respectively ( $k_b$  is the break scale). The smoothing factor  $\Delta$  acts to smooth the transition between the different power law regions, but it is best left at  $\Delta = 1$ . The parameter  $A$  controls the amplitude of the spectrum. Generating  $\mathbf{k}$  and  $\theta$  as  $D$ -dimensional data with  $N$  points in each dimension provides the  $D$ -dimensional fBM field  $f(\mathbf{x})$ . Setting  $\alpha_1 = \alpha_2$  obtains a pure power law spectrum.

It is important to note, that these fields are **not** turbulent, they are missing key features, like intermittency and so will be used solely for testing purposes as we know exactly what power law we expect and they are quick to generate. However, fBM fields can be modified to more accurately represent turbulence characteristics (Miville-Deschénes et al. 2003; Esquivel et al. 2003; Ossenkopf et al. 2006a; Chepurnov & Lazarian 2009; Roman-Duval et al. 2011; Ossenkopf et al. 2006b; Brunt & Heyer 2002; Subedi et al. 2014).

### C.2. Dephasing/Gaussianizing data

Projected images have the ability to lose important phase information, essentially meaning the projection of a turbulent simulation may be just a fBM/Gaussian field. Therefore, it may be useful to examine the properties of turbulence statistics under a similar loss of phase information, this process is called: dephasing or Gaussianization. We convert our signal into Fourier space, retain the modulus component and randomly generate phases (randomly generate  $\theta$ 's and multiply the modulus component with  $\cos \theta + i \sin \theta$ ). Taking the inverse FFT returns our dephased data.

### C.3. Resolution reduction

Observations of the ICM have restraints on the resolution. If we wish to modify the resolution of a simulation or image, we can ap-

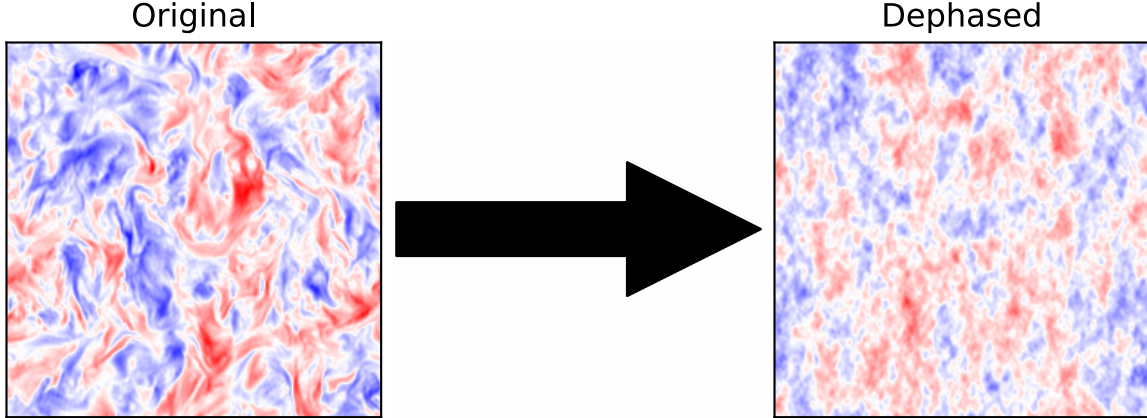


**Figure 28.** Left, the original 2D slice of a simulation. On the right, the left image has had the dephasing/Gaussianization process applied, so the complex phase information has been randomized.

ply a Gaussian blur or a pooling technique. The resolution modification is available in `analysis_engine.simulator.modify_resolution` where we use `skimage.measure.block_reduce()` and `skimage.transform.resize()` ([van der Walt et al. 2014](#)) to apply pooling, and `skimage.filters.gaussian()` to apply a Gaussian blur.

[Figure 29](#) shows a true 2D fBM field (left), and two images with different mean pooling bins (of  $n \times n$  groups of pixels). The mean pooling selects the average value from each bin of  $n \times n$  pixels, this has the affect of removing smaller scale structures and replacing them with the average structure in those bins. [Figure 30](#) shows the 2D modal power spectra calculated on the true (solid black) and pooled images (dashed and dotted grey). The pooled images largely follow the true 3D power spectrum until the Nyquist frequency is reached, showing that this method reduces the resolution but keeps the large scale structures in the modal spectrum and the small ones have been removed entirely.

[Figure 31](#) shows the Gaussian method, removing features smaller than the standard deviation (of the Gaussian,  $\sigma$ ). We show the same true 2D fBM field (left) with the Gaussian blurred fields of  $\sigma = 2$  (middle), and  $\sigma = 4$  (right). [Figure 32](#) shows their 2D modal spectra, unsurprisingly, the larger blurring (dashed gray,  $\sigma = 4$ ) drops in energy before the smaller blurring (dotted grey,  $\sigma = 2$ ) because the Gaussian blurring with a larger standard deviation will remove larger structures, therefore, lower energy at larger wavenumbers.

#### 1339 C.4. Mean field

1340 from an isotropic, homogeneous simulation with no mean field. We can assume a  
1341 Reynold's averaging, where

$$1342 \quad V(\mathbf{x}) = U(\mathbf{x}) + u(\mathbf{x}) \quad (C95)$$

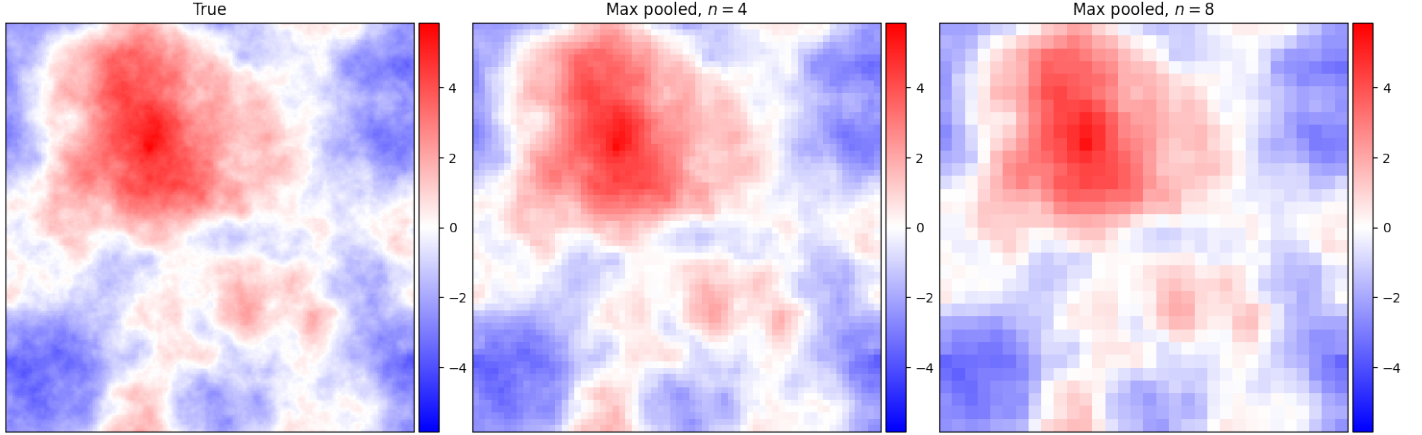


**Figure 29.** 2D fBM field (left) with the same field calculated with a max pooling resolution reduction algorithm where the maximum pixel value in groups of  $n \times n$  pixels are selected (middle  $n = 4$ , right  $n = 8$ ).

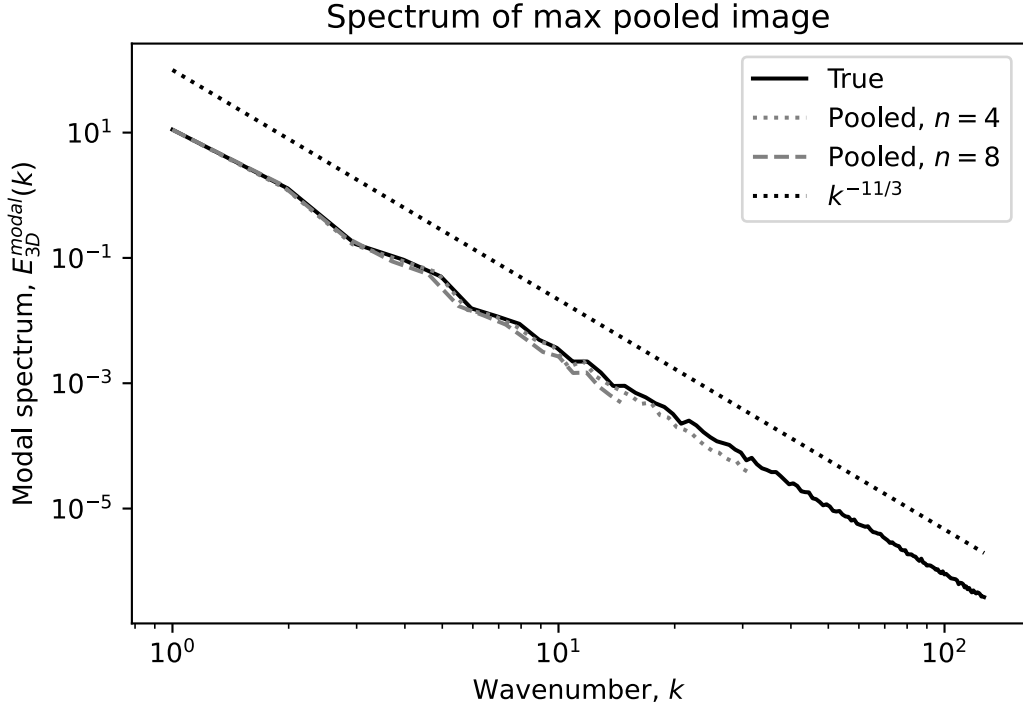


**Figure 30.** 2D modal power spectra calculated from Figure 29. The true image is displayed in solid black matching the expected power law of  $k^{-11/3}$  (dotted, black). The two pooled resolutions are in gray where dotted is for  $n = 4$  and dashed is for  $n = 8$ .

1344 where  $U(\mathbf{x}) = \langle V(\mathbf{x}) \rangle$ ,  $\langle u(\mathbf{x}) \rangle = 0$  and generate the mean field  $U(\mathbf{x})$  as a spherically  
 1345 symmetric model. To better mimic the ICM conditions, we choose to generate a  
 1346 spherical beta model (Arnaud 2009)

$$1347 \quad \bar{y}(r) = \frac{y_0}{\left(1 + \frac{r}{R_c}\right)^{3\beta/2}} \quad (C96)$$

1348

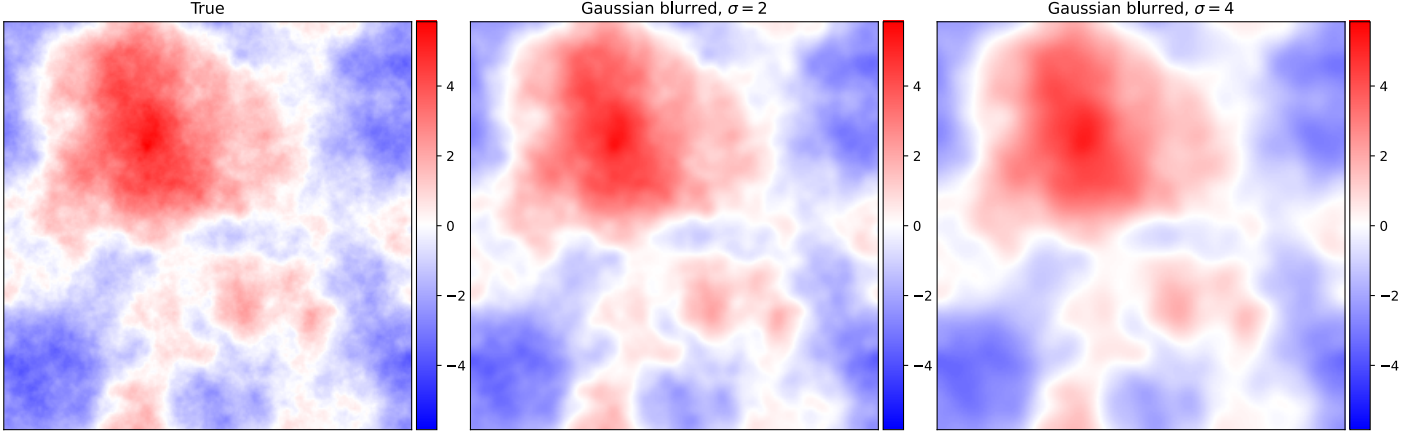


**Figure 31.** 2D fBM field (left) with the same field calculated with a Gaussian filter applied, reducing the resolution of the image by blurring structures smaller than the standard deviation  $\sigma = 2$  (middle), and  $\sigma = 4$  (right).

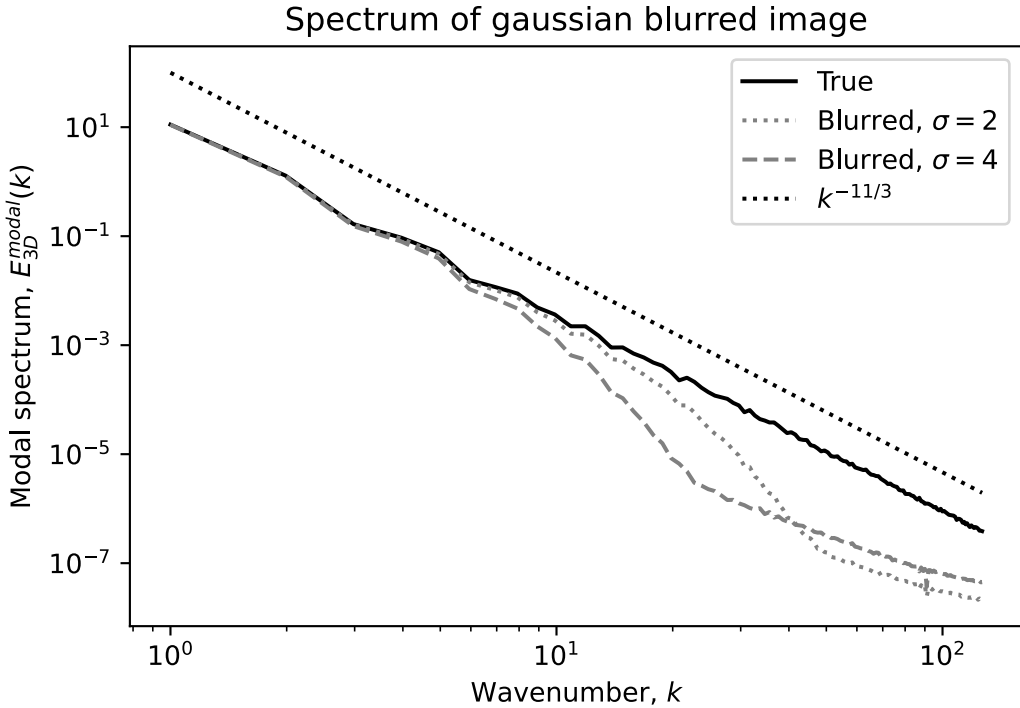


**Figure 32.** 2D modal power spectra calculated from Figure 31. The true image is displayed in solid black matching the expected power law of  $k^{-11/3}$  (dotted, black). The Gaussian convolved spectra are in gray where dotted is for  $\sigma = 2$  and dashed is for  $\sigma = 4$ .

where  $r$  is the radial distance from the center. The free parameters  $y_0$ ,  $\beta$ ,  $R_c$  indicate the maximum value of the core, the slope and the break/core radius respectively.

Figure 33 shows the 2D, sky-plane, generated mean field  $U_{2D}(\boldsymbol{\theta})$  on the left with  $y_0 = 2 \max\{u_{2D}\}$ ,  $\beta = 0.83$ , and  $R_c = 64$ . The 2D ( $256^2$ ), sky-plane, fluctuations ( $u_{2D}(\boldsymbol{\theta})$ ) as a generated fBM field of modal spectrum power law  $k^{-11/3}$ . The right most image shows the sum of the mean field and the fluctuations. The image is

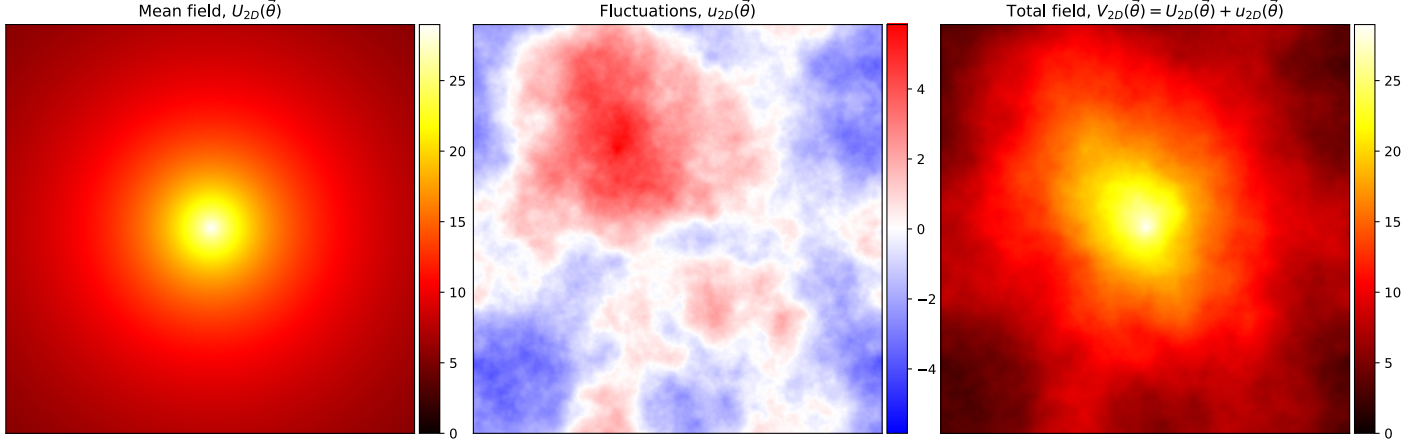


**Figure 33.** Figure showing a 2D generated  $\beta$  model, mean field  $U_{2D}(\boldsymbol{\theta})$  (with  $y_0$  as 5 times the maximum of the fluctuations,  $R_c = 64$ , and  $\beta = 0.83$ ), the fBM fluctuations and the total field that is the sum of the mean and the fluctuations.

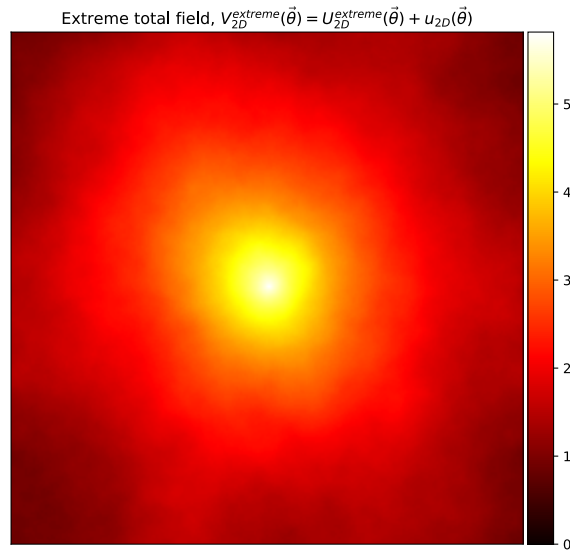


**Figure 34.** Figure showing the total field (sum of the fluctuations and the mean) with an extreme mean field where  $y_0$  is 10 times the maximum of the fluctuations.

1355 dominated by the mean field at large scales, but you can still see the smaller fluctuations  
 1356 contributing to the overall image. We also generate an extreme version of the  
 1357 mean field  $U_{2D}^{extreme}(\boldsymbol{\theta})$  with the only difference being,  $y_0 = 10 \max\{u_{2D}\}$ , and show  
 1358 the total field in Figure 34, it is now even harder to see the small scale structures  
 1359 of the fluctuations. We then compute the binned, modal power spectrum of these  
 1360 images (Figure 35) and, as expected, there is more energy (and the power spectrum  
 1361 is steeper) at the large scales (small wavenumber) compared to the fluctuations.

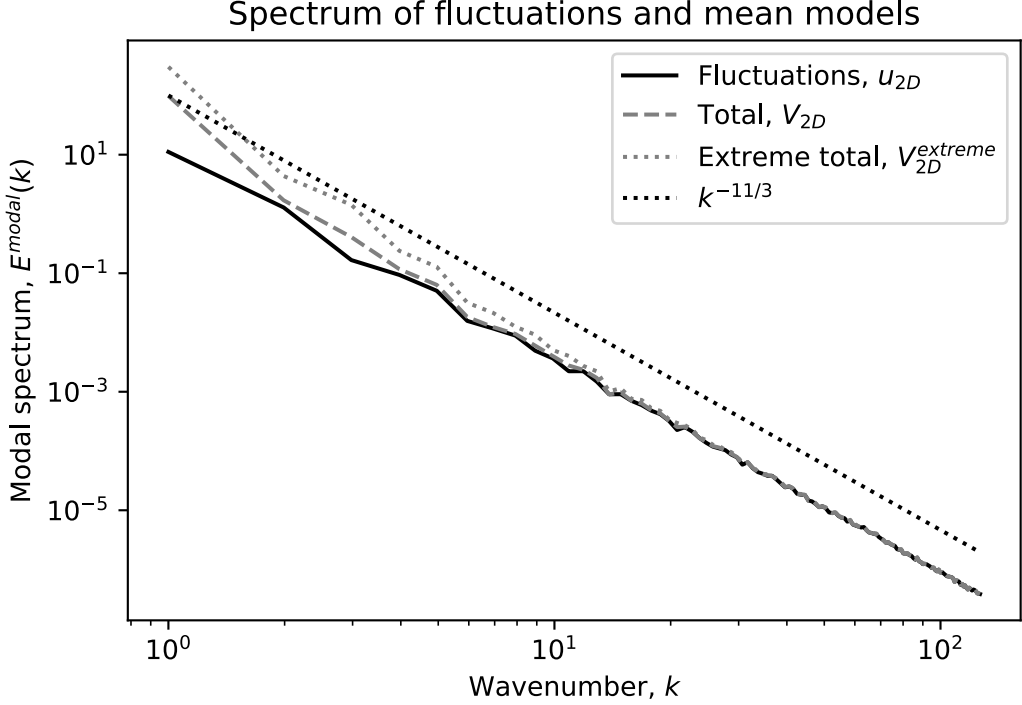


**Figure 35.** The modal energy spectra of the fBM fluctuations (in solid, black), the expected power law of  $k^{-11/3}$  (dotted, black) and the two total fields containing the mean/extreme mean fields plus the fluctuations (grey, dashed and dotted respectively).

### C.5. Projections

The line of sight integration projects along line-of-sight ( $\ell$ ) a 3D data cube onto the 2D plane of sky ( $\theta$ ) mimicing an astronomical observation of the 3D data,

$$y(\theta) = \frac{\int y(\theta, \ell) \epsilon(\theta, \ell) d\ell}{\int \epsilon(\theta, \ell) d\ell} \quad (\text{C97})$$

for a general emissivity  $\epsilon(\theta, \ell)$ . The emissivity function prescribes a weighting to the projection and can be set to a general temperature dependent cooling function  $n_i n_e \Lambda(T)$  (Churazov et al. 2012; Sutherland & Dopita 1993), or density weighting (Mohapatra et al. 2022b; Brunt & Mac Low 2004) etc. This is useful because an observation will depend on the emission along line of sight. In the discretized form,

$$y(\theta) = \frac{\sum_{\ell} y(\theta, \ell) \epsilon(\theta, \ell)}{\sum_{\ell} \epsilon(\theta, \ell)} \quad (\text{C98})$$

Figure 36 shows the a slice along  $\ell$ , of an fBM field on the left, and the line-of-sight integrated 2D image on the right, with  $\epsilon = 1$ . The colourbar scales are kept the same to show the overall decrease in the velocities. The projected image has also lost the finer scale structures visible in the slice. Figure 37 shows the calculated 2D/3D omni-directional (left) and modal (right) power spectra for the 2D sliced (solid gray), 2D projected (dashed gray) and full 3D (solid black) images. The full 3D image (solid

black) has an omni-directional power law of  $k^{-5/3}$  which arises from the fBM field generated with modal spectrum of  $k^{-11/3}$  as  $\mathcal{E}_{3D}^{\text{omni}}(k) = 4\pi k^2 E_{3D}^{\text{modal}}(k)$ .

The 2D slice (solid grey) has the same omni-directional spectrum of  $k^{-5/3}$  but shows a different modal spectrum of  $k^{-8/3}$ . This is expected as the 2D slice is the integral of the full 3D modal spectrum along the line of sight wavenumber  $k_z$

$$E_{2D}^{\text{red}}(k_2) = E_{2D}^{\text{red}}(k_x, k_y) \quad (\text{C99})$$

$$= \int_0^\infty E_{3D}^{\text{modal}}(k_x, k_y, k_z) dk_z \quad (\text{C100})$$

$$\propto \int_0^\infty (k_x^2 + k_y^2 + k_z^2)^{-\alpha_3/2} dk_z \quad (\text{C101})$$

$$= \sqrt{\pi} k_2^{-\alpha_3+1} \frac{\Gamma(\frac{\alpha_3-1}{2})}{2\Gamma(\frac{\alpha_3}{2})} \quad (\text{C102})$$

$$\propto k_2^{-\alpha_3+1} = k_2^{-\alpha_r} \quad (\text{C103})$$

when  $\alpha > 0$ ,  $k_2 = \sqrt{k_x^2 + k_y^2 + k_z^2}$ . Here, the 2D slice power law is  $\alpha_r = \alpha_3 - 1$  where  $\alpha_3$  is the 3D modal spectrum power law (set as 11/3 in the fBM field). Therefore, the 2D slice modal spectrum power law is the same as the 2D reduced spectrum power law of  $\alpha_r = \alpha_3 - 1 = 8/3$ . Following, the 2D omni-directional spectrum of the reduced spectrum is

$$\mathcal{E}_{2D}^{\text{red}}(k_2) \propto k_2 E_{2D}^{\text{red}}(k_2) \propto k_2^{-\alpha_r+1} = k_2^{-\beta_r} \quad (\text{C104})$$

which leads to the omni-directional spectrum power law of  $\beta_r = \alpha_r - 1 = 5/3$ , this is equal to the full 3D omni-directional spectrum power law  $\beta_3 = \beta_r$ . So the modal spectrum of a 2D slice at a fixed line-of-sight point, of a 3D fBM field is equivalent to the reduced spectrum along the line of sight.

The 2D projection (dashed grey) of the full 3D fBM field has an omni-directional power law of  $k^{-8/3}$  and a modal power law of  $k^{-11/3}$ . This is expected, as the real-space 2D projection is equivalent to setting wavenumbers  $k_\ell = 0$  in Fourier space (sometimes called the *projection-slice theorem*) where  $\ell$  is the line-of-sight variable (so  $k_\ell$  is the wavenumber along the line of sight). For a 3D modal spectrum

$$E_{3D}^{\text{modal}}(k_3) = E_{3D}^{\text{modal}}(k_x, k_y, k_z) \propto k_3^{-\alpha_3} \quad (\text{C105})$$

where  $k_3 = \sqrt{k_x^2 + k_y^2 + k_z^2}$ . Setting the line of sight wavenumbers to zero (now,  $k_z = 0$ ) obtains

$$E_{2D}^{\text{modal}}(k_2) = E_{2D}^{\text{modal}}(k_x, k_y) = E_{3D}^{\text{modal}}(k_x, k_y, 0) \propto k_2^{-\alpha_2} \quad (\text{C106})$$

where  $k_2 = \sqrt{k_x^2 + k_y^2}$ . Therefore, modal spectrum of the 2D projected image will have the same power law as the modal spectrum of the full 3D image ( $\alpha_2 = \alpha_3$ ). However, integrating over annuli in Fourier space to find the omni-directional spectrum of the projected 2D image (Appendix A):

$$\mathcal{E}_{2D}^{\text{omni}}(k_2) \propto k_2 E_{2D}^{\text{modal}}(k_2) \propto k_2^{-\alpha_3+1} = k_2^{-\beta_2} \quad (\text{C107})$$

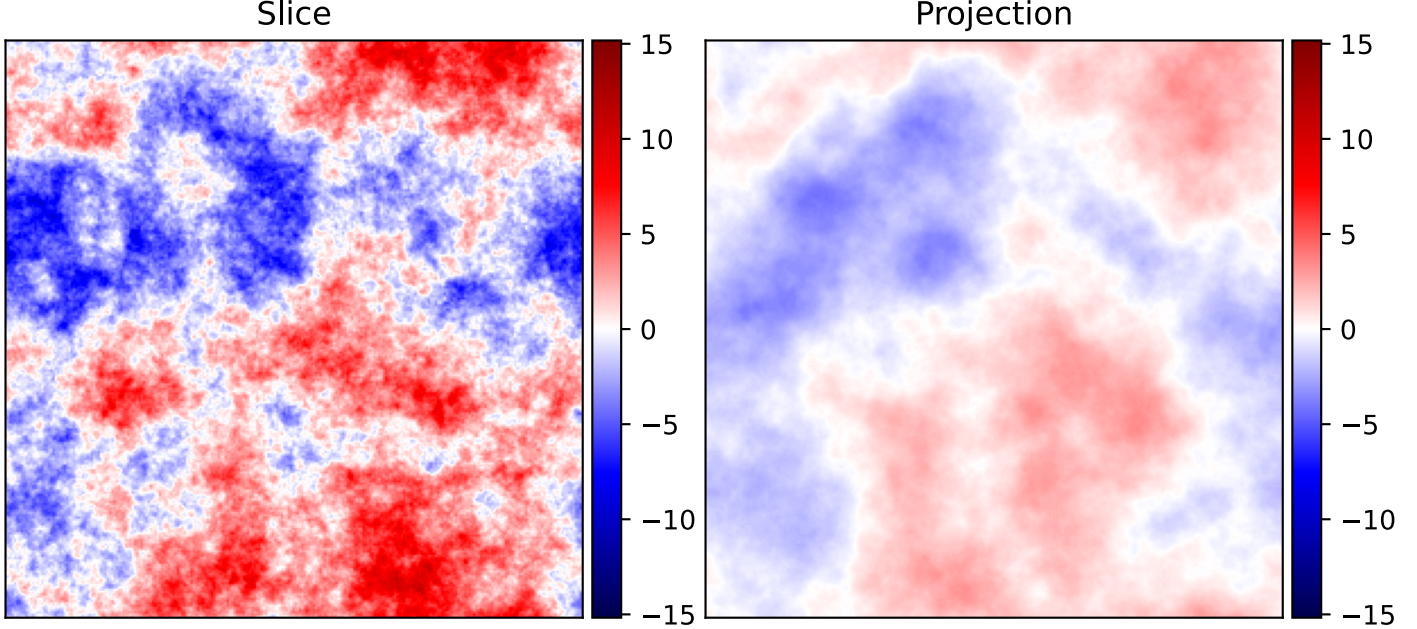


**Figure 36.** A slice perpendicular to the line-of-sight of a 3D fBM cube (left) and the 2D line-of-sight projection (right).

and the full 3D omni-directional spectrum is

$$\mathcal{E}_{3D}^{\text{omni}}(k_3) \propto k_3^2 E_{3D}^{\text{modal}}(k_3) \propto k_3^{-\alpha_3+2} = k_3^{-\beta_3} \quad (\text{C108})$$

therefore,

$$\beta_2 = \beta_3 + 1 \quad (\text{C109})$$

This shows that, for a expected modal spectrum of  $\alpha_3 = \alpha_2 = 11/3$ , the omni-directional spectrum power law of the full 3D image is  $\beta_3 = 5/3$  and the omni-directional spectrum power law of the 2D projected image is  $\beta_2 = \beta_3 + 1 = 8/3$  (Brunt et al. 2003).

For the second order structure function relation (Appendix A)

$$\mathcal{E}_{3D}^{\text{omni}}(k_3) = 4\pi k_3^2 E_{3D}^{\text{modal}}(k_3) \approx \frac{S_{2,3D}(1/k_3)}{k_3} \quad (\text{C110})$$

$$\mathcal{E}_{2D}^{\text{omni}}(k_2) = 4\pi k_2^2 E_{2D}^{\text{modal}}(k_2) \approx \frac{S_{2,2D}(1/k_2)}{k_2} \quad (\text{C111})$$

we obtain the following power law relation for the 3D structure function

$$S_{2,3D}(1/k_3) = k_3 \mathcal{E}_{3D}^{\text{omni}}(k_3) \propto k_3^{-\beta_3+1} = k_3^{-\gamma_3} \quad (\text{C112})$$

$$\implies S_{2,3D}(\lambda_3) \propto \lambda_3^{\gamma_3} \quad (\text{C113})$$

which is  $\gamma_3 = \beta_3 - 1$ . Similarly, the 2D (projected) structure function has

$$S_{2,2D}(1/k_2) = k_2 \mathcal{E}_{2D}^{\text{omni}}(k_2) \propto k_2^{-\beta_2+1} = k_2^{-\gamma_2} \quad (\text{C114})$$

$$\implies S_{2,2D}(\lambda_2) \propto \lambda_2^{\gamma_2} \quad (\text{C115})$$

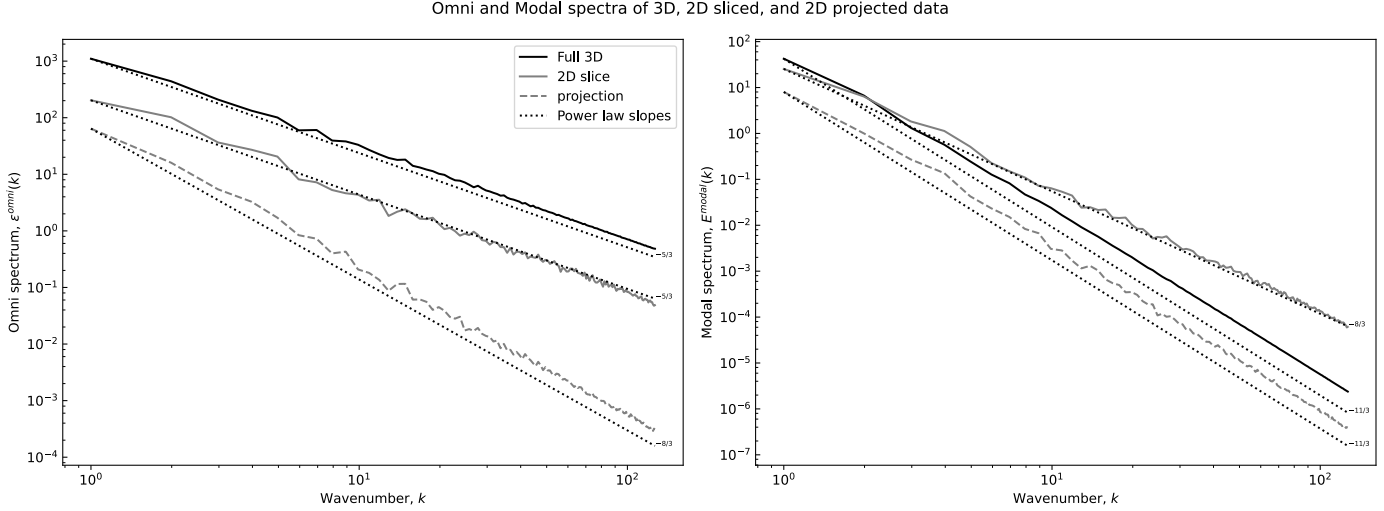


**Figure 37.** Omni-directional (left) and modal (right) spectra of the 2D fBM field (Figure 36). In solid black, the full 3D spectrum which has the expected modal slope of  $k^{-11/3}$  and omni-directional slope of  $k^{-5/3}$ . The 2D projection (dashed grey) has the same modal slope  $k^{-11/3}$  but a steeper omni-directional slope of  $k^{-8/3}$ . The 2D slice (solid grey) has the omni-directional slope of  $k^{-5/3}$  but a modal slope of  $k^{-8/3}$ . These differences naturally arise from definitions of the 2D vs 3D omni-directional, modal and reduced spectra with isotropic fBM field.

	$\alpha$	$\beta$	$\gamma$	$\delta$
3	$\alpha_3$	$\beta_3 = \alpha_3 - 2$	$\gamma_3 = \beta_3 - 1$	$\delta_3 = \frac{1}{2}(\beta_3 - 1)$
2	$\alpha_2 = \alpha_3$	$\beta_2 = \beta_3 + 1$	$\gamma_2 = \gamma_3 + 1$	$\delta_2 = \delta_3 + 1/2$
$r$	$\alpha_r = \alpha_3 - 1$	$\beta_r = \beta_3$	$\gamma_r = \gamma_3$	$\delta_r = \delta_3$

**Table 1.** Relations between 2D projected (subscript 2) and 2D reduced (subscript  $r$ , slice) power laws with the full 3D power laws (subscript 3) where  $\alpha$  is the modal spectrum,  $\beta$  is the omni-directional spectrum,  $\gamma$  is the structure function, and  $\delta$  is the amplitude spectrum.

with relation  $\gamma_2 = \beta_2 - 1 = \gamma_3 + 1$ . Since the 2D slice (reduced) spectrum has the same omni-directional spectrum power law as the full 3D spectrum  $\beta_r = \beta_3$ , the 2D slice structure function power law is the same as the full 3D structure function  $\gamma_r = \gamma_3 = \beta_3 - 1$ . For Kolmogorov omni-directional spectrum scaling  $\beta_r = \beta_3 = 5/3$ , the expected second order structure function power law is  $\gamma_3 = \gamma_r = 2/3$  and  $\gamma_2 = \gamma_3 + 1 = 5/3$ .

For ease, Table 1 shows the expected 2D projection (subscript 2) and 2D slice (subscript  $r$ ) power law relations shown thus far as functions of the true 3D power laws and the transformations of the true 3D power laws to one another (subscript 3).

#### C.6. Fourier transform

We will start off by defining a continuous signal  $y_c(x)$  as a function of position  $x$  and express its Fourier transform  $\hat{y}_c(k)$  as a function of angular wavenumber  $k = 2\pi q$

1453 (i.e. including the  $2\pi$  factor):

1454  $y_c(x) = \frac{1}{2\pi} \int_{-\infty}^{\infty} \hat{y}_c(k) e^{ikx} dk$  (C116)

1455  $\hat{y}_c(k) = \int_{-\infty}^{\infty} y_c(x) e^{-ikx} dx$  (C117)

1457 here, the normalization factor of  $2\pi$  is chosen to be applied to the backwards transform  
 1458 (transforming the frequency domain to the real-space domain). The data we obtain  
 1459 in real life is not the continuous data, but rather, a discrete function that is obtained  
 1460 by sampling an underlying continuous function at a rate  $\Delta x$ . This gives the discrete  
 1461 function  $y[n]$  and its Fourier transform  $\hat{y}[m]$ , defined as the following:

1462  $y[n] = y_c(n\Delta x) = y_c(x)$  (C118)

1463  $\hat{y}[m] = \hat{y}_c(m\Delta k) = \hat{y}_c(k)$  (C119)

1465 If we assume that  $y_c(x)$  is periodic on the domain  $x \in [0, L]$  such that  $y_c(x) = y_c(x+L)$ ,  
 1466 and we have sampled  $N$  evenly separated points within this domain, our sampling  
 1467 rate is  $\Delta x = L/N$ . The discrete function will also be continuous  $y[n] = y[n+N]$  for  
 1468  $n \in [0, N]$ ,  $m \in [-N/2, N/2]$ . As a result, the Fourier-space function is also periodic  
 1469  $\hat{y}_c(k) = \hat{y}_c(k + N\Delta k)$  where  $\Delta k = \frac{2\pi}{N\Delta x} = \frac{2\pi}{L}$  and  $k \in [-\pi N/L, \pi N/L]$ . The last  
 1470 step in this process is to acknowledge the following relation for the discretization of  
 1471 the complex exponential term:  $xk = (n\Delta x)(m\Delta k) = nm\Delta x 2\pi/(N\Delta x) = 2\pi nm/N$ .  
 1472 Applying the relations stated gives us the discrete form of the continuous signal  
 1473 and its Fourier transform, where we have also replaced  $dx$  and  $dk$  with  $\Delta x$  and  $\Delta k$   
 1474 respectively

1475  $y[n] = \frac{\Delta k}{2\pi} \sum_m \hat{y}[m] e^{2\pi i n m / N}$  (C120)

1476  $\hat{y}[m] = \Delta x \sum_n y[n] e^{-2\pi i n m / N}$  (C121)

1478 Following the same method, we can convert Parseval's theorem from the continuous  
 1479 case to the discrete case

1480  $\int_{-\infty}^{\infty} |y_c(t)|^2 dt = \frac{1}{2\pi} \int_{-\infty}^{\infty} |\hat{y}_c(k)|^2 dk$  (C122)

1481  $\implies \Delta x \sum_n |y[n]|^2 = \frac{\Delta k}{2\pi} \sum_m |\hat{y}[m]|^2$  (C123)

1483 We can derive the generalized D-dimensional form of the DFT using the same arguments  
 1484 provided above, which we state as the following:

1485  $y[\mathbf{n}] = \left( \frac{\Delta \mathbf{k}}{2\pi} \right)^D \sum_{\mathbf{m}} \hat{y}[\mathbf{m}] e^{2\pi i \mathbf{n} \cdot \mathbf{m} / \mathbf{N}}$  (C124)

1486  $\hat{y}[\mathbf{m}] = \Delta \mathbf{x}^D \sum_{\mathbf{n}} y[\mathbf{n}] e^{-2\pi i \mathbf{n} \cdot \mathbf{m} / \mathbf{N}}$  (C125)

1488 where  $\mathbf{n} \cdot \mathbf{m}/N = [n_1 m_1/N_1, n_2 m_2/N_2, \dots n_D m_D/N_D]$ ,  $\Delta\mathbf{x}^D = \Delta x_1 \Delta x_2 \dots \Delta x_D$ , and  
 1489  $\Delta k^D = \Delta k_1, \Delta k_2, \dots \Delta k_D$ .

1490 The D-dimensional DFT is implemented using the `pyfftw` backend for the  
 1491 `scipy.fft` package. The DFT is called using the `scipy.fft.fftn` method, and  
 1492 the wavenumbers are obtained using `scipy.fft.fftfreq`, providing it the number  
 1493 of sampled data points  $N$  (this gives  $m/N$  for  $m \in [-N/2, N/2]$ ) and multiplying it  
 1494 by  $2\pi/\Delta x$ .

1495                   C.7. Statistics

1496                   C.7.1. Moments

1497 Generate statistical moments of a function are provided by `analysis_engine.statistics.moments`;  
 1498 this calculates the integral of the absolute value of some variable to a power  $p$  for  
 1499 moments of order  $p$

1500                   
$$\int |y(\mathbf{x})|^p d\mathbf{x} \rightarrow \Delta x^D \sum_{\mathbf{n}} |y[\mathbf{n}]|^p \quad (\text{C126})$$
  
 1501

1502 If the volume averaged moments are required, then simply divide by the volume  
 1503  $V = L^D$

1504                   
$$\left(\frac{\Delta x}{L}\right)^D \sum_{\mathbf{n}} |y[\mathbf{n}]|^p = \frac{1}{N^D} \sum_{\mathbf{n}} |y[\mathbf{n}]|^p \quad (\text{C127})$$
  
 1505

1506                   C.7.2. Correlation

1507                   `analysis_engine.statistics.statfunc.corr` provides utility to calculate the *bias*-  
 1508 *ased* correlation function, calculated with the following formula

1509                   
$$R[\boldsymbol{\lambda}] = \Delta x^D \sum_{\mathbf{n}} y[\mathbf{n}] y[\mathbf{n} + \boldsymbol{\lambda}] \quad (\text{C128})$$
  
 1510

1511 This method takes as parameter the lags to compute the correlation at, this is typically  
 1512 done with all the possible lags or log-spaced lags for large simulation cubes. An  
 1513 alternative way of calculating the correlation function is to use the Fourier transform

1514                   
$$R[\boldsymbol{\lambda}] = \Re \left\{ \frac{\Delta k^D}{(2\pi)^D} \mathcal{F}^{-1} \{ \hat{y}[\mathbf{m}] \hat{y}^*[\mathbf{m}] \} \right\} \quad (\text{C129})$$
  
 1515

1516 where  $\hat{y}[\mathbf{m}]$  is the Fourier transform of  $y[\mathbf{n}]$ ,  $\hat{y}^*$  is the complex conjugate of  $\hat{y}$ ,  $\mathcal{F}^{-1}$  is  
 1517 taking the inverse Fourier transform, and  $\Re$  means to take the real component only.

1518 Figure 38 shows a 2D slice (at line-of-sight lag  $\lambda_\ell = \lambda_z = 0$ ) for the autocorrelation  
 1519 function (left). The right plot shows the same autocorrelation function but averaged  
 1520 over spherical shells with lags of magnitude  $\lambda = |\boldsymbol{\lambda}|$  (black) with shading showing  
 1521 the standard deviation. The grey dotted line and hatching shows the FFT method  
 1522 binned autocorrelation function and its standard deviation respectively.

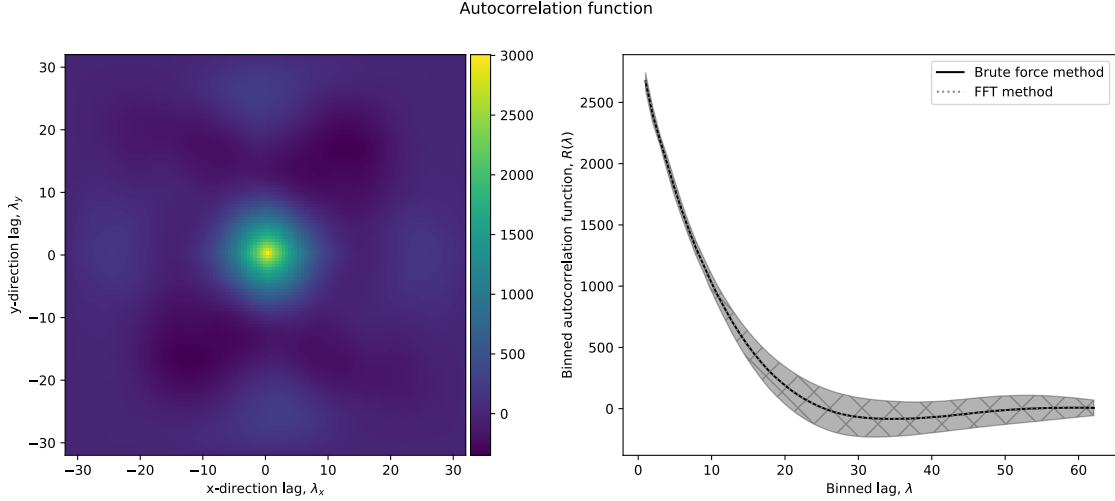


**Figure 38.** A 2D slice (at line-of-sight lag  $\lambda_\ell = 0$ ) of the 3D autocorrelation function (left). On the right is the same 3D autocorrelation function but averaged over spherical shells with lags of magnitude  $\lambda = |\boldsymbol{\lambda}|$  (black) with shading indicating the standard deviation. In dotted grey is the autocorrelation function calculated using the Fourier transform method and averaged over spherical shells with the grey hatching indicating the standard deviation. Clearly, the brute force method is the exact same as the Fourier transform method.

1523

### C.7.3. Structure function

1524

`analysis_engine.statistics.statfunc.strfn` provides ways to calculate the structure function of order  $p$ , the discretized formula is:

1526

$$S_p[\boldsymbol{\lambda}] = \Delta x^D \sum_{\mathbf{n}} |y[\mathbf{n}] - y[\mathbf{n} + \boldsymbol{\lambda}]|^p \quad (\text{C130})$$

1527

1528

which can be computed for any requested lags. Typically these lags will either be the entire lag-space which can be computationally time consuming for large data cubes, or log-spaced. We can also approximate the second order structure function in the inertial range by expanding its definition ([Appendix A](#)):

1532

$$\tilde{S}_2[\boldsymbol{\lambda}] = 2R[\mathbf{0}] - 2R[\boldsymbol{\lambda}] \quad (\text{C131})$$

1533

1534

This method can be much faster to calculate as we can also calculate  $R[\boldsymbol{\lambda}]$  using the FFT method.

1536

[Figure 39](#) shows a 2D slice (at line-of-sight lag  $\lambda_\ell = \lambda_z = 0$ ) of the true 3D second order structure function on the left and the binned structure function, where we have averaged over lags of magnitude  $\lambda = |\boldsymbol{\lambda}|$  for each lag. The black line and shading shows the true second order structure function and the grey line and shading show the approximation method. Both methods show the same power law inertial range slope and amplitude at large lag, but the FFT method has a higher amplitude at small lags.

1537

1538

1539

1540

1541

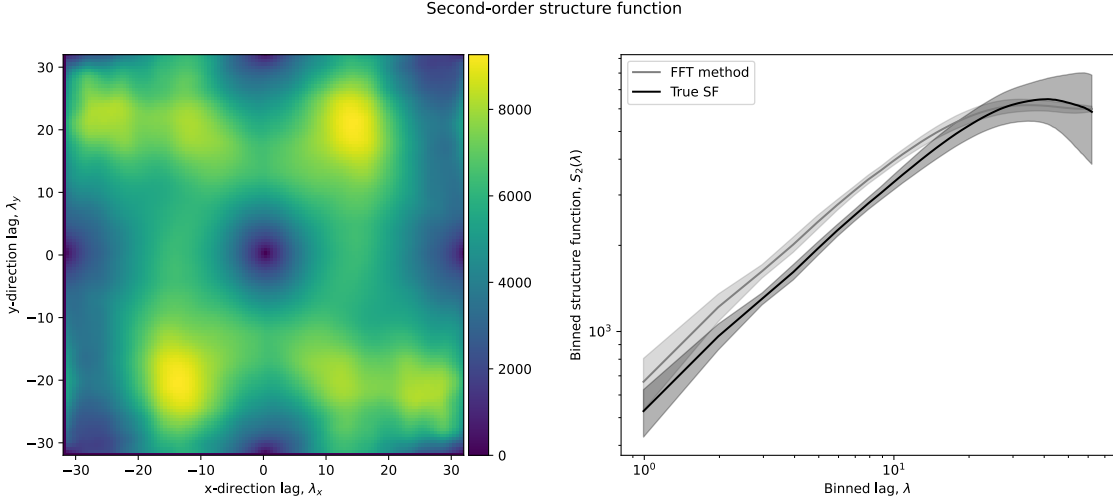


**Figure 39.** A 2D slice (at line-of-sight lag  $\lambda_\ell = 0$ ) of the 3D second order structure function (left). On the right is the same 3D autocorrelation function but averaged over spherical shells with lags of magnitude  $\lambda = |\boldsymbol{\lambda}|$  (black) with shading indicating the standard deviation. In grey is the structure function calculated using the approximation method and averaged over spherical shells with the grey shading indicating the standard deviation. The two methods show the same power law and amplitude at maximum lag but differ in amplitude at small lags.

### 1543 C.8. Spectrum types

#### 1544 C.8.1. Omni-directional spectrum

1545 The *omni-directional spectrum* is a simple binning of wavenumber magnitudes  $k =$   
1546  $|\boldsymbol{k}|$

$$1547 \quad \mathcal{E}^{\text{modal}}[m] = \frac{1}{\Delta k} \sum_{k \leq |\boldsymbol{k}| < k + \Delta k} E^{\text{modal}}(\boldsymbol{k}) \quad (\text{C132})$$

1549 where we have used `scipy.stats.binned_statistic()` to process the binnings. The  
1550  $\Delta k$  factor here is to allow for the binning over a range of  $k$  values (to save compute  
1551 time), by default, this value is 1 when binning between each adjacent wavenumbers.

#### 1552 C.8.2. Modal spectrum

1553 The modal spectrum is the following

$$1554 \quad E^{\text{modal}}[m] = \frac{1}{\Delta k} \frac{1}{N} \sum_{k \leq |\boldsymbol{k}| < k + \Delta k} E^{\text{modal}}(\boldsymbol{k}) \quad (\text{C133})$$

1556 where  $N$  is the number of points in that bin (which equates to  $N = 4\pi k^2$  in 3D). This  
1557 is essentially calculating the *omni-directional spectrum* and then dividing it by the bin  
1558 sizes to get the isotropic, *modal spectrum*. This is implemented using the same code  
1559 as the *omni-directional spectrum*, but we tell `scipy.stats.binned_statistic()` to  
1560 return the average instead of the sum.

### 1561 C.9. Spectrum methods

1562 The implementations for the various spectral methods lie in the  
 1563 folder named `analysis_engine.statistics.spectra`. Whilst each  
 1564 method can be accessed individually, it may also be easier to call  
 1565 `spectra.spectra_base.calculate_integrated_spectrum()` as a single, general  
 1566 use function to calculate spectra by providing it the `spec_type` ('modal', 'omni',  
 1567 'amplitude') and the `method` ('periodogram', 'correlogram', 'strfn', 'arevalo', and  
 1568 'flatsky').

#### 1569 C.9.1. Periodogram

1570 The implementation for the *periodogram spectrum* can be found in  
 1571 `spectra.per_spectra.modal_spectra()` which calculates the following

$$1572 E^{\text{per}}[\mathbf{m}] = \left( \frac{\Delta k}{2\pi} \right)^D |\mathcal{F}\{y[\mathbf{n}]\}[\mathbf{m}]|^2 \quad (C134)$$

1574 This is the simplest method for estimating the modal spectrum of a  $D$ -dimensional  
 1575 variable  $u(\mathbf{x})$ , originally developed to examine the periodicity of a signal, hence the  
 1576 name (Schuster 1898).

#### 1577 C.9.2. Correlogram

1578 The implementation for the *correlogram spectrum* can be found in  
 1579 `spectra.corr_spectra.omni_spectra()` which takes a  $D$ -dimensional correlation  
 1580 function  $R[\ell]$  and computes the FFT on that

$$1581 E^{\text{corr}}[\mathbf{m}] = \left( \frac{\Delta k}{2\pi} \right)^D \Delta \ell^D \mathcal{F}\{R[\ell]\}[\mathbf{m}] \quad (C135)$$

1583 It is important to note: the autocorrelation function typically spans  $\ell \in [-N, N]$  (or  
 1584  $r \in [-L, L]$ ); hence  $\Delta k = \frac{\pi}{L}$ .

1585 When no window function is applied, this method can appear noisy, to smooth out  
 1586 some of the noise: first, average the autocorrelation function into bins of lag  $\ell = |\ell|$   
 1587 (giving  $R[\ell]$ ); taking the Fourier transform obtains the *omni-directional spectrum*

$$1588 E^{\text{omni}}[m] = \frac{\Delta k}{2\pi} \Delta \ell \mathcal{F}\{R[\ell]\}[m] \quad (C136)$$

1590 Another method to reduce the noise is to cut the autocorrelation function at a  
 1591 certain lag  $\ell \leq N/2$ ; say  $\ell \in [-N/2, N/2]$  (or  $r \in [-L/2, L/2]$ ). Therefore, the  
 1592 spectrum is

$$1593 E^{\text{corr}}[\mathbf{m}] = \left( \frac{\Delta k}{2\pi} \right)^D \Delta \ell^D \mathcal{F}\{R[\ell]\}[\mathbf{m}] \quad (C137)$$

1595 and now, we are back to the usual  $\Delta k = \frac{2\pi}{L}$ . Doing it this way retains the same  
 1596 discrete wavenumbers as the *periodogram* method. If we multiply the autocorrelation  
 1597 function with a window function, we get the Blackman-Tukey method (Blackman  
 1598 et al. 1960).

1599                   C.9.3. *Structure function*

1600       Providing a second order structure function  $S_2[\mathbf{m}]$  (C.7)) to the method  
 1601       `strfn_spectra.omni_spectrum()` calculates the following discretized equivalent  
 1602       *omni-directional spectrum*

1603                   
$$\mathcal{E}^{\text{SF}}[m] = \frac{\Delta k}{2\pi} \frac{S_2[m]}{m\Delta k} \quad (\text{C138})$$
  
 1604

1605       where the  $\Delta k/2\pi$  term has been added to give it similar normalization to the peri-  
 1606       odogram (via Parseval's theorem). However, it should be noted that this method does  
 1607       not satisfy Parseval's theorem. If the provided structure function is  $D$ -dimensional  
 1608        $S_2[\mathbf{m}]$ , then the method bins lags of equal magnitude.

1609                   C.9.4. *Arevalo method*

1610       The file `arevalo_spectra.modal_spectrum()` provides the power spectrum of the  
 1611       Arevalo method. It should be noted that the algorithm was designed for two di-  
 1612       mensional images, but it does generalize to higher (and lower) dimensions. When an  
 1613       exposure map  $\Xi[\mathbf{n}]$  is applied, with a mask defined as

1614                   
$$M[\mathbf{n}] = \begin{cases} 0 & \text{where } \Xi[\mathbf{n}] = 0 \\ 1 & \text{otherwise} \end{cases} \quad (\text{C139})$$
  
 1615

1616       the generalized Arevalo method is calculated as

1617                   
$$E^{\text{arevalo}}[m] = \frac{\Delta x^D}{\sum_{\mathbf{m}} |\hat{f}[\mathbf{m}]|^2} \sum_{\mathbf{n}} \left| \Xi \frac{(y * g_1) - (y * g_2)}{(\Xi * g_1) - (\Xi * g_2)} \right|^2 \quad (\text{C140})$$
  
 1618

1619       where the Gaussian convolutions have been calculated using `scipy.ndimage.gaussian_filter()`  
 1620       and the Fourier filter function is defined as  $\hat{f}[m] = e^{-k^2\sigma_1^2/2} - e^{-k^2\sigma_2^2/2}$ . The values of  
 1621        $\sigma$  are defined as

1622                   
$$\sigma = o\Delta x \frac{\sqrt{2}}{\pi} \quad (\text{C141})$$
  
 1623

1624       where  $\Delta x = L/N$  and  $o \in [1, N/2]$ ; this way,  $k_{max} = \sqrt{2}/\sigma \in [\frac{2\pi}{L}, \frac{\pi N}{L}]$  which spans the  
 1625       same wavenumbers as the ordinary Fourier methods for arbitrary  $L$  and  $N$ . When  
 1626       using the `gaussian_filter()` method, provide it with just  $o\sqrt{2}/\pi$  instead. It is also  
 1627       easier to normalize with respect to the Gaussian function in configuration space (as  
 1628       the Gaussian in Fourier space has a width of  $1/\sigma$ ) which is accomplished with the  
 1629       following:

1630                   
$$E^{\text{arevalo}}[m] = \left( \frac{\Delta k}{2\pi} \right)^D \frac{1}{\sum_{\mathbf{n}} |f[\mathbf{n}]|^2} \sum_{\mathbf{n}} \left| \Xi \frac{(y * g_1) - (y * g_2)}{(\Xi * g_1) - (\Xi * g_2)} \right|^2 \quad (\text{C142})$$
  
 1631

1632       Lastly, it is easier to generate the Gaussian to the size of the image; this is not  
 1633       always necessary but there are situations where integer rounding (if generating the  
 1634       distribution across  $M\sigma$  points, where  $M \in \mathbb{N}$ ) for specific  $\sigma$  values causes distinct  
 1635       peaks in the resultant power spectrum.

1636            C.9.5. *Spherical harmonics: flat-sky approximation*

1637        The spherical harmonic form of the power spectrum is calculated using  
1638        `pymaster`; the python implementation of the `NaMaster` library ([Alonso et al.](#)  
1639        [2019](#)). `pymaster` provides the flatsky power spectrum estimate through the  
1640        `nmt.NmtBinFlat()` class. We call the `pymaster` implementation through the file  
1641        `flatsky_spectra.modal_spectrum()`.

## REFERENCES

- 1642 Alonso, D., Sanchez, J., Slosar, A., &  
 1643 LSST Dark Energy Science  
 1644 Collaboration. 2019, Monthly Notices of  
 1645 the Royal Astronomical Society, 484,  
 1646 4127, doi: [10.1093/mnras/stz093](https://doi.org/10.1093/mnras/stz093)
- 1647 Angelinelli, M., Ettori, S., Vazza, F., &  
 1648 Jones, T. W. 2021, Astronomy and  
 1649 Astrophysics, 653, A171,  
 1650 doi: [10.1051/0004-6361/202140471](https://doi.org/10.1051/0004-6361/202140471)
- 1651 Arnaud, M. 2009, A&A, 500, 103,  
 1652 doi: [10.1051/0004-6361/200912150](https://doi.org/10.1051/0004-6361/200912150)
- 1653 Arévalo, P., Churazov, E., Zhuravleva, I.,  
 1654 Hernández-Monteagudo, C., &  
 1655 Revnivtsev, M. 2012, Monthly Notices  
 1656 of the Royal Astronomical Society, 426,  
 1657 1793,  
 1658 doi: [10.1111/j.1365-2966.2012.21789.x](https://doi.org/10.1111/j.1365-2966.2012.21789.x)
- 1659 Barbour, A. J., & Parker, R. L. 2022,  
 1660 Normalization of Power Spectral  
 1661 Density Estimates.  
<https://cran.rstudio.com/web/packages/psd/index.html>
- 1664 Batchelor, G. K. 1953, The Theory of  
 1665 Homogeneous Turbulence.  
<https://ui.adsabs.harvard.edu/abs/1953tht..book.....B>
- 1668 Bensch, F., Stutzki, J., & Ossenkopf, V.  
 1669 2001, Astronomy and Astrophysics, 366,  
 1670 636, doi: [10.1051/0004-6361:20000292](https://doi.org/10.1051/0004-6361:20000292)
- 1671 Blackman, R. B., Tukey, J. W., &  
 1672 Teichmann, T. 1960, Physics Today, 13,  
 1673 52, doi: [10.1063/1.3056826](https://doi.org/10.1063/1.3056826)
- 1674 Bonafede, A., Feretti, L., Murgia, M.,  
 1675 et al. 2010, Astronomy and  
 1676 Astrophysics, Volume 513, id.A30,  
 1677 <NUMPAGES>21</NUMPAGES>  
 1678 pp., 513, A30,  
 1679 doi: [10.1051/0004-6361/200913696](https://doi.org/10.1051/0004-6361/200913696)
- 1680 Boyden, R. D., Koch, E. W., Rosolowsky,  
 1681 E. W., & Offner, S. S. R. 2016, The  
 1682 Astrophysical Journal, 833, 233,  
 1683 doi: [10.3847/1538-4357/833/2/233](https://doi.org/10.3847/1538-4357/833/2/233)
- 1684 Boyden, R. D., Offner, S. S. R., Koch,  
 1685 E. W., & Rosolowsky, E. W. 2018, The  
 1686 Astrophysical Journal, 860, 157,  
 1687 doi: [10.3847/1538-4357/aac76d](https://doi.org/10.3847/1538-4357/aac76d)
- 1688 Brandenburg, A., & Lazarian, A. 2013,  
 1689 Space Science Reviews, 178, 163,  
 1690 doi: [10.1007/s11214-013-0009-3](https://doi.org/10.1007/s11214-013-0009-3)
- 1691 Brandenburg, A., & Nordlund, 2011,  
 1692 Reports on Progress in Physics, 74,  
 1693 046901,  
 1694 doi: [10.1088/0034-4885/74/4/046901](https://doi.org/10.1088/0034-4885/74/4/046901)
- 1695 Brentjens, M. A., & de Bruyn, A. G. 2005,  
 1696 Astronomy and Astrophysics, 441,  
 1697 1217, doi: [10.1051/0004-6361:20052990](https://doi.org/10.1051/0004-6361:20052990)
- 1698 Brunt, C. M., & Heyer, M. H. 2002, The  
 1699 Astrophysical Journal, 566, 276,  
 1700 doi: [10.1086/338031](https://doi.org/10.1086/338031)
- 1701 Brunt, C. M., Heyer, M. H.,  
 1702 Vázquez-Semadeni, E., & Pichardo, B.  
 1703 2003, The Astrophysical Journal, 595,  
 1704 824, doi: [10.1086/377479](https://doi.org/10.1086/377479)
- 1705 Brunt, C. M., & Mac Low, M.-M. 2004,  
 1706 The Astrophysical Journal, 604, 196,  
 1707 doi: [10.1086/381648](https://doi.org/10.1086/381648)
- 1708 Carilli, C. L., & Taylor, G. B. 2002,  
 1709 Annual Review of Astronomy and  
 1710 Astrophysics, 40, 319, doi: [10.1146/annurev.astro.40.060401.093852](https://doi.org/10.1146/annurev.astro.40.060401.093852)
- 1712 Chepurnov, A., & Lazarian, A. 2009, The  
 1713 Astrophysical Journal, 693, 1074,  
 1714 doi: [10.1088/0004-637X/693/2/1074](https://doi.org/10.1088/0004-637X/693/2/1074)
- 1715 Chhiber, R., Chasapis, A.,  
 1716 Bandyopadhyay, R., et al. 2018, Journal  
 1717 of Geophysical Research: Space Physics,  
 1718 123, 9941, doi: [10.1029/2018JA025768](https://doi.org/10.1029/2018JA025768)
- 1719 Churazov, E., Vikhlinin, A., Zhuravleva,  
 1720 I., et al. 2012, Monthly Notices of the  
 1721 Royal Astronomical Society, 421, 1123,  
 1722 doi: [10.1111/j.1365-2966.2011.20372.x](https://doi.org/10.1111/j.1365-2966.2011.20372.x)
- 1723 Corrsin, S. 1959, in Atmospheric Diffusion  
 1724 and Air Pollution, Advances in  
 1725 Geophysics, vol. 6, ed. F. Frenkel &  
 1726 P. Sheppard (New York: Academic  
 1727 Press), 161
- 1728 Courtois, H. M., Pomarède, D., Tully,  
 1729 R. B., Hoffman, Y., & Courtois, D.  
 1730 2013, The Astronomical Journal, 146,  
 1731 69, doi: [10.1088/0004-6256/146/3/69](https://doi.org/10.1088/0004-6256/146/3/69)
- 1732 Davidson, P. A., & Nelkin, M. 2005,  
 1733 Physics Today, 58, 80,  
 1734 doi: [10.1063/1.2138427](https://doi.org/10.1063/1.2138427)
- 1735 de Vries, M., Mantz, A. B., Allen, S. W.,  
 1736 et al. 2023, Monthly Notices of the  
 1737 Royal Astronomical Society, 518, 2954,  
 1738 doi: [10.1093/mnras/stac3285](https://doi.org/10.1093/mnras/stac3285)

- 1739 Domínguez-Fernández, P., Vazza, F.,  
 1740 Brüggen, M., & Brunetti, G. 2019,  
 1741 Monthly Notices of the Royal  
 1742 Astronomical Society, 486, 623,  
 1743 doi: [10.1093/mnras/stz877](https://doi.org/10.1093/mnras/stz877)
- 1744 Donnert, J., Vazza, F., Brüggen, M., &  
 1745 ZuHone, J. 2018, Space Science  
 1746 Reviews, 214, 122,  
 1747 doi: [10.1007/s11214-018-0556-8](https://doi.org/10.1007/s11214-018-0556-8)
- 1748 Drissen, L., Bernier, A.-P.,  
 1749 Rousseau-Nepton, L., et al. 2010, in  
 1750 Ground-based and Airborne  
 1751 Instrumentation for Astronomy III, Vol.  
 1752 7735 (SPIE), 167–176,  
 1753 doi: [10.1117/12.856470](https://doi.org/10.1117/12.856470)
- 1754 Enßlin, T. A., & Vogt, C. 2003,  
 1755 Astronomy and Astrophysics, v.401,  
 1756 p.835-848 (2003), 401, 835,  
 1757 doi: [10.1051/0004-6361:20030172](https://doi.org/10.1051/0004-6361:20030172)
- 1758 Esquivel, A., Lazarian, A., Pogosyan, D.,  
 1759 & Cho, J. 2003, Monthly Notices of the  
 1760 Royal Astronomical Society, 342, 325,  
 1761 doi: [10.1046/j.1365-8711.2003.06551.x](https://doi.org/10.1046/j.1365-8711.2003.06551.x)
- 1762 Fang, X.-E., Guo, F., Yuan, Y.-F., &  
 1763 Mou, G. 2018, The Astrophysical  
 1764 Journal, 863, 177,  
 1765 doi: [10.3847/1538-4357/aad1f6](https://doi.org/10.3847/1538-4357/aad1f6)
- 1766 Feddersen, J. R., Arce, H. G., Kong, S.,  
 1767 Ossenkopf-Okada, V., & Carpenter,  
 1768 J. M. 2019, The Astrophysical Journal,  
 1769 875, 162,  
 1770 doi: [10.3847/1538-4357/ab0e7d](https://doi.org/10.3847/1538-4357/ab0e7d)
- 1771 Frisch, U. 1995, Turbulence. The legacy of  
 1772 A.N. Kolmogorov. <https://ui.adsabs.harvard.edu/abs/1995tlan.book.....F>
- 1773 Fryxell, B., Olson, K., Ricker, P., et al.  
 1775 2000, Astrophys. J. Suppl. Ser, 131,  
 1776 273334, doi: [10.1086/317361](https://doi.org/10.1086/317361)
- 1777 Garaldi, E., Pakmor, R., & Springel, V.  
 1778 2021, Monthly Notices of the Royal  
 1779 Astronomical Society, 502, 5726,  
 1780 doi: [10.1093/mnras/stab086](https://doi.org/10.1093/mnras/stab086)
- 1781 Gaspari, M., & Churazov, E. 2013,  
 1782 Astronomy and Astrophysics, 559, A78,  
 1783 doi: [10.1051/0004-6361/201322295](https://doi.org/10.1051/0004-6361/201322295)
- 1784 Gaspari, M., Churazov, E., Nagai, D.,  
 1785 Lau, E. T., & Zhuravleva, I. 2014,  
 1786 Astronomy and Astrophysics, 569, A67,  
 1787 doi: [10.1051/0004-6361/201424043](https://doi.org/10.1051/0004-6361/201424043)
- 1788 Gatuzz, E., Sanders, J. S., Dennerl, K.,  
 1789 et al. 2023, Measuring the ICM velocity  
 1790 structure in the Ophiuchus cluster,  
 1791 Tech. rep.,  
 1792 doi: [10.48550/arXiv.2303.17556](https://arxiv.org/abs/2303.17556)
- 1793 Gendron-Marsolais, M.,  
 1794 Hlavacek-Larrondo, J., Martin, T. B.,  
 1795 et al. 2018, Monthly Notices of the  
 1796 Royal Astronomical Society, 479, L28,  
 1797 doi: [10.1093/mnrasl/sly084](https://doi.org/10.1093/mnrasl/sly084)
- 1798 Govoni, F., Murgia, M., Feretti, L., et al.  
 1799 2006, Astronomy and Astrophysics,  
 1800 Volume 460, Issue 2, December III  
 1801 2006, pp.425-438, 460, 425,  
 1802 doi: [10.1051/0004-6361:20065964](https://doi.org/10.1051/0004-6361:20065964)
- 1803 Guidetti, D., Murgia, M., Govoni, F.,  
 1804 et al. 2008, Astronomy and  
 1805 Astrophysics, Volume 483, Issue 3,  
 1806 2008, pp.699-713, 483, 699,  
 1807 doi: [10.1051/0004-6361:20078576](https://doi.org/10.1051/0004-6361:20078576)
- 1808 Hitomi Collaboration, Aharonian, F.,  
 1809 Akamatsu, H., et al. 2016, Nature, 535,  
 1810 117, doi: [10.1038/nature18627](https://doi.org/10.1038/nature18627)
- 1811 —. 2018, Publications of the  
 1812 Astronomical Society of Japan, 70, 9,  
 1813 doi: [10.1093/pasj/psx138](https://doi.org/10.1093/pasj/psx138)
- 1814 Hu, H., Qiu, Y., Gendron-Marsolais,  
 1815 M.-L., et al. 2022, The Astrophysical  
 1816 Journal, 929, L30,  
 1817 doi: [10.3847/2041-8213/ac6601](https://doi.org/10.3847/2041-8213/ac6601)
- 1818 Jaffe, A. H., & Kamionkowski, M. 1998,  
 1819 Physical Review D, 58, 043001,  
 1820 doi: [10.1103/PhysRevD.58.043001](https://doi.org/10.1103/PhysRevD.58.043001)
- 1821 Khatri, R., & Gaspari, M. 2016, Monthly  
 1822 Notices of the Royal Astronomical  
 1823 Society, 463, 655,  
 1824 doi: [10.1093/mnras/stw2027](https://doi.org/10.1093/mnras/stw2027)
- 1825 Koch, E. W., Rosolowsky, E. W., Boyden,  
 1826 R. D., et al. 2019, The Astronomical  
 1827 Journal, 158, 1,  
 1828 doi: [10.3847/1538-3881/ab1cc0](https://doi.org/10.3847/1538-3881/ab1cc0)
- 1829 Koch, E. W., Ward, C. G., Offner, S.,  
 1830 Loeppky, J. L., & Rosolowsky, E. W.  
 1831 2017, Monthly Notices of the Royal  
 1832 Astronomical Society, 471, 1506,  
 1833 doi: [10.1093/mnras/stx1671](https://doi.org/10.1093/mnras/stx1671)
- 1834 Kolmogorov, A. N. 1941, Dokl. Akad.  
 1835 Nauk SSSR, 30, 301,  
 1836 doi: [10.1098/rspa.1991.0075](https://doi.org/10.1098/rspa.1991.0075)

- 1837 Kunz, M. W., Jones, T. W., &  
 1838 Zhuravleva, I. 2022, Plasma physics of  
 1839 the intracluster medium, Tech. rep.,  
 1840 doi: [10.48550/arXiv.2205.02489](https://doi.org/10.48550/arXiv.2205.02489)
- 1841 Laing, R. A., Bridle, A. H., Parma, P., &  
 1842 Murgia, M. 2008, Monthly Notices of  
 1843 the Royal Astronomical Society, 391,  
 1844 521,  
 1845 doi: [10.1111/j.1365-2966.2008.13895.x](https://doi.org/10.1111/j.1365-2966.2008.13895.x)
- 1846 Lazarian, A., & Pogosyan, D. 2000, The  
 1847 Astrophysical Journal, 537, 720,  
 1848 doi: [10.1086/309040](https://doi.org/10.1086/309040)
- 1849 —. 2004, The Astrophysical Journal, 616,  
 1850 943, doi: [10.1086/422462](https://doi.org/10.1086/422462)
- 1851 Li, Y., Gendron-Marsolais, M.-L.,  
 1852 Zhuravleva, I., et al. 2020, The  
 1853 Astrophysical Journal, 889, L1,  
 1854 doi: [10.3847/2041-8213/ab65c7](https://doi.org/10.3847/2041-8213/ab65c7)
- 1855 Mac Low, M.-M., & Ossenkopf, V. 2000,  
 1856 Astronomy and Astrophysics, 353, 339,  
 1857 doi: [10.48550/arXiv.astro-ph/9906334](https://doi.org/10.48550/arXiv.astro-ph/9906334)
- 1858 Martin, T., Drissen, L., & Joncas, G.  
 1859 2015, 495, 327. <https://ui.adsabs.harvard.edu/abs/2015ASPC..495..327M>
- 1860 Martin, T., Drissen, L., & Prunet, S.  
 1861 2021a, Monthly Notices of the Royal  
 1862 Astronomical Society, 505, 5514,  
 1863 doi: [10.1093/mnras/stab1656](https://doi.org/10.1093/mnras/stab1656)
- 1864 Martin, T., Milisavljevic, D., & Drissen,  
 1865 L. 2021b, Monthly Notices of the Royal  
 1866 Astronomical Society, 502, 1864,  
 1867 doi: [10.1093/mnras/staa4046](https://doi.org/10.1093/mnras/staa4046)
- 1868 Martin, T. B., Drissen, L., & Melchior,  
 1869 A.-L. 2018, Monthly Notices of the  
 1870 Royal Astronomical Society, 473, 4130,  
 1871 doi: [10.1093/mnras/stx2513](https://doi.org/10.1093/mnras/stx2513)
- 1872 Mignone, A., Bodo, G., Massaglia, S.,  
 1873 et al. 2007, The Astrophysical Journal  
 1874 Supplement Series, 170, 228,  
 1875 doi: [10.1086/513316](https://doi.org/10.1086/513316)
- 1876 Mignone, A., Zanni, C., Tzeferacos, P.,  
 1877 et al. 2012, The Astrophysical Journal  
 1878 Supplement Series, 198, 7,  
 1879 doi: [10.1088/0067-0049/198/1/7](https://doi.org/10.1088/0067-0049/198/1/7)
- 1880 Miville-Deschénes, M. A., Levrier, F., &  
 1881 Falgarone, E. 2003, The Astrophysical  
 1882 Journal, 593, 831, doi: [10.1086/376603](https://doi.org/10.1086/376603)
- 1884 Mohapatra, R., Federrath, C., & Sharma,  
 1885 P. 2020, Monthly Notices of the Royal  
 1886 Astronomical Society, 493, 5838,  
 1887 doi: [10.1093/mnras/staa711](https://doi.org/10.1093/mnras/staa711)
- 1888 —. 2021, Monthly Notices of the Royal  
 1889 Astronomical Society, 500, 5072,  
 1890 doi: [10.1093/mnras/staa3564](https://doi.org/10.1093/mnras/staa3564)
- 1891 —. 2022a, Monthly Notices of the Royal  
 1892 Astronomical Society, 514, 3139,  
 1893 doi: [10.1093/mnras/stac1610](https://doi.org/10.1093/mnras/stac1610)
- 1894 Mohapatra, R., Jetti, M., Sharma, P., &  
 1895 Federrath, C. 2022b, Monthly Notices  
 1896 of the Royal Astronomical Society, 510,  
 1897 2327, doi: [10.1093/mnras/stab3429](https://doi.org/10.1093/mnras/stab3429)
- 1898 —. 2022c, Monthly Notices of the Royal  
 1899 Astronomical Society, 510, 3778,  
 1900 doi: [10.1093/mnras/stab3603](https://doi.org/10.1093/mnras/stab3603)
- 1901 Mohapatra, R., & Sharma, P. 2019,  
 1902 Monthly Notices of the Royal  
 1903 Astronomical Society, 484, 4881,  
 1904 doi: [10.1093/mnras/stz328](https://doi.org/10.1093/mnras/stz328)
- 1905 Mohapatra, R., Sharma, P., Federrath,  
 1906 C., & Quataert, E. 2023, Multiphase  
 1907 condensation in cluster halos: interplay  
 1908 of cooling, buoyancy and mixing, Tech.  
 1909 rep., doi: [10.48550/arXiv.2302.09380](https://doi.org/10.48550/arXiv.2302.09380)
- 1910 Molina, F. Z., Glover, S. C. O., Federrath,  
 1911 C., & Klessen, R. S. 2012, Monthly  
 1912 Notices of the Royal Astronomical  
 1913 Society, 423, 2680,  
 1914 doi: [10.1111/j.1365-2966.2012.21075.x](https://doi.org/10.1111/j.1365-2966.2012.21075.x)
- 1915 Mroczkowski, T., Nagai, D., Basu, K.,  
 1916 et al. 2019, Space Science Reviews, 215,  
 1917 17, doi: [10.1007/s11214-019-0581-2](https://doi.org/10.1007/s11214-019-0581-2)
- 1918 Murgia, M., Govoni, F., Feretti, L., et al.  
 1919 2004, Astronomy and Astrophysics,  
 1920 v.424, p.429-446 (2004), 424, 429,  
 1921 doi: [10.1051/0004-6361:20040191](https://doi.org/10.1051/0004-6361:20040191)
- 1922 Nagai, D., Kravtsov, A. V., & Vikhlinin,  
 1923 A. 2007, The Astrophysical Journal,  
 1924 668, 1, doi: [10.1086/521328](https://doi.org/10.1086/521328)
- 1925 Nelson, K., Lau, E. T., Nagai, D., Rudd,  
 1926 D. H., & Yu, L. 2014, The  
 1927 Astrophysical Journal, 782, 107,  
 1928 doi: [10.1088/0004-637X/782/2/107](https://doi.org/10.1088/0004-637X/782/2/107)
- 1929 Oppenheim, A. V., Schafer, R. W., &  
 1930 Buck, J. R. 1999, Discrete-Time Signal  
 1931 Processing (Pearson Education India)

- 1932 Ossenkopf, V., Esquivel, A., Lazarian, A., & Stutzki, J. 2006a, *Astronomy and Astrophysics*, Volume 452, Issue 1, June II 2006, pp.223-236, 452, 223, doi: [10.1051/0004-6361:20052754](https://doi.org/10.1051/0004-6361:20052754)
- 1933 —. 2006b, *Astronomy and Astrophysics*, Volume 452, Issue 1, June II 2006, pp.223-236, 452, 223, doi: [10.1051/0004-6361:20052754](https://doi.org/10.1051/0004-6361:20052754)
- 1934 Ossenkopf, V., Krips, M., & Stutzki, J. 2008, *Astronomy and Astrophysics*, 485, 917, doi: [10.1051/0004-6361:20079106](https://doi.org/10.1051/0004-6361:20079106)
- 1935 Oughton, S., Matthaeus, W. H., Wan, M., & Osman, K. T. 2015, *Phil. Trans. R. Soc. A*, 373, doi: [10.1098/rsta.2014.0152](https://doi.org/10.1098/rsta.2014.0152)
- 1936 Peacock, J. A. 1999, *Cosmological Physics*. <https://ui.adsabs.harvard.edu/abs/1999coph.book.....P>
- 1937 Pope, S. B. 2000, *Turbulent Flows*. <https://ui.adsabs.harvard.edu/abs/2000tufl.book.....P>
- 1938 Pratt, G. W., Arnaud, M., Biviano, A., et al. 2019, *Space Science Reviews*, 215, 25, doi: [10.1007/s11214-019-0591-0](https://doi.org/10.1007/s11214-019-0591-0)
- 1939 Rincon, F. 2019, *Journal of Plasma Physics*, 85, 205850401, doi: [10.1017/S0022377819000539](https://doi.org/10.1017/S0022377819000539)
- 1940 Roman-Duval, J., Federrath, C., Brunt, C., et al. 2011, *The Astrophysical Journal*, 740, 120, doi: [10.1088/0004-637X/740/2/120](https://doi.org/10.1088/0004-637X/740/2/120)
- 1941 Sato, T., Hughes, J. P., Williams, B. J., & Morii, M. 2019, *The Astrophysical Journal*, 879, 64, doi: [10.3847/1538-4357/ab24db](https://doi.org/10.3847/1538-4357/ab24db)
- 1942 Schekochihin, A. A., & Cowley, S. C. 2006, *Physics of Plasmas*, 13, 056501, doi: [10.1063/1.2179053](https://doi.org/10.1063/1.2179053)
- 1943 Schuster, A. 1898, *Terrestrial Magnetism (Journal of Geophysical Research)*, 3, 13, doi: [10.1029/TM003i001p00013](https://doi.org/10.1029/TM003i001p00013)
- 1944 Shi, X., Nagai, D., & Lau, E. T. 2018, *Monthly Notices of the Royal Astronomical Society*, 481, 1075, doi: [10.1093/mnras/sty2340](https://doi.org/10.1093/mnras/sty2340)
- 1945 Shi, X., & Zhang, C. 2019, *Monthly Notices of the Royal Astronomical Society*, 487, 1072, doi: [10.1093/mnras/stz1392](https://doi.org/10.1093/mnras/stz1392)
- 1946 Simionescu, A., ZuHone, J., Zhuravleva, I., et al. 2019, *Space Science Reviews*, 215, 24, doi: [10.1007/s11214-019-0590-1](https://doi.org/10.1007/s11214-019-0590-1)
- 1947 Simonte, M., Vazza, F., Brightenti, F., et al. 2022, *Astronomy and Astrophysics*, 658, A149, doi: [10.1051/0004-6361/202141703](https://doi.org/10.1051/0004-6361/202141703)
- 1948 Spitzer, L. 1962, *Physics of Fully Ionized Gases*. <https://ui.adsabs.harvard.edu/abs/1962pfig.book.....S/abstract>
- 1949 Sreenivasan, K. R. 1995, *Phys. Fluids*, 7, 2778
- 1950 Stoica, P., & Moses, R. 2005, *Spectral Analysis of Signals* (Pearson Prentice Hall Upper Saddle River, NJ)
- 1951 Stutzki, J., Bensch, F., Heithausen, A., Ossenkopf, V., & Zielinsky, M. 1998, *Astronomy and Astrophysics*, 336, 697. <https://ui.adsabs.harvard.edu/abs/1998A&A...336..697S/abstract>
- 1952 Subedi, P., Chhiber, R., Tassein, J. A., Wan, M., & Matthaeus, W. H. 2014, *The Astrophysical Journal*, 796, 97, doi: [10.1088/0004-637X/796/2/97](https://doi.org/10.1088/0004-637X/796/2/97)
- 1953 Sutherland, R. S., & Dopita, M. A. 1993, *The Astrophysical Journal Supplement Series*, 88, 253, doi: [10.1086/191823](https://doi.org/10.1086/191823)
- 1954 Tennekes, H., & Lumley, J. L. 1972, *First Course in Turbulence*. <https://ui.adsabs.harvard.edu/abs/1972fct..book.....T>
- 1955 Vacca, V., Murgia, M., Govoni, F., et al. 2010, *Astronomy and Astrophysics*, Volume 514, id.A71, <NUMPAGES>12</NUMPAGES> pp., 514, A71, doi: [10.1051/0004-6361/200913060](https://doi.org/10.1051/0004-6361/200913060)
- 1956 —. 2012, *Astronomy & Astrophysics*, Volume 540, id.A38, <NUMPAGES>15</NUMPAGES> pp., 540, A38, doi: [10.1051/0004-6361/201116622](https://doi.org/10.1051/0004-6361/201116622)
- 1957 Valdarnini, R. 2019, *The Astrophysical Journal*, 874, 42, doi: [10.3847/1538-4357/ab0964](https://doi.org/10.3847/1538-4357/ab0964)
- 1958 van der Walt, S., Schönberger, J. L., Nunez-Iglesias, J., et al. 2014, *PeerJ*, 2, e453, doi: [10.7717/peerj.453](https://doi.org/10.7717/peerj.453)

- 2029 van Weeren, R. J., de Gasperin, F.,  
 2030 Akamatsu, H., et al. 2019, Space Sci  
 2031 Rev, 215, 16,  
 2032 doi: [10.1007/s11214-019-0584-z](https://doi.org/10.1007/s11214-019-0584-z)
- 2033 Vazza, F., Brunetti, G., Gheller, C.,  
 2034 Brunino, R., & Brüggen, M. 2011,  
 2035 Astronomy and Astrophysics, 529, A17,  
 2036 doi: [10.1051/0004-6361/201016015](https://doi.org/10.1051/0004-6361/201016015)
- 2037 Virtanen, P., Gommers, R., Oliphant,  
 2038 T. E., et al. 2020, Nature Methods, 17,  
 2039 261, doi: [10.1038/s41592-019-0686-2](https://doi.org/10.1038/s41592-019-0686-2)
- 2040 Vogt, C., & Enßlin, T. A. 2003,  
 2041 Astronomy and Astrophysics, v.412,  
 2042 p.373-385 (2003), 412, 373,  
 2043 doi: [10.1051/0004-6361:20031434](https://doi.org/10.1051/0004-6361:20031434)
- 2044 —. 2005, Astronomy and Astrophysics,  
 2045 Volume 434, Issue 1, April IV 2005,  
 2046 pp.67-76, 434, 67,  
 2047 doi: [10.1051/0004-6361:20041839](https://doi.org/10.1051/0004-6361:20041839)
- 2048 Walker, S. A., Sanders, J. S., & Fabian,  
 2049 A. C. 2015, Monthly Notices of the  
 2050 Royal Astronomical Society, 453, 3699,  
 2051 doi: [10.1093/mnras/stv1929](https://doi.org/10.1093/mnras/stv1929)
- 2052 Wan, M., Oughton, S., Servidio, S., &  
 2053 Matthaeus, W. H. 2010, Physics of  
 2054 Plasmas, 17, 082308,  
 2055 doi: [10.1063/1.3474957](https://doi.org/10.1063/1.3474957)
- 2056 Wang, C., Ruszkowski, M., Pfrommer, C.,  
 2057 Oh, S. P., & Yang, H. Y. K. 2021,  
 2058 Monthly Notices of the Royal  
 2059 Astronomical Society, 504, 898,  
 2060 doi: [10.1093/mnras/stab966](https://doi.org/10.1093/mnras/stab966)
- 2061 XRISM Science Team. 2020, Science with  
 2062 the X-ray Imaging and Spectroscopy  
 2063 Mission (XRISM), Tech. rep.,  
 2064 doi: [10.48550/arXiv.2003.04962](https://arxiv.org/abs/2003.04962)
- 2065 Zhang, C., Churazov, E., & Schekochihin,  
 2066 A. A. 2018, Monthly Notices of the  
 2067 Royal Astronomical Society, 478, 4785,  
 2068 doi: [10.1093/mnras/sty1269](https://doi.org/10.1093/mnras/sty1269)
- 2069 Zhang, C., Zhuravleva, I.,  
 2070 Gendron-Marsolais, M.-L., et al. 2022,  
 2071 Monthly Notices of the Royal  
 2072 Astronomical Society, 517, 616,  
 2073 doi: [10.1093/mnras/stac2282](https://doi.org/10.1093/mnras/stac2282)
- 2074 Zhou, Y., Mitsuda, K., & Yamasaki, N. Y.  
 2075 2022, The Astrophysical Journal, 929,  
 2076 128, doi: [10.3847/1538-4357/ac5966](https://doi.org/10.3847/1538-4357/ac5966)
- 2077 Zhuravleva, I., Allen, S. W., Mantz, A., &  
 2078 Werner, N. 2018, The Astrophysical  
 2079 Journal, 865, 53,  
 2080 doi: [10.3847/1538-4357/aadae3](https://doi.org/10.3847/1538-4357/aadae3)
- 2081 Zhuravleva, I., Chen, M. C., Churazov,  
 2082 E., et al. 2022, Indirect Measurements  
 2083 of Gas Velocities in Galaxy Clusters:  
 2084 Effects of Ellipticity and Cluster  
 2085 Dynamic State, Tech. rep.  
 2086 <https://ui.adsabs.harvard.edu/abs/2022arXiv221011544Z>
- 2088 Zhuravleva, I., Churazov, E., Kravtsov,  
 2089 A., & Sunyaev, R. 2012, Monthly  
 2090 Notices of the Royal Astronomical  
 2091 Society, 422, 2712,  
 2092 doi: [10.1111/j.1365-2966.2012.20844.x](https://doi.org/10.1111/j.1365-2966.2012.20844.x)
- 2093 Zhuravleva, I., Churazov, E.,  
 2094 Schekochihin, A. A., et al. 2019, Nature  
 2095 Astronomy, 3, 832,  
 2096 doi: [10.1038/s41550-019-0794-z](https://doi.org/10.1038/s41550-019-0794-z)
- 2097 —. 2014a, Nature, 515, 85,  
 2098 doi: [10.1038/nature13830](https://doi.org/10.1038/nature13830)
- 2099 Zhuravleva, I., Churazov, E. M.,  
 2100 Schekochihin, A. A., et al. 2014b, The  
 2101 Astrophysical Journal, 788, L13,  
 2102 doi: [10.1088/2041-8205/788/1/L13](https://doi.org/10.1088/2041-8205/788/1/L13)
- 2103 ZuHone, J. A., Markevitch, M., &  
 2104 Zhuravleva, I. 2016, The Astrophysical  
 2105 Journal, 817, 110,  
 2106 doi: [10.3847/0004-637X/817/2/110](https://doi.org/10.3847/0004-637X/817/2/110)